ICHF
Institute of Physical Chemistry PAS

PhD Dissertation

Effects of Confinement on Self-assembly in Systems with Competing Interactions

Horacio Antonio Serna Serna

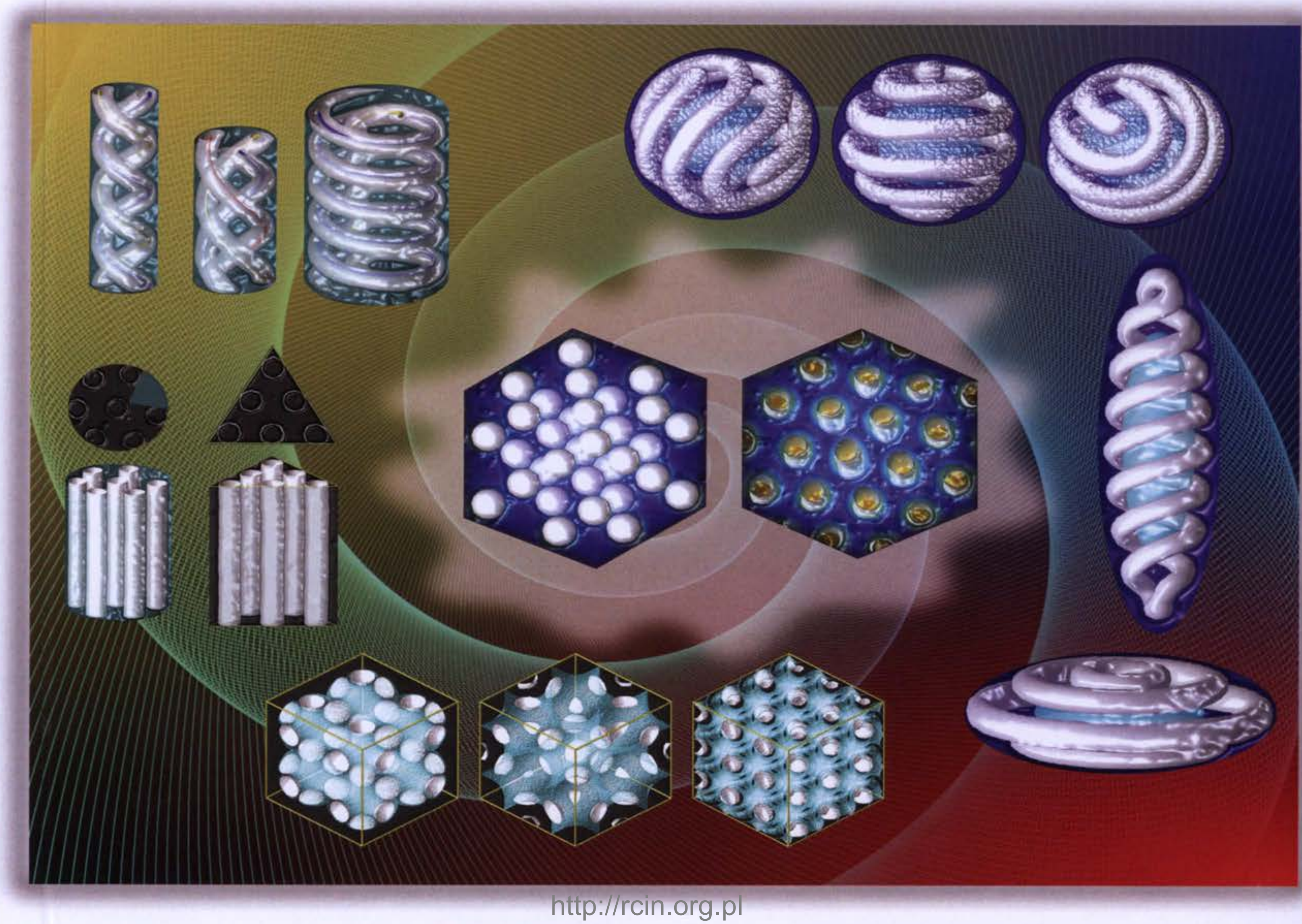

Institute of Physical Chemistry
Polish Academy of Sciences
Kasprzaka 44/52, 01-224
Warsaw, Poland

Effects of confinement on self-assembly in systems with competing interactions

Horacio Antonio Serna Serna

Department of Complex Systems and Chemical Processing of Information
Group of Physical Chemistry of Complex Systems

Supervisors:

Prof. dr hab. Wojciech Góźdź
Dr. Eva González Noya

This dissertation was prepared within the International PhD Studies at the Institute of Physical Chemistry of the Polish Academy of Sciences in Warsaw, in collaboration with Dr. Eva González Noya from the Institute of Physical Chemistry "Rocasolano" (IQFR) in Madrid.

Warsaw
May, 2021

Funding

This research is part of a project that has received funding from the European Union's Horizon 2020 research and innovation programme under the Marie Skłodowska-Curie grant agreement No. 711859.

Scientific work funded from the financial resources for science in the years 2017-2022 awarded by the Polish Ministry of Science and Higher Education for the implementation of an international co-financed project.

Horizon 2020
European Union Funding
for Research & Innovation

NaMeS

Ministry of Science
and Higher Education
Republic of Poland

MARIE CURIE ACTIONS

Para mis amados padres, a quienes debo todo.

La ciencia ha eliminado las distancias, pregonaba Melquíades. Dentro de poco, el hombre podrá ver lo que ocurre en cualquier lugar de la tierra, sin moverse de su casa.

Cien Años de Soledad, Gabriel García Márquez.

Almost in the beginning was curiosity.

Asimov's New Guide To Science, Isaac Asimov.

Acknowledgements

First of all, I wish to express my deepest gratitude to my supervisors, Professor Wojciech Góźdź and Dr Eva González Noya. Thank you for your guidance, patience and support in these four years.

At the Institute of Physical Chemistry (IPC PAS), I had the pleasure of meeting great scientists who have assisted me during this time. In particular, I want to thank Dr Jakub Pękalski, who helped me a lot at the beginning of my studies when I was a newcomer. Also, I would like to thank Dr Ariel Meyra for the constructive discussions we had during his stay at the IPC PAS. Some of these discussions transcended to collaborations. I also want to thank all the members of the Department of Complex Systems and Chemical Processing of Information that have been involved in my research in one way or another. I especially want to thank Carolina Cruz. Some of the discussions I had with her helped me clarify my ideas.

During my six months stay in the Institute of Physical Chemistry "Rocasolano" in Madrid, I belonged to the group of Professor Enrique Lomba; I express my gratitude to him and all the members of his group. In particular, I would like to thank Antonio Díaz Pozuelo; his programming skills were crucial to carry out my research in Madrid.

At this stage, I cannot forget the people who inspired me to become a scientist. I am indebted to Professors Carlos Eduardo Sierra Cuartas and Daniel Barragán Ramirez, my former supervisors. They showed me how fun and meaningful science could be.

Me permito terminar con unas palabras en mi nativo español. Mis más sinceros y profundos agradecimientos a mis padres, y en general a toda mi familia. Si no fuera por ellos nada de esto hubiera sido posible. También extiendo un sentido agradeciemiento a mis amigos en Medellín, especialmente a Mateo y a Andrés, quienes con las palabras indicadas supieron subirme el ánimo en los momentos más complicados de esta aventura. Finalmente, quiero agradecer a mi chica, Agnieszka, por su paciencia y comprensión, sobre todo en la recta final de mis estudios de doctorado.

Supervisors

Prof. dr hab. Wojciech Goźdź, Supervisor

(Department of Complex Systems and Chemical Processing of Information.

Institute of Physical Chemistry of the Polish Academy of Sciences, Warsaw, Poland.)

Dr. Eva González Noya, Supervisor

(Group of Statistical Mechanics & Condensed Matter.

Institute of Physical Chemistry "Rocasolano", CSIC, Madrid, Spain.)

ABSTRACT

Systems with competing interactions, such as colloidal suspensions, block copolymers and lipids mixtures, have shown interesting self-assembling properties that can be exploited in technological applications. It has been demonstrated that despite the type and nature of the interactions, systems with competing interactions exhibit a universal phase behaviour in bulk. Ordered microphases such as cluster-crystals, hexagonal, cubic bicontinuous and lamellar phases are often observed in this kind of systems.

When confined, systems with competing interactions behave differently, showing new structural, thermodynamic, and dynamic properties. In the thesis, we investigate colloidal fluids with competing interactions under confinement into channels and pores with different morphology. The colloidal fluid consists of spherical particles interacting via an isotropic short-range attraction and long-range repulsion (SALR) potential. We consider repulsive interactions between the colloidal particles and the walls of the confining channels and pores.

We start the study by confining the colloidal fluid into channels with different cross-section geometries. Using Grand Canonical Monte Carlo (GCMC) simulations, we found that the structure of the ordered microphases can be tuned by confinement. We observed the formation of helical structures inside cylindrical and elliptical pores. We also found that triangular, hexagonal and wedged-cylindrical channels promoted the nucleation of ordered microphases with the same structure

of the bulk hexagonal phase.

We continue the research by investigating the behaviour of the colloidal system under confinement into curved quasi-bidimensional space. Using GCMC simulations again, we study the colloidal fluid confined into spherical and ellipsoidal narrow shells. We observed that in conditions at which the hexagonal phase is stable in bulk, the system self-assembled into coiled cylindrical clusters that resembled geometrical solutions of the problem of the longest rope filling the surface of a sphere. On the other hand, the confinement into prolate and oblate ellipsoidal shells favoured the formation of helical and toroidal structures, respectively.

Additionally, we investigated the colloidal system when confined into ordered bicontinuous porous materials. A GCMC simulation study revealed that, depending on the morphology and the size of the porous materials, the colloidal system could form a set of new cluster crystals formed from cylindrical and spherical clusters that are not stable in bulk. Interestingly, we observed that some pore sizes and morphologies promoted the formation of ordered microphases with the same structure of the cluster-crystal and hexagonal phases in bulk.

In the last part of the research, we performed Molecular Dynamics (MD) simulations, in bulk and under confinement into slit pores, of a colloidal system with competing interactions modelled with a SALR potential. In bulk, besides the formation of the typically ordered microphases, we observed intra-cluster freezing transitions. Such transitions were characterised from structural, thermodynamic and dynamic points of view. We found that the confinement into slit pores induced a change in the phase diagram of the colloidal system. Moreover, we observed that the diffusion of the colloidal particles could be enhanced for some pore widths.

In the thesis, we presented evidence that the universal phase behaviour of systems with competing interactions extends to confined systems. Moreover, we showed that confinement not only favours the formation of new ordered structures that can be exploited in nanotechnology but also helps in the nucleation of ordered cluster crystals. Thus, the confinement can be used to obtain the ordered microphases in colloidal systems, which have been elusive in experiments so far.

The majority of the results are collected in the following papers:

Published

1. **Serna, Horacio**, Eva G. Noya, and W. T. Góźdź. *Assembly of helical structures in systems with competing interactions under cylindrical confinement.* Langmuir 35.3 (2019): 702-708. (Section 2.2).
2. **Serna, Horacio**, Eva G. Noya, and Wojciech T. Góźdź. *The influence of confinement on the structure of colloidal systems with competing interactions.* Soft Matter 16.3 (2020): 718-727. (Section 2.3).
3. **Serna, Horacio**, Eva G. Noya, and Wojciech T. Góźdź. *Confinement of Colloids with Competing Interactions in Ordered Porous Materials.* The Journal of Physical Chemistry B 124.46 (2020): 10567-10577.(Chapter 4)
4. **Serna, Horacio**, Antonio Díaz Pozuelo, Eva G. Noya, and Wojciech T. Góźdź. *Formation and internal ordering of periodic microphases in colloidal models with competing interactions.* Soft Matter 17.19 (2021): 4957-4968 . (Section 5.2).

In preparation

1. **Serna, Horacio**, Ariel G. Meyra, Eva G. Noya, and Wojciech T. Góźdź. *Confinement of colloids with competing interactions in spherical shells.* (Chapter 3).
2. **Serna, Horacio**, Eva G. Noya, and Wojciech T. Góźdź. *Self-assembly of colloids with competing interactions confined in slit pores.*(Section 5.3).

Contents

List of Tables

List of Figures

Chapter 1

Introduction

Soft matter materials often exhibit self-assembling properties. Self-assembly is the spontaneous emergence of ordered structures from a disordered system composed of fundamental units without external assistance [1]. This process is driven by the information present in the way in which the fundamental units interact with each other. The fundamental units can be molecules or particles, and their interactions can be isotropic (direction independent) or anisotropic (direction-dependent). For instance, block copolymers, surfactants and patchy colloids show anisotropic interactions, whereas colloids with competing interactions can be modelled by effective isotropic potentials. In modern science and engineering, understanding self-assembly is crucial since it is one of the practical routes for producing nanostructures, which is essential to design functional nanomaterials [1, 2, 3]. The self-assembly we consider in the thesis is static, i.e. the ordered self-assembled structures correspond to free energy minima. We will focus on the study of colloidal systems with competing interactions, a particular type of colloidal suspensions that exhibit self-assembling properties at two different length-scales (see Section1.1). Colloidal systems with competing interactions share some features with protein solutions and block copolymers. In particular, their effective interactions are similar to those in protein solutions [4, 5], and the self-assembled structures to those observed in block copolymers [6, 7].

In this chapter, we first discuss the phenomenology and phase behaviour of colloidal systems with competing interactions both in bulk and under confinement. Then, we will briefly comment on investigations on block copolymers, emphasising the similarities with colloidal systems with competing interactions. After that, we will detail the modelling and simulation methods we are employing in the dissertation. Finally, we define the scope of the thesis.

1.1 Colloidal systems with competing interactions

1.1.1 Phenomenology and bulk behaviour

A colloidal system is a mixture in which one substance (dispersed phase) is microscopically dispersed into another (dispersion medium). Typically, both phases are not miscible, which leads to phase separation. The particle size of the dispersed phase usually is between $1nm$ and $500nm$ [8]. To understand the behaviour of colloidal systems, not only the interactions between particles are essential, but also the interactions with the solvent (dispersion medium) [9]. Furthermore, the strength and type of interactions can be modified by changing external parameters, such as temperature, pressure and pH, or adding co-solutes. For instance, stabilising agents, like salts, and depleting agents, like non-adsorbing polymers, are widely used to tune the interactions in colloidal systems [10].

Let us consider colloidal particles, with diameter σ, dispersed throughout a liquid phase. In the simplest case, particles can be considered hard spheres, and thus they only interact by volume exclusion. However, more factors must be taken into account to complete a more accurate description of the system. The surface of the colloidal particles tends to accumulate a certain amount of charge due to the release of counterions to the solvent. Although the surface charge depends on the fraction of dissociated counterions, in simple models we can assume that the charge on the surface of the particles is constant [10]. The presence of charges induces an electrostatic repulsive interaction between particles. In most cases, the repulsion is somewhat screened by the free counterions in the solvent (See Figure 1.1).

On the other hand, we can add another solute, with a size much smaller than σ, which acts as a depletant. The presence of depletants promotes attractive interactions at short-ranges due to depletion forces. There is a region of excluded volume surrounding the colloidal particles, which is not available for the centres of the depletants to occupy (See Figure 1.1). When colloidal particles are close enough, their excluded volumes overlap and, in consequence, depletants are driven out the inter-particle region, creating a depletant concentration gradient between the surroundings and the inter-particle regions, with an associated osmotic pressure that acts on the colloidal particles inwards [11]. Thus, the solvent amount is reduced in the inter-particle region, which results in an effective attraction between colloidal particles at short ranges [12, 13]. Depletion forces are

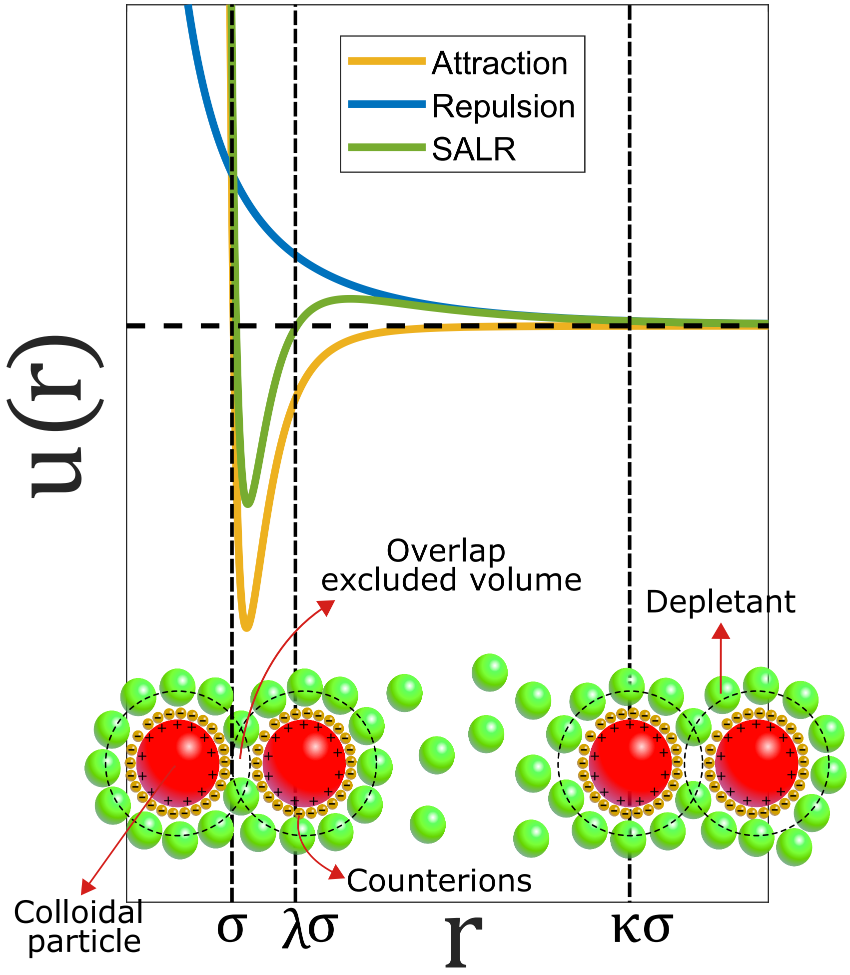

Figure 1.1: The SALR potential is a summation of short-range attraction and long-range repulsion terms. The attraction comes from depletion forces, and the repulsion comes from screened electrostatic interactions. Here σ is the diameter of the colloidal particles, used as length unit, λ is the attractive range and κ the repulsive range. SALR potentials are an effective and simplified model of a complex interplay between colloidal particles, solvent, counterions and depletants.

considered entropic forces, as was demonstrated in the seminal works by Asakura and Oosawa. In their model, they considered rigid particles and depletants that only interact via exclusion of volume. Therefore, the origin of the attractive force at short ranges has to be necessarily entropic [11, 14].

Now, we have two contributions: a long-range repulsion coming from screened electrostatic interactions and a short-range attraction coming from depletion forces. When both contributions are present, it is said that colloidal particles have competing interactions [10]. This complex interplay between colloidal particles, solvent, counterions, and depletants, which gives rise to a very rich phenomenology, can be simplified by combining an attractive term at short ranges, that describes the depletion forces, and a repulsive term at long ranges that describes the screened electrostatic interactions. An effective pair potential with short-range attraction and long-range repulsion is called SALR potential. Figure 1.1 shows how the repulsive and attractive contributions sum up to produce the effective SALR potential. Interestingly, many studies have shown that this type of effective potentials describes well not only colloidal systems but also solutions of globular proteins at moderate concentrations [4, 5].

The balance between attraction and repulsion at two length scales leads to self-assembly: the short-range attraction favours the aggregation, or clustering, of colloidal particles, and then the long-range repulsion prevents the clusters from merging, which eventually can lead to an ordered distribution of clusters. When attraction and repulsion are properly tuned, depending on the thermodynamic conditions, colloidal systems with competing interactions can self-assemble into cluster-crystal, hexagonal , bicontinuous and lamellar phases in bulk [15, 16, 17, 18, 19]. Iso-density surfaces of these periodic microphases are depicted in Figure 1.2. Regardless of the physical origin of competing interactions (amphiphilic, depletion + electrostatic, or any other), we always observe the same sequence of ordered microphases. This universality in the topology of the phase diagram of systems with competing interactions has been extensively documented, but one of the most important examples is the similarity between colloidal systems with competing interactions and block copolymers [17, 16]. We will discuss further on block copolymers in section 1.2.

SALR models with different functional shapes have been used to study systems with competing interactions. Combinations of potentials such as hard spheres plus double Kac -composed of two exponential functions- [20], hard spheres plus double Yukawa (HSDY) [21, 19], Lennard-Jones plus Yukawa (LJY) [22, 23], and hard spheres plus square attractive well plus repulsive linear ramp - the so-called square-well-linear (SWL) potential[24, 25, 18, 26] - are some examples of typically used SALR potentials. As long as the attractive and repulsive contributions are well-tuned, the functional shape of the SALR potential does not affect the qualitative phase behaviour of SALR systems. For instance, HSDY, LJY, and SWL potentials stabilise a cluster-crystal with cubic symmetry, a hexagonal phase, a bicontinuous phase, and a lamellar phase. (See Figure 5.2 and compare it with Figure 2 in reference [19] and Figure 2 in reference [24]). Numerous investigations have been devoted to SALR fluids in bulk. In the next lines, we will review some important contributions to the field.

Theoretical and simulation studies

Let us start with theoretical studies. Tarzia and Coniglio reported a study in which the short-range attraction was described by the Ginzburg-Landau theory, and the long-range screened repulsion by a Yukawa potential [27]. This model has been used to describe different systems, such as dipolar fluids, mixtures of block copolymers, water-oil-surfactant mixtures and superconductors. As this model can adequately describe different systems with competing interactions, predicting the formation of patterns with spatial inhomogeneities, it offers a unified vision of the phenomenology and phase behaviour of this type of systems. Particularly, the authors calculated a phase diagram in which lamellar and glassy phases were predicted at low enough temperatures. In the same direction, Ortix, Lorenzana and Di Castro proposed a theory in which the Ginzburg-Landau theory was extended with Coulombic interactions. The model predicted the stability of periodic microphases composed of inhomogeneities with the shape of droplets arranged in a BCC lattice, rods arranged in a triangular lattice and lamellae [28].

In 2008, Ciach proposed a Density-Functional Theory (DFT) [15]. The theory was developed in the context of self-assembling systems with competing interactions and predicted a universal phase diagram with a sequence of disordered fluid, BCC-cluster, hexagonal, lamellar, inverted hexagonal, inverted BCC-cluster and disordered fluid. The theory was applied in the HSDY potential for a specific case of very short-range attraction, predicting a gyroid phase located between the hexagonal and lamellar phases. Two years later, Ciach and Góźdź applied this theory to the HSDY potential to determine the stability region of the gyroid phase at different sets of parameters of the interaction potential [16]. The authors concluded that the free-energy landscape of SALR systems might contain many local minima corresponding to distorted bicontinuous networks. This suggests that, in experiments with colloids, the system might be trapped into a metastable glass-like disordered phase at conditions for which a bicontinuous phase should be thermodynamically stable.

Another theoretical contribution to SALR fluids was published by Roth in 2011 [29]. The author proposed a DFT for a two-dimensional system interacting via the HSDY potential. This system had been previously studied, by means of Monte Carlo (MC) simulations, in a seminal contribution to the field by Imperio and Reatto [30]. Theory and simulation agreed to predict cluster phases with the shape of droplets and stripes in bulk.

In recent years, Pini and Parola studied the HSDY potential in bulk by means of DFT in the grand canonical ensemble [19]. Fully numerical minimisation of the grand potential was carried

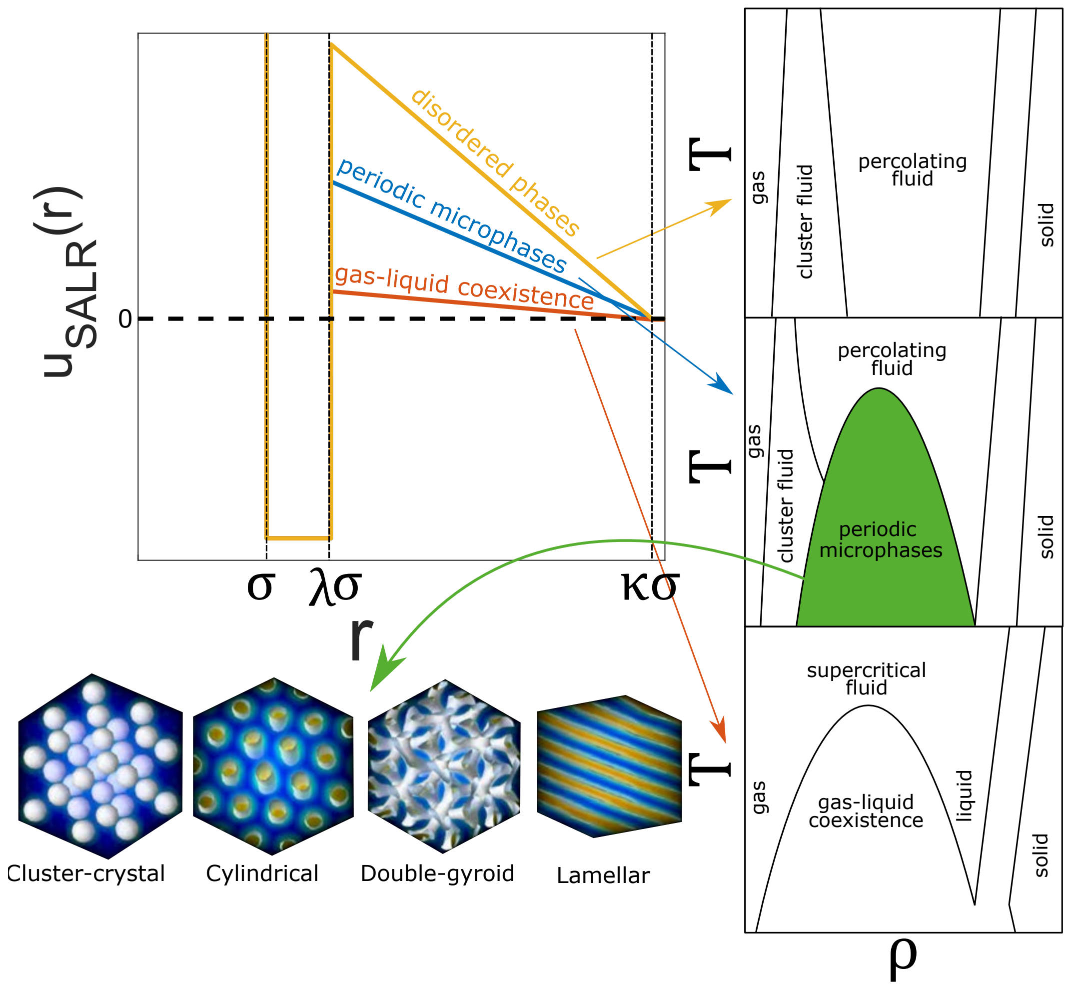

Figure 1.2: Effect of repulsion on the phase behaviour of colloidal systems with competing interactions. The SWL potential is depicted for various repulsion strengths at constant attraction. Here σ is the diameter of the colloidal particles, used as length unit, λ is the attractive range and κ the repulsive range. When attraction and repulsion are balanced, ordered microphases are stable at low to intermediate temperatures. Based on reference [18].

out to calculate the phase diagram at the microphase region. The same sequence of microphases was obtained: cluster-crystal, hexagonal, gyroid and lamellar. Interestingly, the authors found two stable symmetries for the cluster-crystal phase: at high temperatures, close to the maximium of the line that separates the ordered microphases from the disordered phases, a BCC-cluster is predicted, whereas, at lower temperatures, an HCP-cluster is the stable phase. In a contribution by Ciach, a new functional was developed where the local density was replaced by the volume fraction [31]. A simplified version of the theory was used to calculate the phase diagram of the SWL potential, showing good qualitative agreement with the phase diagram calculated from MC simulations [24], especially at high temperatures.

Accompanying the theoretical studies we just discussed, many simulation works contribute to the understanding of systems with competing interactions. Let us now focus on some relevant simulation works. In 1999, Sear *et. al.* performed MC simulations in the canonical ensemble for a SALR two-dimensional model composed of nanoparticles interacting via a hard disks plus double Kac potential [32]. The simulations predicted the formation of clusters of particles with a hexagonal distribution at low densities and elongated stripe-like clusters at high densities. Interestingly, the patterns obtained in simulations were in qualitative agreement with Langmuir films of Ag nanoparticles.

In 2004, Imperio and Reatto investigated the hard disks plus double Kac potential using MC simulations. Thermodynamic and structural analysis revealed the stability of two ordered phases: a hexagonal arrangement of circular clusters and a pattern of parallel stripe-like clusters [30]. Furthermore, the authors sketched the region in the phase diagram, where the microphases were expected (See Figure 14 of reference [30]). This region was further detailed, providing approximate regions of stability for each microphase (See Figure 13 in reference[33]).

The formation of disordered cluster phases in colloidal systems was studied in detail in references [22, 23] using MD simulations for particles interacting via the LJY potential. The authors observed dynamically arrested states at densities at which a cluster-crystal and hexagonal phase should be expected at low temperatures. Depending on the length of repulsion, the arrest mechanisms might be the formation of a cluster glass phase [22] or a one-dimensional growth of clusters followed by an arrested state due to the formation of a three-dimensional network [23]. The latter mechanism is similar to that observed in protein solutions [34, 35]. These investigations helped to understand the influence of the attractive and repulsive strengths and the role of the length scales on the phase behaviour of systems with competing interactions.

In a contribution by de Candia *et al.*, a three-dimensional colloidal model based on the Derjaguin-Landau-Verwey-Overbrek (DLVO) potential, which combines short-range attractive and long-range repulsive interactions, was studied through MD simulations in the canonical ensemble [36]. The results revealed that at low temperatures, the fluid self-assembles into a cylindrical phase with hexagonal distribution and into a lamellar phase for intermediate and high densities, respectively. Interestingly, the cylindrical aggregates exhibit the structure of Bernal spirals [37]. Furthermore, the lamellae are composed of two layers of hexagonally-packed particles.

In 2007, Archer and Wilding conducted a joint simulation and theoretical study of a three-dimensional model of particles interacting via the HSDY potential [38]. MC simulations in the grand canonical ensemble were performed. Particularly, the role of the strength of the attractive short-range interactions was evaluated, whereas the strength of the repulsive interaction was fixed. At low densities, the SALR fluid undergoes the transition from a vapour to a fluid of spherical clusters (droplets) upon decreasing the temperature. Similarly, at higher densities, a transition from the liquid to a fluid of spherical voids(bubbles) was observed.

In 2016, Zhuang *et al.* [24] developed a simulation method to calculate the phase diagram, at the microphase forming regime, of the SWL potential (See Figure 1.2). The authors reported the stability of FCC-cluster, hexagonal, double gyroid and lamellar phases. A priori, it seems that this potential might be artificial and unrealistic. However, the self-assembling features of more realistic SALR potentials like LJY (See Chapter 5)and HSDY [15, 19] are preserved in SWL potential. Besides, its piece-wise nature allowed the authors to modify one part without affecting the other, which is not possible in continuous models such as LJY. With these characteristics, more controlled and systematic *in silico* experiments can be performed [25, 18, 24]. For example, varying the repulsion at constant attraction or vice versa [25, 18].

The combined effect of attraction and repulsion is responsible for both the cluster size and their ordered distribution [20, 39, 30, 33]. The magnitude of repulsion can induce different phase behaviours. In Figure 1.2, we represent the SWL potential with different repulsion strengths at constant attraction. When the repulsion is small, the colloidal fluid behaves like a simple fluid that undergoes a gas-liquid transition, exhibiting the typical coexistence region. When the repulsion is increased in the right proportion, the gas-liquid coexistence disappears, and a region of periodic microphases emerges. If we keep increasing the repulsion, the ordered microphases region disappears and is replaced by a region in which a percolating fluid is stable.

Experimental studies

Let us now review some experimental works on colloidal systems with competing interactions in bulk. In 2004, Sedgwick *et al.* investigated the phase behaviour of a colloidal suspension composed of spherical particles of poly(methylmethacrylate) (PMMA). The solvent was chosen such that the colloidal particles obtain a net positive charge on the surface (a mixture of cycloheptyl bromide (CHB) and *cis*-decalin) [40]. Linear polystyrene was used as a depletant to induce short-range attraction. The authors observed a cluster phase at low densities and a gelation transition at higher densities. In an investigation by Stradner *et. al.*, two different systems were compared experimentally: lysozyme solutions and colloidal suspensions of PMMA particles [41]. Both systems exhibit similar phase behaviour, showing an equilibrium cluster phase followed by a gelation transition upon increasing density. These results revealed that the cluster phase was independent of the particular protein interactions but was rather related to the combination of weakly screened charges and short-range attractions present in both lysozyme solutions and colloidal suspensions of PMMA particles. This was an experimental confirmation of the similarity in phase behaviour of systems with competing interactions.

In 2005, Campbell *et al.* explored the effect of weak long-repulsion on the dynamical arrest of colloidal systems with short-range attractive forces experimentally [42]. The system was a suspension of chemically stabilised PMMA particles dispersed in a mixture of CHB and *cis*-decalin, which provides the particles with a positive charge. Similarly, as in reference [40], the attractive interaction was induced by adding polystyrene as a depleting agent. The authors observed the formation of stable chain-like clusters whose structure was built by the interpenetration of tetrahedral units. Those chain-like clusters evolved into a fully connected network to gelation when the density increased. In another work by Sánchez and Bartlett, the same colloidal system of PMMA particles was further studied [43]. The authors focused on the size and shape of the clusters close to the gelation transition. It was found that the average cluster size changes suddenly as the density approaches the gelation density. These observations supported the idea of an equilibrium phase transition from the cluster phase to the gel.

In an investigation by Klix, Royall and Tanaka, different dynamic and structural states were identified in a colloidal system of PMMA particles [44]. By varying the density and the concentration of depletant, a fluid, a cluster-fluid, a Wigner glass, a gel and a regular close-packed crystal (*i.e.* individual particles occupy the lattice sites) were observed and characterised. Continuing with the experimental investigations on the same model system, Zhang *et. al.* found that the size of the equilibrium clusters formed at low densities, contrary to theoretical predictions [45], decreased upon increasing the attraction strength [46]. The authors also observed gelation at high densities. The gels are microcrystalline for low strength of attraction, whereas strong attraction promotes percolation of almost linear clusters that leads to low density gels.

In an experimental and simulation study, a colloidal suspension of PMMA particles was analysed to determine the effects of polydispersity on the structure of the gel formed at high densities [47]. The authors also intended to find the lamellar phase that should be stable according to theoretical and simulation studies. A low-frequency alternating electric field was applied on a microcrystalline gel with 3 % of polydispersity, promoting the formation of a columnar state. However, after switching off the external electric field, the columnar structure relaxes to the initial microcrystalline gel. Simulation results revealed that in SALR colloids with a polydispersity of 1%, ordered structures, such as columnar or lamellar phases, are unstable and tend to form a segregated micro crystalline gel with a low local polydispersity. Although simulations results indicate that after long runs the microcrystalline gel should evolve to a lamellar phase, the experimental results never showed such periodic phase since the system exhibits dynamical arrest at these densities [47]. In 2016, both experiments and simulations were carried out to study the structural and dynamical behaviour of PMMA-based colloidal suspensions [48]. The results showed that gel formation could be preceded by continuous and directed percolation. Although both types of percolation lead to spanning networks, only directed percolation results in very slow dynamics. The authors conclude that a structural transition, as it is directed percolation, is linked to the dynamical arrest in gelation processes of colloidal systems with competing interactions.

In a recent investigation, colloidal strings, Bernal spiral-like, and hollow tubular clusters were observed experimentally [49]. Negatively charged colloids were functionalised by the addition of hydrophobic chains on the surface. Then, the functionalised nanoparticles were dispersed in an aqueous solution. Depending on the type of hydrophobic chains on the surface, the nanoparticles self-assemble into clusters with the shapes mentioned above.

As we just reviewed, ordered microphases have not been observed yet in experiments with colloidal systems with competing interactions. Some hypotheses have been put forward trying to understand why the ordered microphases remain elusive.

1. **Dynamical arrest:** When a disordered phase is formed at high temperatures, at densities that should lead to the formation of a lamellar phase at lower temperatures, it has been observed that upon decreasing the temperature, the fluid undergoes a gelation transition with the subsequent dramatically slow down of the dynamics. Thus, the system is kinetically trapped in an arrested state and cannot continue evolving to the lamellar phase. As we discussed in this section, the dynamical arrest is often observed in experiments [42, 43, 47] where the range of attraction is very short (approximately 10-20% of the diameter of the particles). Although theoretical models with such short ranges of attraction predict the formation of the ordered

microphases [15], this hypothesis has been confirmed in simulations [39, 23, 22] using similar parameters as those reported in reference [42] experimentally. However, simulations with longer attractive ranges (above 50% of the diameter of the particles) have shown the formation of the ordered microphases with no dynamical arrested states that prevent their formation (See Chapter 5 and reference [26]). A very short attractive range favours small fluctuations that might lead to arrested states. This issue seems to be solved by enlarging the attraction range as we show in our simulations in Chapter 5. Larger attractive ranges can be achieved experimentally by synthesising colloidal particles with hydrophobic chains chemically adsorbed on the surface, as reported in reference [49].

2. **Polydispersity of colloids:** In simulations, the colloidal particles are usually considered perfectly mono-dispersed. Nevertheless, it has been shown that polydispersity can play a role on the structure of the colloidal fluid [47]. In experiments, the polydispersity is typically around 3% [42, 47]. At low temperatures, the polydispersed particles form microcrystalline gels. It has been shown that the regions of the gel that exhibit the most ordered internal structures correspond to regions of particles with low local polydispersity [47]. This is confirmed in MD simulations with a smaller polydispersity around 1%. Furthermore, simulations predict the formation of a lamellar phase due to the segregation of particles into bilayers formed by particles with relatively low local polydispersity [47]. A larger attractive range might overcome the polydispersity and finally lead to the formation of ordered microphases in experiments[47].

3. **Unaccounted interactions:** As we discussed at the beginning of this chapter, SALR interactions can be modelled by adding an attractive term at short ranges and a repulsive term at long ranges. In purely attractive and repulsive colloidal systems, it has been shown that the typical models used for attractive and repulsive interactions correspond fairly well with what is measured in experiments [9]. However, when both contributions are put together in a SALR potential, experimental measurements in colloidal systems with competing interactions reveal high discrepancies with what is expected from the SALR potential. Thus, there might be some interactions that are missed and not taken into account in the models. For example, ion condensation on the surface of the particles might lead to an inhomogeneous surface charge distribution that is not accounted for in the SALR potentials where a homogeneous surface charge is assumed [9]. Moreover, most of the experimental works on colloidal systems with SALR interactions have been carried out in non-aqueous solvents in which the electrostatic

interactions are not well understood, and some solvent effects on the SALR interactions might be unaccounted. The problem with using aqueous systems is that the Debye length is very small, and the repulsive interactions would end to be short-ranged. The use of smaller colloidal particles and solvents with intermediate dielectric constants might help to overcome this issue [9].

1.1.2 Effects of confinement

In our context, a confined system is such that interacts with surfaces, interfaces, membranes or is restricted by walls or external potentials. It is well-known that confinement affects the thermodynamic, structural and dynamic properties of confined fluids [50, 51, 52]. In the last two decades, although the interest in colloidal systems with competing interactions has substantially increased [10], most of the studies on such systems are devoted to their bulk properties, whereas the effects of confinement have been comparatively less studied. In this section, we will briefly discuss the most relevant works on confined SALR systems.

In 2007, Imperio and Reatto investigated a two-dimensional colloidal fluid with competing interactions confined in slit pores [53]. The particle-particle interactions were modelled with the double Kac potential, and the particle-wall interactions were defined so they could be either repulsive, neutral or attractive. Using Monte Carlo simulations in the canonical ensemble, (NVT), the authors concluded that, when confined, the stripe phase undergoes structural changes regarding size, periodicity and orientation of the clusters. Besides, they observed that ordered phases only appeared when the separation between confining walls was commensurate with the period of the phase, which is the key factor in the formation of ordered structures under confinement.

One year later, there were two contributions on confined systems with competing interactions by Archer and collaborators. First, a simple DFT [54] was proposed to describe the same system previously studied by Imperio and Reatto in reference [53], which was in qualitative agreement with the simulations results. Moreover, a two-dimensional system interacting via HSDY potential was studied in bulk and confined in parallel walls, using a mean-field DFT [55]. These theoretical calculations not only coincided with some previous simulations in bulk [38] but also proved the reliability of the DFT approaches to study SALR-fluids under confinement. Furthermore, Liu *et al.* studied a two-dimensional system of particles interacting via long-range electrostatic repulsion and a short-range exponential attraction under confinement in an external quadratic potential employing

Molecular Dynamics (MD) simulation, obtaining a series of ordered concentric structures whose morphology could be modulated by modifying the attraction-repulsion ratio [56].

In 2009 and 2010, Zarragoicoechea, Meyra and Kuz published a couple of contributions on Monte Carlo simulations of SALR interacting particles adsorbed on the surface of spheres. In both articles, they used a hard core contribution plus a double Kac potential to model the interactions between particles. In the first article [57], they focused on single-component systems and observed the formation of clustered and striped patterns on the surface of spheres with different radii. In the second contribution [58], the authors studied the behaviour of binary mixtures of SALR-interacting particles, in which different types of patterns were obtained depending on the values of the parameters of the model and the size of the sphere.

In 2015, Bores *et al.* studied, through grand canonical Monte Carlo simulations, the phase behaviour of a two-dimensional SALR fluid confined in disordered porous materials. The fluid particles interacted via a modified double Kac potential [59]. The results revealed that the confinement in disordered pores favoured the formation of droplets, preventing the formation of percolating phases. Later, in a couple of works by Pękalski *et al.*, a one-dimensional lattice model with isotropic SALR potential was developed to study the effects of elastic and rigid boundary conditions on the structural and thermodynamic properties of the system [60, 61]. The interactions were such that the first neighbours attract each other, and the third neighbours repel each other. The authors found bistability when the system was confined in elastic walls and thermodynamic anomalies mediated by clusters repulsion. In 2016, the authors extended the previous model to a triangular two-dimensional lattice model and studied the influence of confinement in slit pores on the properties of the SALR fluid [62]. Again, the conclusions pointed out the importance of commensurability between the pore size and the period of microphases on the formation of ordered structures.

In 2018, Pękalski and Ciach investigated two-dimensional systems composed of LJY-interacting particles on a flat and on a spherical surface [63]. The system was studied at conditions that favoured the formation of elongated clusters at low enough temperatures. An MD study revealed that at high temperatures, the flat and spherical systems behaved in a similar way from structural and thermodynamic points of view. However, at low temperatures, the system assembles into long clusters whose length eventually becomes comparable to the radius of the confining sphere, and then the curvature affects the structural properties of the adsorbed SALR fluid significantly. Lima and collaborators used Langevin dynamics simulations to study a SALR system confined by a three-dimensional harmonic potential [64]. This is the first simulation study to consider an off-lattice three-dimensional SALR fluid under confinement to the best of our knowledge. The interactions between particles were given by combining a short-range soft core potential, a mid-range attractive well potential and a Gaussian-shaped long-range repulsive potential. The authors justified such selection because previous works had used the same interactions in two-dimensional systems [65], and also by arguing that the specific mathematical shape of the interactions does not play a role on the phase behaviour of SALR systems as long as attractive and repulsive contributions are well-tuned. The results showed that the external harmonic potential promoted the formation of complex ordered structures that are not found in bulk.

In the last two years, it is worth mentioning some contributions to the field of confined systems with competing interactions. In a study by Pękalski, Bildanau and Ciach, using Monte Carlo simulations of the two-dimensional lattice model presented in reference [62], the influence of hexagonal confinement on striped patterns was investigated. The authors proposed a method for inducing the formation of spiral patterns by including triangular wedges at the hexagonal boundary vertex. In another recent paper, Ciach proposed a model based on the mean-field method to study systems with competing interactions near a planar surface [66]. As a particular case, the model was tested with the HSDY potential, finding that the correlation function had a large decay length in the longitudinal direction near the confining surface. These theoretical predictions were in qualitative agreement with Molecular Dynamic simulations of LJY-interacting particles confined in parallel walls, where one wall was attractive, and the other repulsive [67].

In the thesis, we will perform three-dimensional off-lattice MC and MD simulations of colloidal particles interacting via SALR potentials under confinement in pores with different sizes and geometries. We will be focused on purely repulsive interactions between the particles and the pore walls.

1.2 Similarity between different systems with competing interactions

The morphologies of the ordered microphases obtained in colloidal systems with competing interactions can be observed in different systems. For example, in block copolymers, upon increasing the volume fraction of one of the blocks, the ordered microphases adopt the shape of cubic-packed spheres, hexagonally packed cylinders, bicontinuous cubic networks and lamellar sheets [6]. Despite the difference in the physical nature of the interactions, these ordered microphases are strikingly similar to those predicted in colloidal systems. A comparison between colloidal systems with competing interactions and diblock copolymers, regarding the structure of the ordered microphases and the phase diagrams topology, can be found in Figure 1 of reference [17]. Block copolymers self-assembly has been extensively studied because its impact on many potential applications in nanotechnology and industry [68, 7, 69].

The origin of the similarity and universality in the phase behaviour of systems with competing interactions has been the subject of some theoretical works [15, 17]. It has been demonstrated that the microphase separation can be described by the same Landau-Brazovskii functional in amphiphilic and colloidal systems interacting through effective SALR potentials of arbitrary functional shape [17]. Thus, on mathematical grounds, the sequence of ordered microphases and the topology of the phase diagrams of systems with competing interactions are universal.

Unlike colloidal systems, in block copolymers, the length scales of the interactions are easily tuned in experiments. This can be achieved by controlling the number of monomers added to each block [70]. Although the strengths of attractive and repulsive interactions can be modified in experiments with colloids (by adding depleting agents and ionic compounds), the fine adjustment of the short-range and long-range interactions is still a challenge in three-dimensional systems [9]. This might be why the ordered microphases have been observed experimentally in block copolymers whereas in colloidal systems they remain elusive.

Theoretical[71, 72], simulation [73, 74] and experimental[75, 76, 77] studies have demonstrated the formation of novel structures when block copolymers are confined into different geometries. Particularly, helical structures under cylindrical confinement (in simulations [73], and experiments [76, 77]) have been observed, as well as arrangements of cylindrical aggregates moulded by channels with different geometries [74, 68, 72]. The structures obtained under confinement in block copolymers are strikingly similar to those obtained in the thesis. This evidence strongly supports the hypothesis that the universality in the phase behaviour of systems with competing interactions is also extended to confined systems.

1.3 Simulation techniques

Molecular Simulation (MS) has become a powerful tool exploited in different fields of science and engineering. It is not surprising, then, that MS is used to test approximations in theories, understand experimental data, and design setups at extreme conditions that would not be achievable in the laboratory [78]. In this section, we will describe, briefly, the fundamentals of MC and MD simulations used by us.

1.3.1 Monte Carlo

Canonical ensemble NVT

Let us start from the classical expression for the average value of an observable, $\mathcal{A}$, in the canonical ensemble (NVT),

$$\langle \mathcal{A} \rangle_{NVT} = \frac{\int d\mathbf{r}^N \mathcal{A}(\mathbf{r}^N) \exp\left[-\beta U(\mathbf{r}^N))\right]}{\int d\mathbf{r}^N \exp\left[-\beta U(\mathbf{r}^N))\right]}. \tag{1.1}$$

Here $\mathbf{r}^N$ is the vector that contains the positions of all N particles of the system, $\beta = 1/k_B T$ (T stands for temperature and k_B for the Boltzmann's constant), $U(\mathbf{r}^N)$ the interaction energy between particles. We note that the calculation of $\langle \mathcal{A} \rangle_{NVT}$ implies the computation of a 3N-dimensional integral, which is, in general, unattainable by analytical methods or by conventional numerical integration [78]. However, Metropolis *et al.* invented a method to calculate the integrals in equation 1.1 [79]. The canonical configurational partition function is defined as

$$Z_{NVT} = \int d\mathbf{r}^N \exp\left[-\beta U(\mathbf{r}^N))\right]. \tag{1.2}$$

We can define the probability of a given microstate as

$$\mathcal{P}_{NVT}(\mathbf{r}^N) = \frac{\exp\left[-\beta U(\mathbf{r}^N))\right]}{Z_{NVT}}. \tag{1.3}$$

Thus, we need to generate a random succession of configurations according to the probability distribution $\mathcal{P}_{NVT}(\mathbf{r}^N)$.

To generate such succession of configurations, we consider the system in a given configuration $\mathbf{r}^N_{old}$. Then, we generate another configuration $\mathbf{r}^N_{new}$ by adding a small random displacement δ to configuration $\mathbf{r}^N_{old}$. The transition probability from "old" to "new" configuration, $\Pi(old \rightarrow new)$, must obey the detailed balance condition, i.e.,

$$\mathcal{P}_{NVT}(\mathbf{r}^N_{old})\Pi(old \rightarrow new) = \mathcal{P}_{NVT}(\mathbf{r}^N_{new})\Pi(new \rightarrow old). \tag{1.4}$$

This condition ensures that in equilibrium, the number of accepted trial moves from "old" to "new" must be equal to the number of accepted trial moves from "new" to "old". The detailed balance condition underlies an acceptance criterion for MC moves, which is given by,

$$acc(old \rightarrow new) = \exp\left[-\beta(U(\mathbf{r}^N_{new}) - U(\mathbf{r}^N_{old}))\right] > \xi. \tag{1.5}$$

Where ξ is a random number uniformly distributed in $[0, 1]$. A derivation of the acceptance criterion can be found in reference [78]. In practice, an MC scheme produces a Markov chain of configurations, each configuration having a probability proportional to the Boltzmann's factor $\exp\left[-\beta U(\mathbf{r}^N)\right]$. In a Markov chain, the probability distribution of a new configuration only depends on the current configuration, without being influenced by previous configurations. A typical MC algorithm in the canonical ensemble is described as follows:

1. The system is set in an initial configuration with non-vanishing Boltzmann's factor (no overlapping of particles).
2. A particle is randomly chosen
3. Calculate the energy of the "old" configuration $U(\mathbf{r}^N_{old})$
4. Give the chosen particle a random displacement to produce a "new" configuration $\mathbf{r}^N_{new}$.
5. Calculate the energy of the "new" configuration $U(\mathbf{r}^N_{new})$
6. Generate a random number, ξ, uniformly distributed in $[0, 1]$.
7. Accept the particle displacement if $\xi < \exp\left[-\beta(U(\mathbf{r}^N_{new}) - U(\mathbf{r}^N_{old}))\right]$.
8. If the move is rejected, the "old" configuration is kept and the process is repeated.

An MC simulation can be divided into two parts. **Equilibration run:** we evolve the system from an initial configuration to an equilibrium state. In general, we acknowledge that the system is in equilibrium when the instantaneous energy reaches a plateau and fluctuates around a mean value. **Production run:** we compute the averages of the properties of interest.

Grand canonical ensemble μVT

In the grand canonical ensemble, the chemical potential (μ), the temperature (T) and the volume (V) are kept constant while the number of particles (N) fluctuates. Let us consider a system in contact with an infinite particle reservoir (See Figure 1.3).

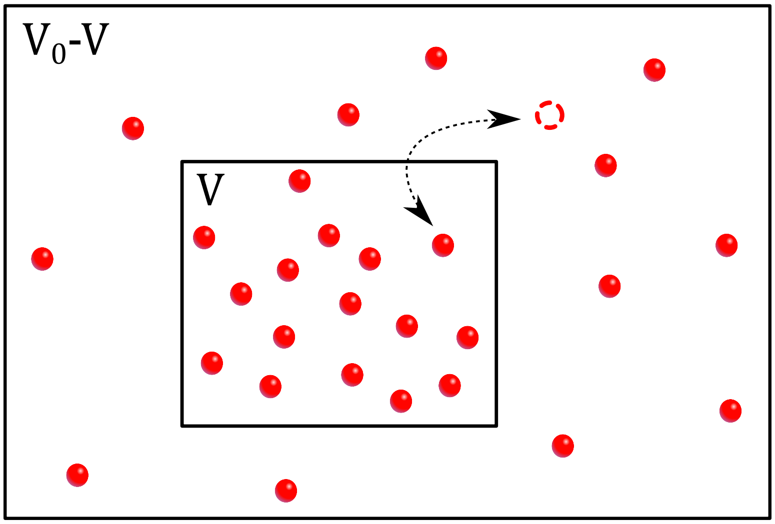

Figure 1.3: Representation of the system in contact with a particle reservoir in the grand canonical ensemble. Based on [78].

The grand canonical partition function of the system in the classical approximation can be written as [80],

$$Q_{\mu VT} = \sum_{N=0}^{\infty} \frac{\exp(\beta\mu N)V^N}{\Lambda^{3N}N!} \int d\mathbf{r}^N \exp\left[-\beta U(\mathbf{r}^N)\right] \tag{1.6}$$

Where Λ is the thermal de Broglie wavelength. The probability distribution to find the system with N particles in the configuration $\mathbf{r}^N$ can be expressed as [80],

$$\mathcal{N}(\mathbf{r}^N, N) = \frac{\exp\left[-\beta(U(\mathbf{r}^N) - \mu N)\right]V^N}{Q_{\mu VT}\Lambda^{3N}N!} \tag{1.7}$$

Equation 1.7 is the probability distribution that we need to sample following a Markov chain in which we can either add particles to the system or remove particles from the system. The corresponding probability distributions ratio gives the probability of accepting the particle exchanging moves. Thus, the probability of acceptance of an addition move is,

$$\Gamma(N \to N+1) = \frac{\mathcal{N}(\mathbf{r}^{N+1}, N+1)}{\mathcal{N}(\mathbf{r}^{N}, N)} = \frac{V}{\Lambda^3(N+1)} \exp\left[\beta(U(\mathbf{r}^{N}) - U(\mathbf{r}^{N+1}) + \mu)\right] \tag{1.8}$$

And the probability of acceptance of a removal move,

$$\Gamma(N \to N-1) = \frac{\mathcal{N}(\mathbf{r}^{N-1}, N-1)}{\mathcal{N}(\mathbf{r}^{N}, N)} = \frac{\Lambda^3 N}{V} \exp\left[\beta(U(\mathbf{r}^{N}) - U(\mathbf{r}^{N-1}) - \mu)\right] \tag{1.9}$$

It can be proven that equations 1.8 and 1.9 obey detailed balance (See reference [78] for an easy demonstration).

An example of an MC algorithm in the grand canonical ensemble is:

1. The system is set in an initial configuration with non-vanishing Boltzmann's factor (no overlapping of particles).

2. The type of MC move to be performed is randomly selected. It can be a particle displacement, a particle addition, or particle removal. Usually, the frequency of particle displacement moves is much higher than particle exchange moves.

3. If a particle displacement is selected, the algorithm described for the canonical ensemble is followed.

4. If an addition of a particle is selected, a particle is added at a random position inside the simulation box. The addition of a particle is accepted with a probability,

   $$acc(N \to N+1) = \min\left[1, \Gamma(N \to N+1)\right] \tag{1.10}$$

   In practice, we generate a random number, ξ, uniformly distributed between $[0,1]$ and accept the addition if $\xi < \Gamma(N \to N+1)$.

5. If a particle removal is selected, a particle is randomly chosen and removed. The removal is accepted with a probability,

   $$acc(N \to N-1) = \min\left[1, \Gamma(N \to N-1)\right] \tag{1.11}$$

   In practice, we sort a random number, ξ, uniformly distributed between $[0,1]$, and accept the removal if $\xi < \Gamma(N \to N-1)$.

In the thesis, we developed our MC codes in the canonical (NVT) and grand canonical ensembles (μVT), both in bulk and under confinement.

1.3.2 Molecular Dynamics

According to Lagrange's formulation of classical mechanics for conservative systems, there is a function, $\mathcal{L}$, that contains all the trajectories of the system, whose time integral, $\int \mathcal{L} dt$, is an extremum. $\mathcal{L}$ is the Lagrangian function of the system and depends on the generalized coordinates, $\{\mathbf{q}_i\}$, the generalized velocities, $\{\dot{\mathbf{q}}_i\}$, and the time, t. Thus, $\mathcal{L} = \mathcal{L}(\{\mathbf{q}_i\}, \{\dot{\mathbf{q}}_i\}, t)$. The Lagrange equations of motion can be written as,

$$\frac{d}{dt}\left(\frac{\partial \mathcal{L}}{\partial \dot{\mathbf{q}}_i}\right) = \frac{\partial \mathcal{L}}{\partial \mathbf{q}_i} \qquad \forall i \tag{1.12}$$

Lagrange function is defined as,

$$\mathcal{L}(\{\mathbf{q}_i\}, \{\dot{\mathbf{q}}_i\}, t) = \mathcal{K}(\{\dot{\mathbf{q}}_i\}) - \mathcal{V}(\{\mathbf{q}_i\}) \tag{1.13}$$

where $\mathcal{K}$ and $\mathcal{V}$ are the kinetic and the potential energy respectively. In a system composed of N particles with equal mass, m, the generalized coordinates are the positions of their centres of mass, $\mathbf{r}_i$, and equation 1.12 becomes Newton's second law,

$$\mathbf{F}_i = m\ddot{\mathbf{r}}_i = -\frac{\partial \mathcal{V}}{\partial \mathbf{r}_i} \qquad i = 1, ..., N \tag{1.14}$$

Since we usually deal with pairwise interaction potentials, the force can be expressed as,

$$\mathbf{F}_i(\mathbf{r}_i) = \sum_{j \neq i} F(|\mathbf{r}_j - \mathbf{r}_i|)\hat{\mathbf{r}}_{ij} \tag{1.15}$$

Molecular Dynamics is based on the solution of the equations of motion (Equation 1.14) [81]. A finite differences scheme to integrate the equations of motion, widely used in MD studies, is Verlet's algorithm,

$$\mathbf{r}_i(t + \delta t) = 2\mathbf{r}_i(t) - \mathbf{r}_i(t + \delta t) + \delta t^2 \mathbf{F}_i(t)/m + O(\delta^4) \tag{1.16}$$

$$\mathbf{v}_i(t) = \frac{\mathbf{r}_i(t + \delta t) - \mathbf{r}_i(t - \delta t)}{2\delta t} + O(\delta t^2) \tag{1.17}$$

These equations are obtained by Taylor-expanding the positions of the particles at $t+\delta t$ and $t-\delta t$, both truncated at order δt^4. Then, we sum these expansions to obtain equation 1.16. Similarly, from the trajectories of the particles, we can obtain equation 1.17 by subtracting the Taylor expansion of $r_i(t-\delta t)$ from the expansion of $r_i(t+\delta t)$, both truncated at $O(\delta t^2)$, and then solving for $v(t)$.

The computation of forces can be very expensive if the system is large. There are some tricks such as Verlet lists and cell lists [78] that make the calculation of forces computationally affordable. Also, to initialise an MD simulation, we have to set the initial positions and velocities of the particles, avoiding particles overlapping and huge velocities. After an equilibration run, we can compute time averages of the properties of our interest.

Due to the conservative nature of the equations of motion, an MD simulation samples the microcanonical probability distribution (NVE). However, we are usually interested in performing MD simulations in different ensembles, namely NVT or NpT. To achieve the sampling in these ensembles we can introduce thermodynamic constrains, such as a thermostat (the system is surrounded by a thermal bath) or a barostat (the system is allowed to change its volume to regulate the pressure). The mathematical procedure to include these constrains implies a reformulation of the equations of motion in terms of scaled time and coordinates, and the addition of feedback terms to the Lagrangian function. The most used algorithms in NVT and NpT MD simulations are the Nosé-Hoover thermostat and barostat. A general view of this method is presented in references [78] and [81]. For a very detailed derivation of the method, the original papers can be consulted [82, 83].

In the thesis, we use the open source MD package LAMMPS [84] to perform simulations in the NVT and NpT ensembles in bulk and under confinement.

1.4 Scope and thesis plan

What we know so far is that systems with competing interactions, no matter the origin of their interactions, such as amphiphiles, colloids, copolymers, magnetic layers, among others, present similar phase diagram topology when their attractive and repulsive contributions are adequately tuned to promote the formation of ordered microphases. Thus, we say that the phase behaviour of systems with competing interaction is universal, exhibiting different ordered phases such as cluster-crystal, cylindrical, bicontinuous and lamellar. This universality can be exploited to guide theoretical, simulation, and experimental studies in the whole spectrum of systems with competing interactions, i.e., the information obtained for one system can be used as inspiration or reference to study a different system.

Particularly, in colloidal systems with competing interactions, the fundamental link between the morphology of the ordered microphases and thermodynamic and dynamic properties is not fully understood. This is why, despite some efforts [42, 44, 41, 40, 43, 48], researchers have not observed yet ordered microphases in experiments. Although there are many works dedicated to bulk behaviour, the impact of the boundary conditions on the ordered microphases morphology is still an open question. As we reviewed in section 1.1.2, some investigations have aimed to understand the behaviour of colloidal systems with competing interactions under confinement. However, three-dimensional off-lattice systems have been comparatively less studied under confinement. We require more understanding of continuous-space systems that can be linked more accurately to experiments, and thus we can exploit the potential of colloidal self-assembly in technology. Besides that, the confinement of colloidal systems with competing interactions might help to overcome some of the issues that have hindered the formation of ordered microphases in bulk, and thus it can be a good strategy to finally obtain ordered microphases in experiments.

The research presented in the thesis is a simulation study; we employ both MC and MD simulations. The scope is to gather evidence that helps to understand the effects of confinement on the self-assembly of colloidal particles with competing interactions, with the purpose of finding relations between the colloidal fluid properties (structural, thermodynamic and dynamic) and the morphologies of the confining pores. The models we study in the thesis are three-dimensional off-lattice. We look for novel structures induced by confinement and strategies to direct the assembly of the bulk ordered microphases. Additionally, we want to prove whether the phase behaviour universality in bulk can also be extended to confined systems, taking as reference studies on confined block copolymers in which new structural properties have been observed [68, 74, 76, 7].

We divide the thesis into two parts: Part I is devoted to MC simulations and Part II to MD simulations. In Part I, we confine the system into channels with different cross-section geometries (Chapter 2), into spherical and ellipsoidal shells (Chapter 3), and into bicontinuous porous networks (Chapter 4). In this part, we are focused mainly on thermodynamic and structural properties.

In Part II, composed of Chapter 5, we present an MD study where structural, thermodynamic and dynamic properties of the colloidal fluid are studied both in bulk (section 5.2) and under confinement (section 5.3) in infinite slit pores.

Finally, in Chapter 6 the thesis is summarised.

Part I

MC Simulations

Chapter 2

Confinement in channels with different geometries

In this chapter, we study, via Monte Carlo simulations, the structural behaviour of colloidal systems with competing interactions under confinement in channels with circular, elliptical, triangular, hexagonal and squared cross-sections. We focus on the hexagonal phase since we observed in preliminary simulations that it exhibits the most versatile behaviour under confinement in terms of formation of novel structures.

2.1 Model and simulation method

The colloidal system we are modelling here is composed of perfectly mono-dispersed spherical particles which interact with each other via a spherical-symmetrical SALR interaction potential. In particular, we consider the square-well-linear(SWL) potential, consisting of a hard core, an attractive square-well, and a repulsive ramp. The pair potential is given by,

$$u_{SALR}(r_{ij}) = \begin{cases} \infty, & r_{ij} \leq \sigma \\ -\epsilon, & \sigma < r_{ij} \leq \lambda\sigma \\ \zeta\epsilon(\kappa - r_{ij}/\sigma), & \lambda\sigma < r_{ij} \leq \kappa\sigma \\ 0, & r_{ij} > \kappa\sigma \end{cases} \tag{2.1}$$

Here r_{ij} denotes the distance between particles i and j, λ the attraction range, κ the repulsion range, ζ the repulsion strength, σ the diameter of the colloidal particles and ϵ the depth of the energy well.

All the thermodynamic quantities are reduced using ϵ and σ as units of energy and distance respectively. We set the values $\zeta = 0.05$, $\lambda = 1.5$ and $\kappa = 4.0$, because the phase diagram of the bulk system was calculated for this set of parameters in Ref [24], and can be used as a point of reference to study the behaviour under confinement.

Some readers might think that this potential is unrealistic and does not have an experimental counterpart. In particular, various researchers opt to model the inter-particle interactions with the combination of Lennard-Jones and Yukawa potentials, since it is easier to relate the parameters of this model with some quantities measurable in experiments. On the other hand, the attractive range that we use is relatively large compared to simulation works[23] that have described qualitatively well experimental studies [42]. In the first place, we need to clarify that the works above mentioned explored different thermodynamic conditions, they were focused on the transitions from clustered phases to gel-like phases, which typically occurs at higher temperatures. Besides, the choice of parameters they used favours gelation over microphase separation [18]. Thus, we need to find an appropriate balance between the attraction and repulsion to find the ordered phases we are interested in, which implies, among other things, a longer attractive range. In the second place, as we will discuss in Chapter 5, we have simulated the Lennard-Jones + Yukawa system with the appropriate choice of parameters, and we have obtained the same qualitative phase behaviour both in bulk and in confinement. Additionally, we can not forget that diblock copolymers behave similarly to the colloidal system we are simulating in this chapter. In the case of copolymers, it is easier to tune the attractive and repulsive ranges to realize experimental systems with the interaction potential studied by us.

The Monte Carlo simulations were performed in the grand canonical ensemble (μVT). The colloidal fluid is confined in channels with different cross-sectional geometries and sizes, which are modelled as hard, impenetrable walls. The simulated systems contained between 150 and 4000 particles. We first carried out an equilibration run whose length depends on the system size. The production run, where averages are taken, consisted of 1×10^9 MC steps. In this study, an MC step is either one particle displacement, one particle addition or one particle deletion. We set the displacement attempt probability at 95% and the remaining 5% to the particle exchange attempt. A particle exchange move can be either addition or deletion with a probability of 50%.

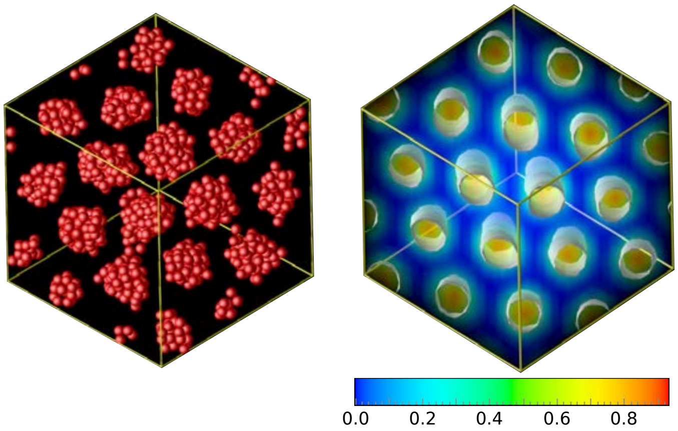

Figure 2.1: Hexagonal phase obtained in bulk at $T = 0.35$, $\mu = -2.100$ and $L = 20\sigma$. In the left panel an equilibrium snapshot is shown. In the right panel the average local density is represented along with the iso-density surface (in white) at $\rho_{iso} = 0.4$. The color indicates the values of the average local density according to the color map below. The ensemble average energy per particle is $\langle u \rangle = -3.273$ and the ensemble average density $\langle \rho \rangle = 0.211$.

We explored the behaviour of the cluster-crystal, hexagonal and lamellar phases in bulk and under confinement in different types of channels. The conclusion of this exploratory study of the phase behaviour under confinement is that the most interesting phase to study is the hexagonal one. Thus, we chose the thermodynamic conditions $T = 0.35$ and $\mu = -2.100$, which are located at the centre of the stability region of the hexagonal phase according to the phase diagram reported in [24]. Since identifying the structure of the fluid by direct observation of snapshots is often difficult, we use the local density and iso-density surfaces to help the visualization of the ordered phases. To calculate the local density, we divide the simulation box into small cubic volumes (σ^3) for which we calculate the density averaging over independent equilibrium configurations. In Figure 2.1 we show the hexagonal phase viewed as a sanpshot of the configuration of particles (left panel) and as a local density profile (right panel).

2.2 Confinement in cylindrical channels

The first type of confinement that we study, due to its simplicity, is cylindrical. The particles are confined in a hollow cylinder with hard walls. Now we have two geometrical parameters to modulate the structure of the colloidal fluid: the radius, R, and the length, L_z, of the confining cylinder. We consider both axially periodic cylinders, i.e., applying periodic boundary conditions along the cylinder axial direction, and finite cylinders placing planar walls at both ends of the cylinder. This section is based on reference [85]

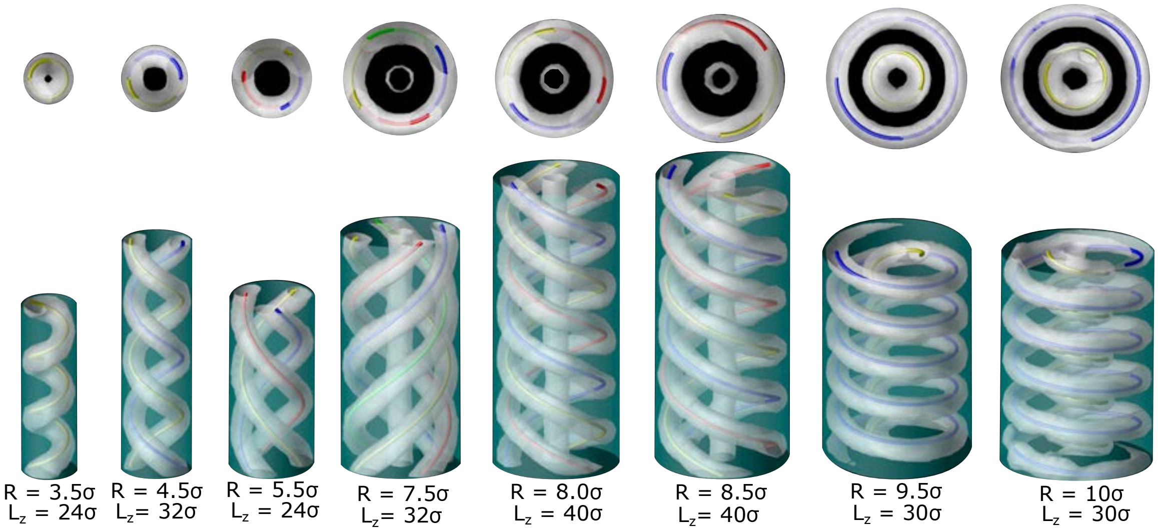

Figure 2.2: Possible configurations of the hexagonal phase under cylindrical confinement for different values of the cylinder radius $3.5\sigma \leq R \leq 10\sigma$ for axially periodic pores. The gray surface shows points with local density $\rho_{iso} = 0.40$. Two different views of each configuration are depicted: along the parallel (bottom images) and perpendicular (top images) directions to the cylinder axis. The length of the confining cylinder is $24\sigma \leq L \leq 40\sigma$.The thermodynamic conditions are $\mu = -2.10$ and $T = 0.35$.

Initially, we study how the structure of the colloidal fluid is affected by variations in the radius, R. The summary of the results is presented in Figure 2.2.

As we can observe in Figure 2.1, at the chosen thermodynamic conditions the particles self-assemble in straight cylinders that are arranged in a hexagonal lattice in bulk [24]. For the same conditions, our calculations show that the cylindrical confinement modifies the formation of straight cylinders within the range $3.5\sigma < R < 10\sigma$, promoting instead the formation of helical structures. When $R < 3.5\sigma$, the size of the confining cylinder is comparable to the equilibrium diameter of the cylindrical aggregates in bulk hexagonal phase ($d_0 = 3.40\sigma$), and particles still form one straight cylindrical aggregate. In the case of such tight confinement, the geometrical restrictions are incompatible with any non-straight arrangement. Nonetheless, when the pore size is comparable to the equilibrium distance between neighbour cylinders in the bulk hexagonal phase ($l_0 = 6.20\sigma$), the fluid undergoes through a structural transition to helical arrangements. As the radius of the confining cylinder, R, becomes larger, the system self-assembles into single or multiple helical structures. The system follows a layered concentric growth pattern. First, one layer is formed which can be a single helix ($R = 3.5\sigma$), a double ($R = 4.5\sigma$) helix or a triple helix ($R = 5.5\sigma$) depending on the size of the pore. Then, for $R \geq 5.5\sigma$, a straight cylindrical aggregate is formed at the centre of pore and a second layer of helices grows close to the wall of the confining cylinder. This central straight cylindrical cluster survives over a relatively broad range of radii, until, at a given radius, a transition into a second helical structure, which is concentric to the outer helix, takes place. The multi-helical structures that we obtained here are remarkably similar to those obtained in confined di-block copolymers [68] and surfactant composites [75]. We emphasize that the behaviour of all these systems is governed by competing interactions, although the physical origin is different in each case (See Chapter 1 for a further discussion on this topic). Although we have considered here the simplest case of confinement (hard walls), it seems reasonable that the main features will not change for a more realistic soft confining potential. We have indirectly demonstrated that when the system is confined in a soft potential, it behaves practically in the same way. When the radius, R, of the pore is sufficiently large to accommodate two layers of concentric helical structures ($R = 9.5\sigma$ and $R = 10\sigma$ in Figure 2.2), the inner helix is, in fact, confined by the outer helix, which acts as a soft confining potential. Our results suggest that the inner single helix will transform into a double helix and then into a triple helix as the radius of the confining cylinder increases, behaving the same as the helical structures for $3.5\sigma \leq R \leq 5.5\sigma$ which are directly confined by the cylinder hard wall.

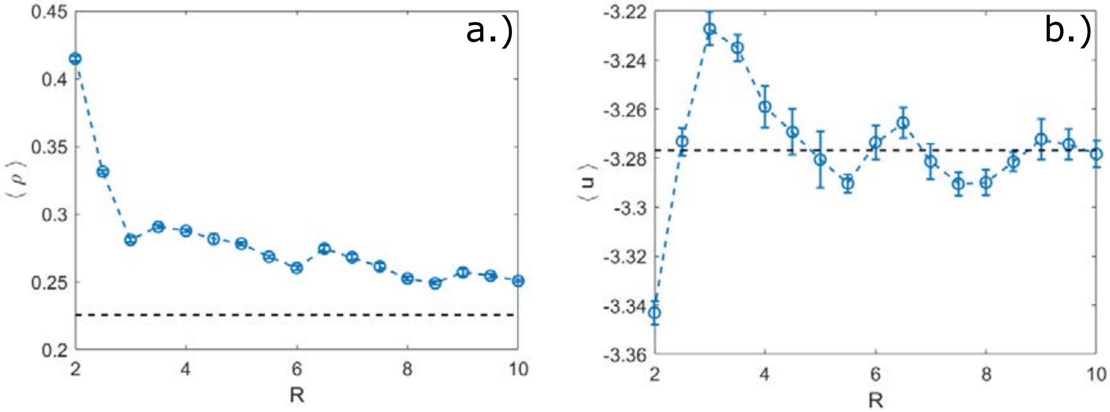

Figure 2.3: **a.)** Average density and **b.)** average energy as a function of the radius of the confining cylinder. The thermodynamic conditions are $T = 0.35$, $\mu = -2.100$ and $L_z = 20\sigma$. The dashed lines are the values in bulk at the same conditions.

It is interesting to note that the helical structures formed by colloidal particles can be fitted by parametric equations of a helix,

$$
\begin{aligned}
x(t) &= a\cos t \\
y(t) &= a\sin t \qquad\qquad t \in (0, 2\pi) \\
z(t) &= bt
\end{aligned}
\tag{2.2}
$$

Where t is the independent variable, a is the radius and $2\pi b$ describes the pitch of the helix. Fits of the helical structures using the previous equations are shown in Figure 2.2 with different colours (red, green, blue and yellow). It proves that the structures are almost mathematically perfect helices. Something that can call the attention is the fact that the length of the confining cylinder is not the same for all the studied radii. From our calculations, we noted that when multi-helical structures are formed (double, triple, tetra, etc.), the length of the confining cylinder must be commensurate with the periodic boundary conditions to avoid stress. Sometimes, this stress can lead to distorted configurations.

Now, we study the dependence of the energy and density with the radius of the confining cylinder while the length is kept constant ($L_z = 20\sigma$). This length is chosen for the sake of simplicity, although for some radii it might lead to incommensurability. The average density is calculated in such a way the hard cores of the particles are taken into account when they are placed close to the cylinder wall. It means that the centres of the particles can be placed at the boundary of the cylinder and then the actual radius of the confining cylinder is $\frac{\sigma}{2}$ greater than the value of the radius for which we define the infinite potential.

The results are shown in Figure 2.3. We can monitor the structural transitions following the behaviour of both the energy and the density. The first thing we note is that the density under confinement is always higher than in bulk at the same thermodynamic conditions but it tends to the bulk value as the radius increases. On the other hand, the energy oscillates around the value of the bulk as the radius increases.

There are three points of interest that we can note:

1. At $R = 3.5\sigma$, we observe a transition from a single straight cylindrical aggregate to a single helix. The additional particles to form the helix coils, causes the increase of the density (See Figure 2.3a), improving the system packing. However, the energy is rather high (See Figure 2.3b), meaning that the helix pitch is not optimal for the given length. The energy reaches its first minimum at $R = 5.5\sigma$, value for which the system assembles into a triple helix. This configuration is favourable energetically because the three helices are separated by an

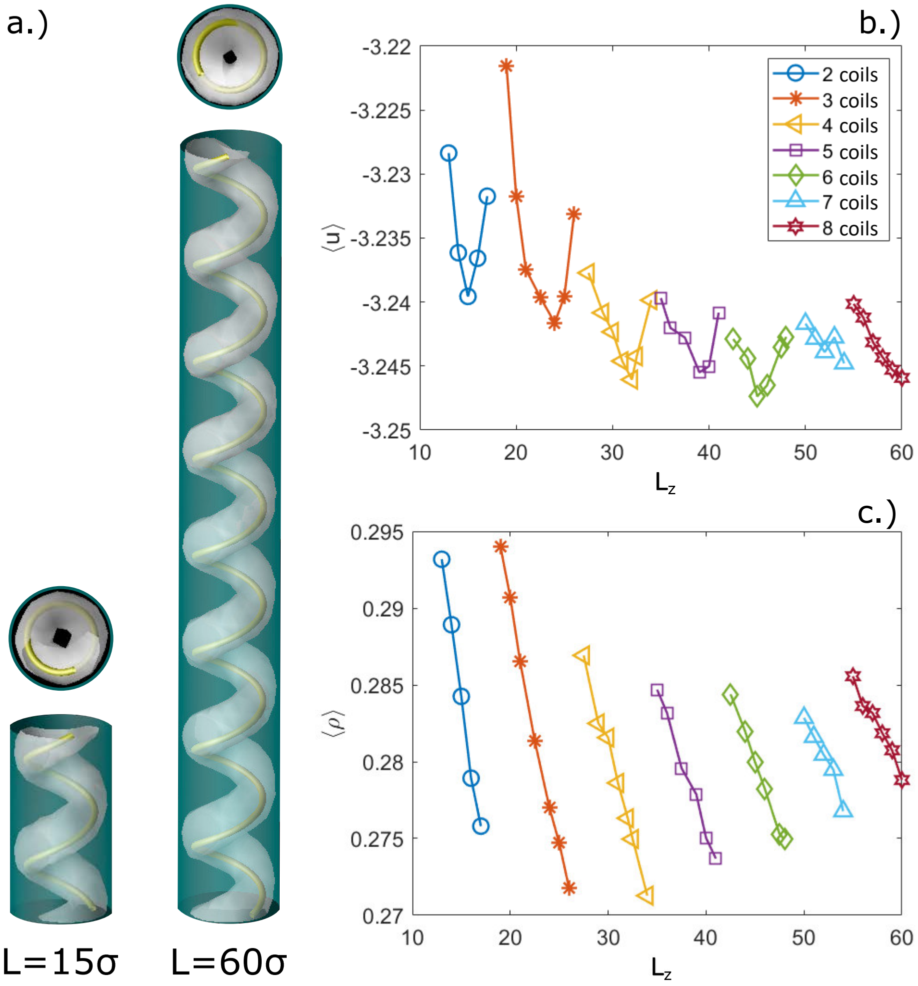

Figure 2.4: **a.)** Single helices formed in cylindrical channels of radius $R = 3.5\sigma$, at two different cylinder lengths. The gray surface shows points with local density $\rho_{iso} = 0.4$. Front and top views are presented. **b.)** The average energy as a function of the confining cylinder length. **c.)** The average density as a function of the confining cylinder length. The evolution of the number of coils is included in the colour code.

appropriate distance which avoids high repulsion.

2. At $R = 6.5\sigma$, a second layer grows in the form of a central straight cylindrical aggregate. We observe a small peak in the density while the energy has an increasing tendency. The energy reaches its second minimum at $R = 8.0\sigma$ when a triple helix surrounds the central straight cluster.

3. At $R = 9.0\sigma$, a structure with two single concentric helices is formed, and the density increases by the additional particles necessary to form the coils of the inner helix. This structure relaxes energetically at $R = 10\sigma$ with a value of energy close to its bulk counterpart.

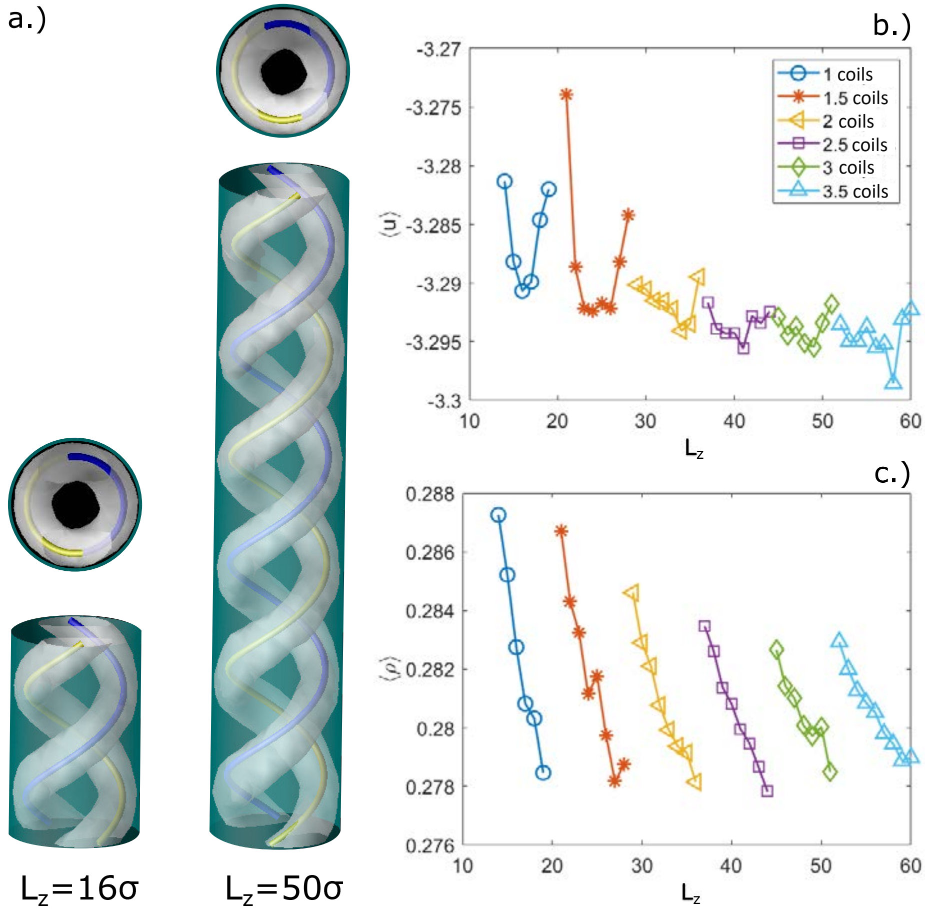

Figure 2.5: **a.)** Double helices formed in cylindrical channels of radius $R = 4.5\sigma$, at two different cylinder lengths. The gray surface shows points with local density $\rho_{iso} = 0.4$. Front and top views are presented. **b.)** The average energy as a function of the confining cylinder length. **c.)** The average density as a function of the confining cylinder length. The evolution of the number of coils is included in the colour code.

We continue our study by analyzing the effect of the confining cylinder length in axially periodic pores on the structure of the colloidal fluid for two representative values of the radius. As the helical structures are periodic in the axial direction, it is natural to expect that the structure of the helices can be affected by variations in the length of the channel.

For a narrow pore ($R = 3.5\sigma$), for which a single helix is formed, we present the results in Figure 2.4. We depict the evolution of the average energy (2.4b) and the average density (2.4c) with the length while we monitor the number of coils that each helix has. We observe that the single helix is stable for all the lengths considered. However, the pitch of the helix is strongly affected by variations in the length, causing an increase of energy when the equilibrium pitch of the helix is not commensurate with the length of the channel. As a result, the helical structure behaves like an elastic spring that can be stretched or shortened with the respective energy increment. It means that for a given number of coils, there is a unique length (or a small length range) for which the energy is minimal, either shortening or lengthening such length will cause an energy increase. Thus, when the pitch is unnaturally long, the structure becomes unstable, and a new helix is formed with one additional coil (See Figure 2.4b).

We perform the same study for a cylinder with a larger radius, $R = 4.5\sigma$. In this case a double helix is formed (See Figure 2.5). Simulations varying the confining cylinder length again reveal that the double helix is always formed for all the lengths considered. Similarly to the single helix, the double helix also behaves like an elastic spring (See Figure 2.5b), experiencing pitch variations accompanied by energy increases. Unlike the single helix, the double helix adds half coils as the length increases, although the structures differing by half coil are topologically different. Let us explain this taking the double helices depicted in Figure 2.5a as example. The structure on the left($L_z = 16\sigma$) has one coil while the structure on the right ($L_z = 50\sigma$) has three coils. In both cases, we can observe that at the ends of the cylinders, the blue helix is connected by periodic boundary conditions to itself, and the same occurs for the yellow helix. However, if we either extend the shorter structure by half a coil or cut the longer structure by the same distance, we shall observe that the blue and the yellow helices will connect through periodic boundary conditions, a fact that is topologically different from the case in which each helix is connected to itself. Nevertheless, the addition of a half coil does not compromise the stability of the structure and affects negligibly the thermodynamic properties as we can see from Figure 2.5b and c.

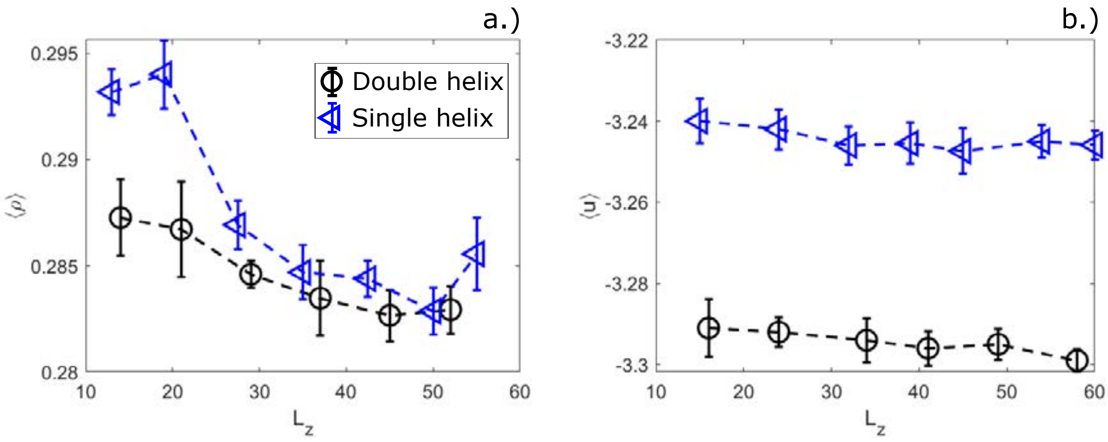

Figure 2.6: **a.)** Average energy local minima as a function of the cylinder length.**b.)** Average density local maxima as a function of the cylinder length. The radii of the pores are $R = 3.5\sigma$ for the single helix and $R = 4.5\sigma$ for the double helix.

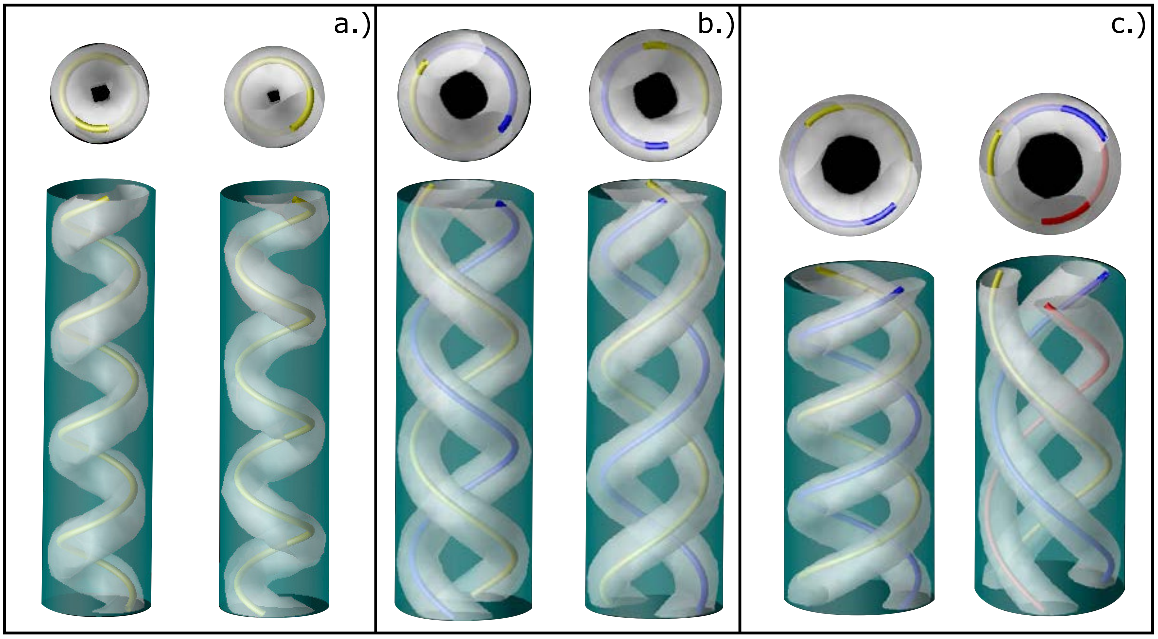

Figure 2.7: **a.)** Left- and right-handed single helices obtained for a confining cylinder with $R = 3.5\sigma$ and $L_z = 30\sigma$. The thermodynamic properties coincide within the error for both configurations, for the right-handed $\langle\rho\rangle = 0.281$ and $\langle u\rangle = -3.242$, and for the left-handed $\langle\rho\rangle = 0.280$ and $\langle u\rangle = -3.241$. **b.)** Left- and right-handed double helices obtained for a confining cylinder with $R = 4.5\sigma$ and $L_z = 30\sigma$. The thermodynamic properties coincide within the error for both configurations, for the left-handed $\langle\rho\rangle = 0.283$ and $\langle u\rangle = -3.290$, and for the right-handed $\langle\rho\rangle = 0.281$ and $\langle u\rangle = -3.290$.**c.)** Example of two different configurations obtained for the same set of geometrical parameters of the confining pore at $R = 5.5\sigma$ and $L_z = 26\sigma$. The thermodynamic properties for the configuration with two helices are, $\langle\rho\rangle = 0.268$ and $\langle u\rangle = -3.286$, and for the configuration with three helices, $\langle\rho\rangle = 0.265$ and $\langle u\rangle = -3.295$. All the results depicted in this figure were obtained at $\mu = -2.10$ and $T = 0.35$.

If we focus on the density plots for the single (Figure 2.4c) and double (Figure 2.5c) helices, we observe that, for a given number of coils, neither the maximum nor the minimum density corresponds with the energetically preferred length. Instead, for such lengths, the average density acquires intermediate values. Furthermore, in both cases, the addition of a new coil in the helices is always accompanied by a substantial increase of density, which can be explained by the larger number of particles needed to build the new coil.

With the previous results, we can make an approximate estimation of the equilibrium pitch for both the single and double helices. We notice that the energy minima and the density maxima appear for lengths that follow a period. On one hand, each energy's local minimum corresponds to the most stable helix with a given number of coils. On the other hand, the density's local maxima represent the best system packing for a given number of coils. Thus, we can estimate the helices pitch by two different criteria: the lowest energy and the highest system packing.

We extract the local minima of the average energy from Figures 2.4b and 2.5b and the local maxima of the average density from Figures 2.4c and 2.5c, and then we depict them in Figure 2.6. Thus, we adopt a criterion of minimum energy per particle to estimate the pitch for each type of helix. By measuring the distance between energy minima, we estimate that the periodicity of the single helix is $L_p \approx 7.5\sigma$ and the periodicity of the double helix is of the order of $L_p \approx 16\sigma$. We remind the reader that the distances measured for the double helix case are half periods as specified before.

Since we are dealing with helices, the question about handedness must be discussed. In our simulations, the helices were either right- or left-handed without any preference for either one. We have found that regardless of the handedness, the stability and thermodynamic properties remain the same. An example of two helical structures that are mirror images is presented in Figure 2.7a for a single helix and 2.7b for a double helix. For concentric helical structures, we found that the handedness of the inner and outer helices was always the same.

Another interesting fact that we want to comment is that, for large enough pores ($R \geq 5.0\sigma$), it is common that the colloidal fluid can assemble into more than one stable structure for a given set of geometrical pore parameters at the same thermodynamic conditions. In Figure 2.7c, we present an example of two configurations existing for the same pore dimensions and thermodynamic conditions. The existence of two or more types of structures occurs over a wide range of radii, not only in cases consisting of one-layered helical structures but also in cases where concentric helical structures are formed in larger pores. When this phenomenon happens, the thermodynamic properties are rather similar (See Figure 2.7c). We can speculate that, in systems with competing interactions, one can observe two or more structures with the same free energy. To check this hypothesis, extensive calculations of free energy for different radii and lengths of the confining cylinder are required.

Finally, we consider the case of a finite cylinder whose ends are closed by hard planar walls. The external potential is infinite for $z = 0$ and $z = L$. Only with this change, we can reconfigure the original structure. For the cylinder with $R = 3.5\sigma$, disk-like clusters are formed at the ends of the channel. The particles inside the cylinder can arrange in either a succession of disk-like clusters along the cylinder or a single helix. The formation of one sort of structure or the other depends on the pore length (See Figure 2.8a). We might think that for very long pores, when the axially infinite cylinder limit can be assumed, the particles will always self-assemble into helical structures.

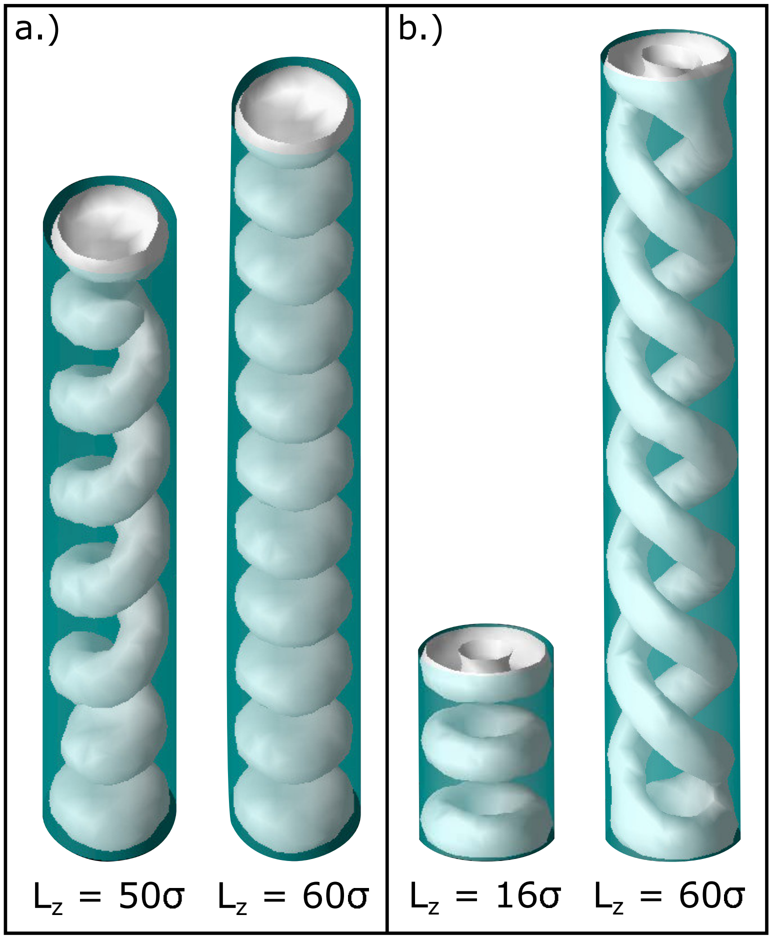

Figure 2.8: **a.)** Structures formed in closed cylindrical pores with $R = 3.5\sigma$. On the left a truncated single-helix and on the right a structure formed by a succession of disk-like clusters.**b.)** Structures formed in closed cylindrical pores with $R = 4.5\sigma$. On the left a structure composed of toroidal clusters and on the right a truncated double-helix.

Surprisingly, our results show that structures composed of only disk-like clusters are stable even for very long pores. We speculate that these structures appear when the length of the channel and the preferred pitch of a helix do not match.

Similarly, for $R = 4.5\sigma$, when the cylindrical channel is closed at the ends, the system can adopt two types of configurations: toroidal clusters along the cylinder and truncated double-helices with two tori at the ends. These configurations are presented in Figure 2.8b. For this case, we did not obtain toroidal clusters for long pores, suggesting that the double helix is more stable than that.

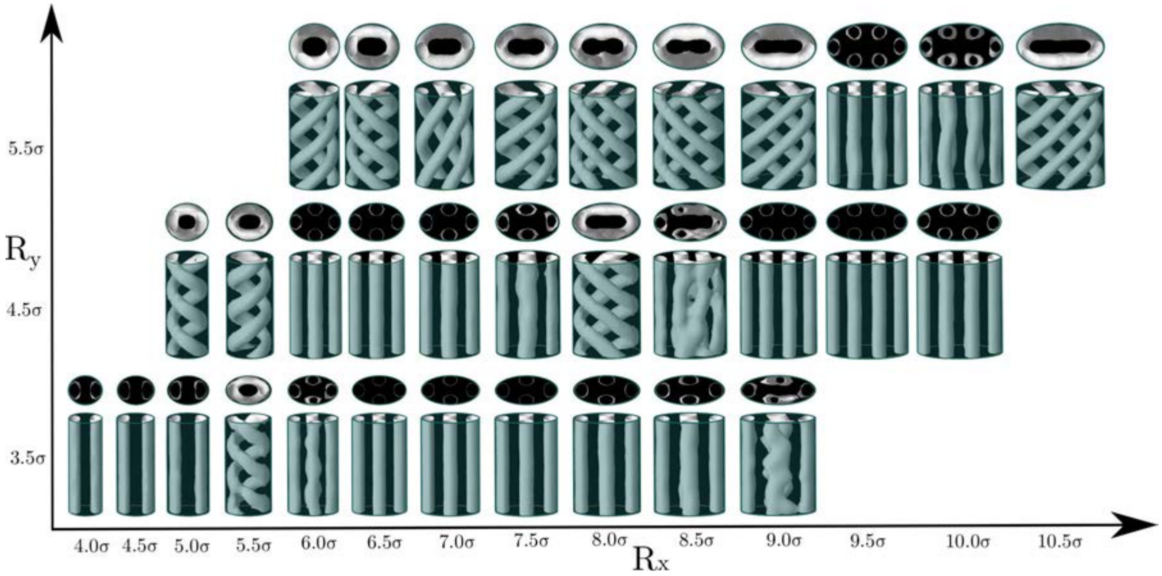

Figure 2.9: Set of structures of cylindrical aggregates confined in hard elliptical channels. The gray surface corresponds to an iso-density surface with $\rho_{iso} = 0.4$.The length of the the channel is $L_z = 24\sigma$. Periodic boundary conditions are applied along the axial direction. Two views of the structures are depicted. Three values of R_y were investigated and in each case R_x is varied between $R_y + \sigma/2$ and $2R_y$ approximately. The thermodynamic conditions are $T = 0.35$ and $\mu = -2.10$.

2.3 Confinement under different cross-sectioned channels

After having explored the behaviour of the colloidal fluid while confined in cylindrical pores, it is natural to continue studying the influence of the geometry of the pores on the ordered microphases. In this section, we will consider channels with elliptical, hexagonal, triangular and squared cross-sections. Additionally, we will confine the system in cylindrical channels, but this time we include wedges as obstacles for the fluid. We investigate three types of wedges to understand how the system modulates its structure when curved, and flat walls are present simultaneously. This section is based on reference [86].

In the previous section, we found out that, under cylindrical confinement, the colloidal particles assemble into helical structures whose equilibrium and topological properties depend on the length and radius of the confining pore. Specifically, we found that single helical structures have a preferred pitch of around 7σ to 8σ. We also observed that when multiple helices are formed, the pitch is a multiple integer of the preferred pitch of a single helix. Using this empirical rule, and as we are expecting that helical structures will still form in some of the channels we are analyzing in this section, we set the length to $L_z = 24$ for all studied cases.

We start this section presenting the results for the elliptical channels. Now we have two radii

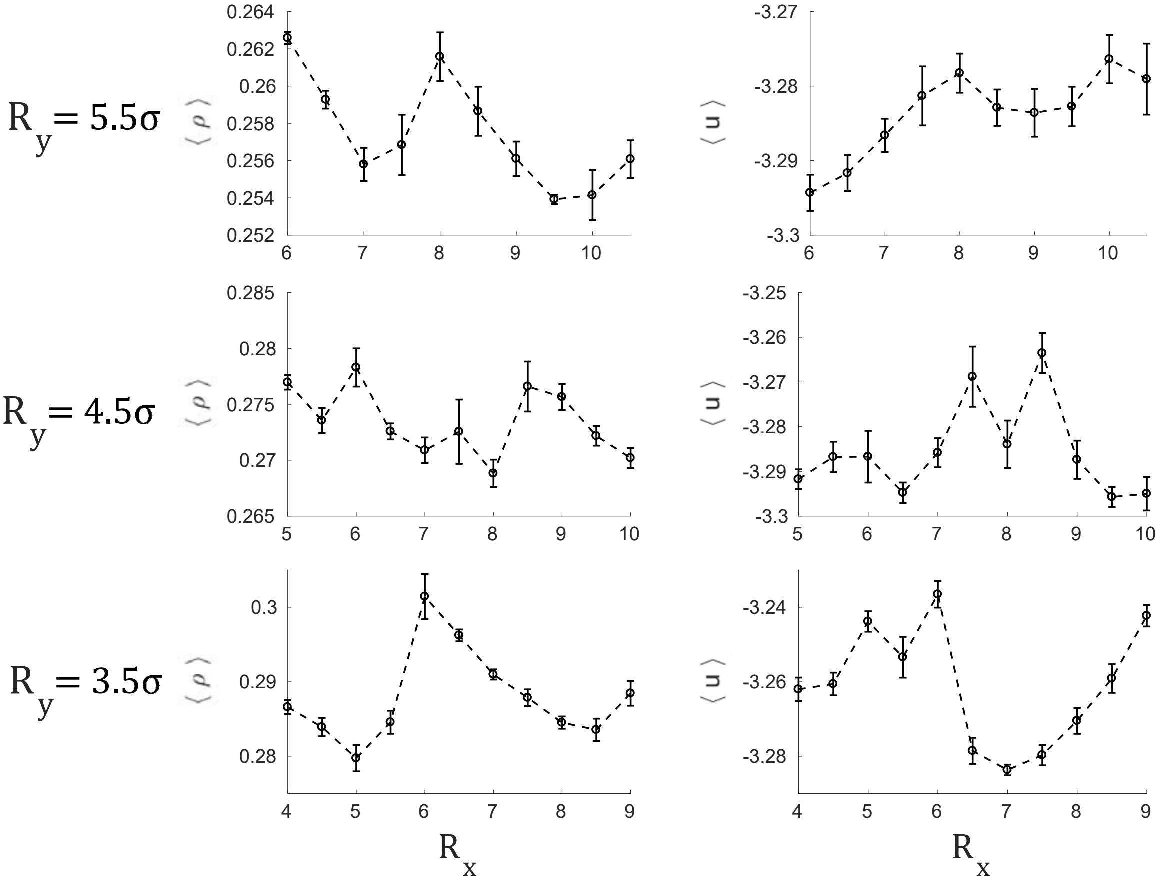

Figure 2.10: Average density, $\langle\rho\rangle$, and average energy, $\langle u\rangle$ as functions of the radii of the elliptical pores.

to play with: the semi-major axis, R_x, and the semi-minor axis, R_y. We consider three values of $R_x = 3.5\sigma$, 4.5σ and 5.0σ. For each of these values, we elongate the channel cross-section by increasing R_x up to $2R_y$ approximately. We present the results in Figure 2.9. As can be seen, some channels hold helical structures, but some others promote the formation of straight cylindrical clusters. The latter structures are often formed when the elliptical cross-section exhibits large eccentricities. We stress that neither an ellipse nor a circle match the symmetry of the hexagonal phase in bulk. This mismatching causes frustration on the original morphology of the hexagonal phase and deforms it into different structures depending on the geometrical parameters.

In bulk, we estimated that the distance between nearest cylindrical clusters in the hexagonal phase is $L_0 \approx 6.2\sigma$, and the radius of the cylinders is $r_0 \approx 1.70\sigma$. These measurements were taken at the same thermodynamic conditions as the confined system ($\mu = -2.10$, $T = 0.35$), using density plots with isosurface $\rho_{iso} = 0.4$. Thus, we expect that the formation of straight cylindrical

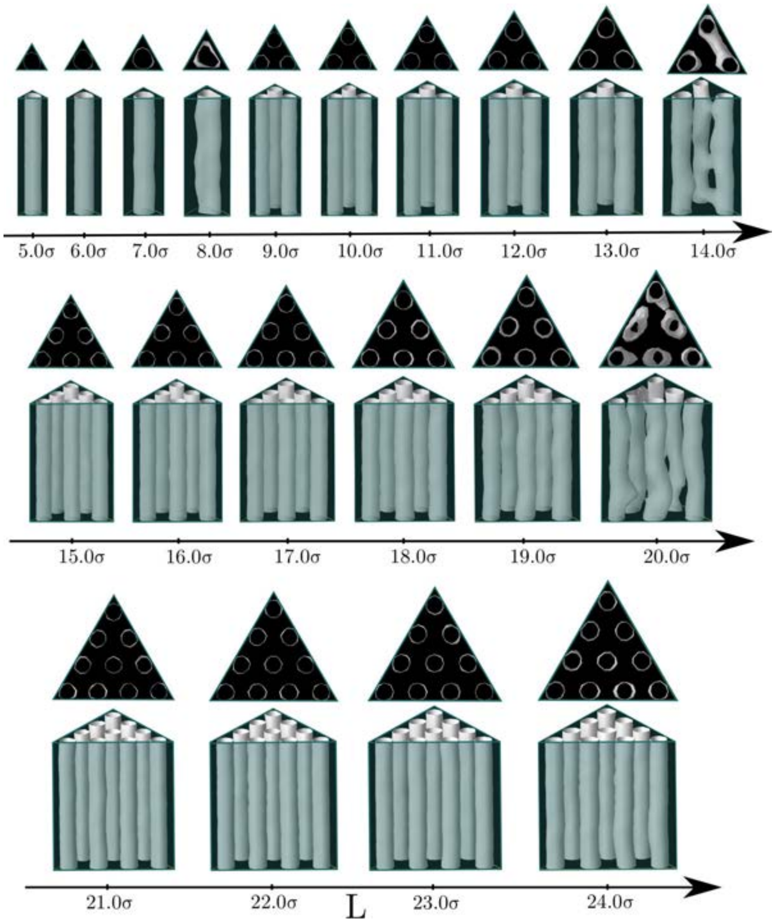

Figure 2.11: The structure of colloidal clusters confined in channels with equilateral triangular cross-sections. The gray surface corresponds to an iso-density surface with $\rho_{iso} = 0.4$. Two views of the structures are depicted. Side lengths, L, between 5σ and 24σ are presented. The length of the channel is $L_z = 24\sigma$. Periodic boundary conditions are applied along the axial direction. The thermodynamic conditions are $T = 0.35$ and $\mu = -2.10$.

aggregates occurs when the cross-section of the channels is chosen to accommodate an integer number of straight cylinders of radius r_0, separated by a distance L_0. Nevertheless, the elliptical channels can still promote the formation of straight cylinders if these conditions are not perfectly fulfilled. In such cases, the system self-assembles into either an array of clusters with elliptical cross-section (See for example Figure 2.9, $[R_y = 3.5\sigma,\ R_x = 7.5\sigma]$) or an array of cylindrical clusters with a smaller radius than in bulk (See for example Figure 2.9, $[R_y = 4.5\sigma,\ R_x = 9.0\sigma]$). Also, the configuration of the straight cylinders can be attained by shortening the distance between the nearest clusters. This usually happens with the clusters that are placed along the semi-minor radius for high eccentricities.

Comparing the results obtained for circular cross-section with those for elliptical channels, we note that in the first case the straight cylindrical clusters only appear in the centre of the pores.

Meanwhile, in the second case, the straight cylindrical clusters can form close to the pore surface. We attribute this phenomenon to the fact that an ellipse has regions of different curvatures, unlike the circle. Based on our results, it seems that the straight cylindrical aggregates find nucleation points in the regions of high curvature. Naturally, the size of the pore must be such that it can accommodate an integer number of cylindrical clusters separated by a distance close to the equilibrium distance in bulk, L_0. On the other hand, when the dimensions of the cross-section of the pore are incommensurate with the bulk phase geometrical parameters, helical structures are formed instead (See for example Figure 2.9, $[R_y = 4.5\sigma,\ R_x = 8.0\sigma]$). There is an extreme case of incommensurability in which neither helical nor straight structures are formed, but highly distorted configurations (See for example Figure 2.9, $[R_y = 4.5\sigma,\ R_x = 8.5\sigma]$). Another remarkable difference is that in cylindrical pores we obtained up to three intertwined helical aggregates without a cylindrical cluster in the centre, whereas in the elliptical channel we can obtain more complex structures with up to five intertwined helices (See Figure 2.9 $[R_y = 5.0\sigma,\ R_x = 10.5\sigma]$). We present the results of the average energy and density as functions of the radii of the elliptical channels in Figure 2.10. From these results, we observe that configurations with straight cylindrical aggregates are energetically preferred over the helical structures since they usually show lower average energies. On the other hand, the distorted configurations exhibit higher energies and, then, are less favoured than the helical structures. Helical structures often correspond to energy local minima between two distorted configurations. Regarding the average density, the structures with the highest packing use to be either distorted or helical. Very often the density maxima correspond to distorted intermediates in transitions from straight cylinders to helical structures or vice versa.

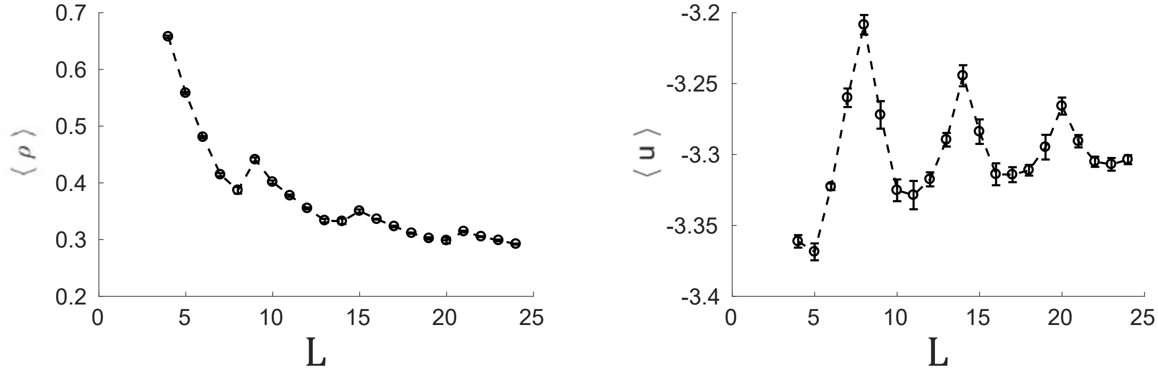

Figure 2.12: Average density,$\langle\rho\rangle$, and average energy,$\langle u\rangle$, as functions of the side length of the triangular pores.

Up to this point, we have confined the system into pores whose shape is incompatible with the symmetry of the bulk hexagonal phase. Thus, we decide to study what happens when the system is confined in pores that are coherent with the symmetry of the bulk phase. Beforehand, we intuitively expect that the confined system maintains the same symmetry as in bulk, for a wide range of pore sizes. To check this hypothesis, we study the system under confinement in triangular and hexagonal cross-sectioned channels.

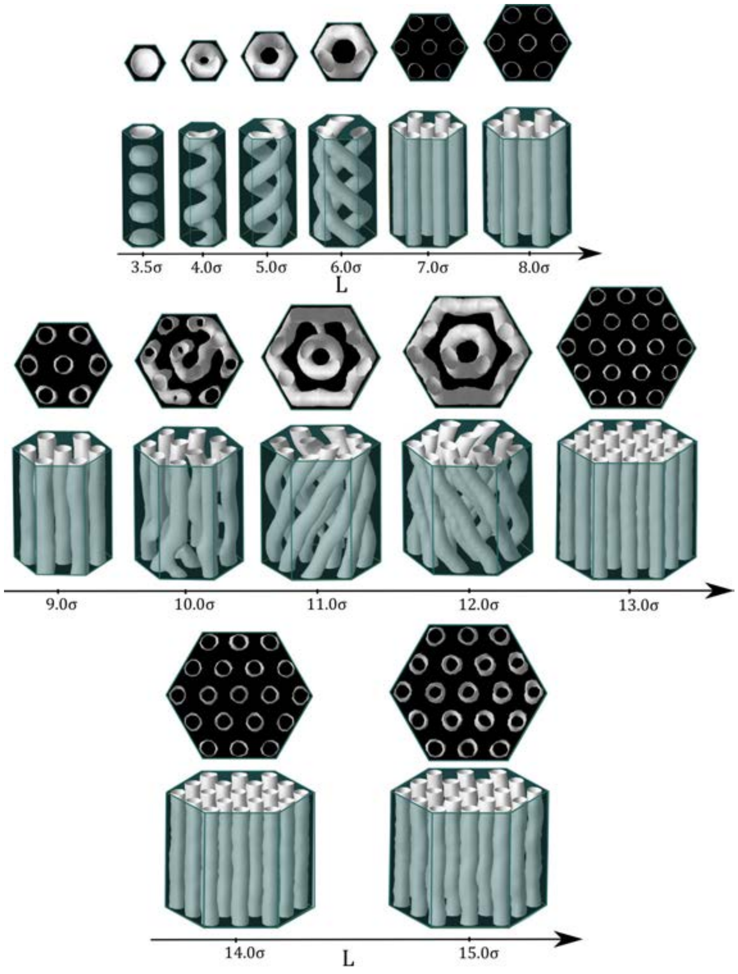

Figure 2.13: The structure of colloidal clusters confined in channels with hexagonal cross-sections. The gray surface corresponds to an iso-density surface with $\rho_{iso} = 0.4$. Two views of the structures are depicted. Side lengths, L, between 3.5σ and 15σ are presented. The length of the channel is $L_z = 24\sigma$. Periodic boundary conditions are applied along the axial direction. The thermodynamic conditions are $T = 0.35$ and $\mu = -2.10$.

In Figure 2.11 we show the structures obtained in equilateral triangular channels for different edge length, L. As we were expecting, the bulk symmetry is retained for the majority of the pore sizes. The triangular symmetry is only altered for pore sizes that are highly incommensurate with its bulk lattice constant, L_0, and its equilibrium cluster radius, r_0, so the pore can not accommodate

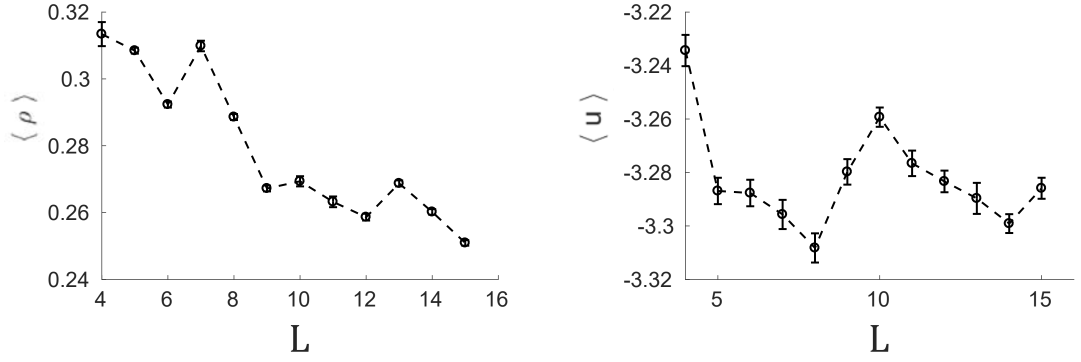

Figure 2.14: Average density,$\langle \rho \rangle$, and average energy,$\langle u \rangle$, as functions of the side length of the hexagonal pores.

an integer number of cylindrical aggregates. We notice that this behaviour is not only favoured by the matching between the fluid structure and the shape of the pore, but also by the presence of narrow wedges in the corners that act as nucleation points. We propose that the mechanism of formation of the structure starts with the assembly of straight cylindrical clusters at the corners, which facilitates the formation of additional cylindrical clusters in the centre of the pore and their ordering in a triangular lattice.

We have also observed some structural features worth discussing. In Figure 2.12, we show the evolution of the average energy and density as functions of the triangle side length. The energy minima correspond to those configurations that, given the appropriate pore size, have structural parameters (L_0 and r_0) close to the hexagonal phase parameters in bulk. For instance, the separation distance between two nearest neighbours cylinders is 6.03σ at the second minimum ($L = 11\sigma$), 6.00σ at the third ($L = 17\sigma$) and 5.99σ at the fourth ($L = 23\sigma$). These values must be compared to $L_0 = 6.20\sigma$ in the bulk phase at the same thermodynamic conditions. Another remark that gives us further evidence of the correlation between the energy minima and the possibility of accommodating the cylindrical clusters with radii and inter-distances compatible with those of the bulk phase is that the period from one minimum to the next one is around 6σ. From our results, we notice that, as a consequence of the triangular symmetry induced by confinement, the number of cylindrical clusters does not grow continuously. Instead, it follows an inverse pyramidal growth, in which the number of clusters goes from one ($5.0\sigma \leq L \leq 8.0\sigma$), to three ($9.0\sigma \leq L \leq 14.0\sigma$), to six ($15.0\sigma \leq L \leq 20.0\sigma$), to ten ($21.0\sigma \leq L \leq 24.0\sigma$). According to this inverse pyramidal growth, the radius of the cylindrical aggregates increases periodically with the pore size, with sudden drops each time that a new row of

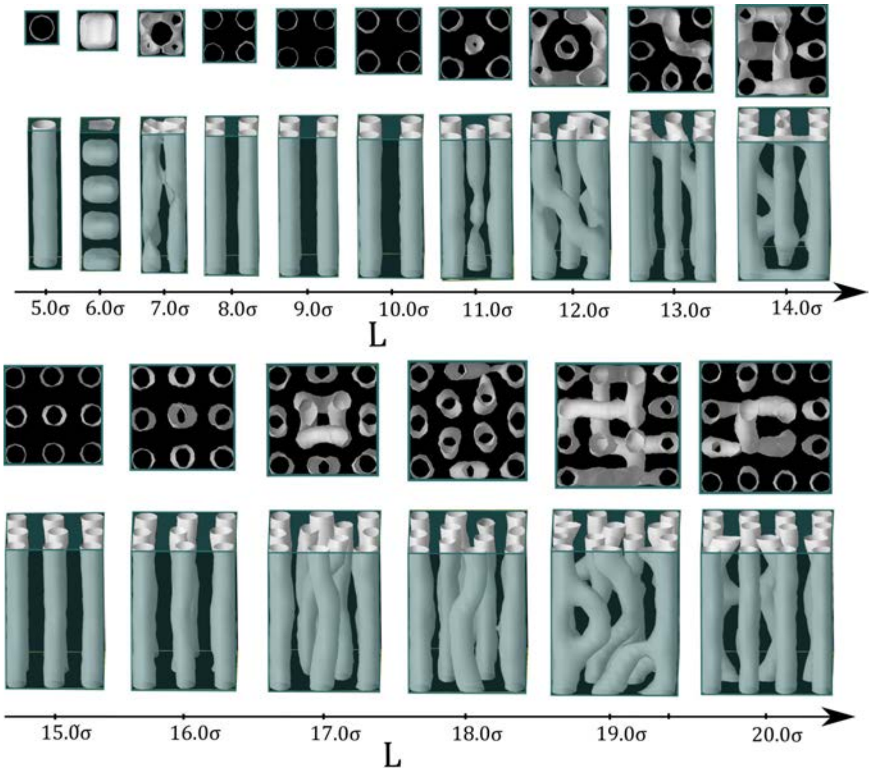

Figure 2.15: The structure of colloidal clusters confined in channels with squared cross-sections. The gray surface corresponds to an iso-density surface with $\rho_{iso} = 0.4$. Two views of the structures are depicted. Side lengths, L, between 5.0σ and 20.0σ are presented. The length of the channel is $L_z = 24\sigma$. Periodic boundary conditions are applied along the axial direction. The thermodynamic conditions are $T = 0.35$ and $\mu = -2.10$.

cylinders is formed. Furthermore, the maximum packing is achieved when a new row of cylindrical aggregates is added, whereas the energy minima appear at larger edge lengths of the triangular pore. Similar studies on triangular confinement in block copolymers have been performed with striking similarities to our findings. Both in two-dimensional [72] and three-dimensional [74, 68] systems, the main features like the inverse pyramidal growth and the periodic changes in the radius of the clusters were also found in such studies. This is further evidence of the universality of the phase behaviour of systems with competing interactions, despite the type of interactions or the chemical composition, not only in bulk but also in confinement.

Let us continue with the confinement in hexagonal channels. Since this type of confinement has the same symmetry of the hexagonal phase in bulk, we might expect that the effects on the structure of the system will be similar to those described for the triangular cross-sectioned pores. However, it turns out that the behaviour differs significantly depending on the side length, L, of

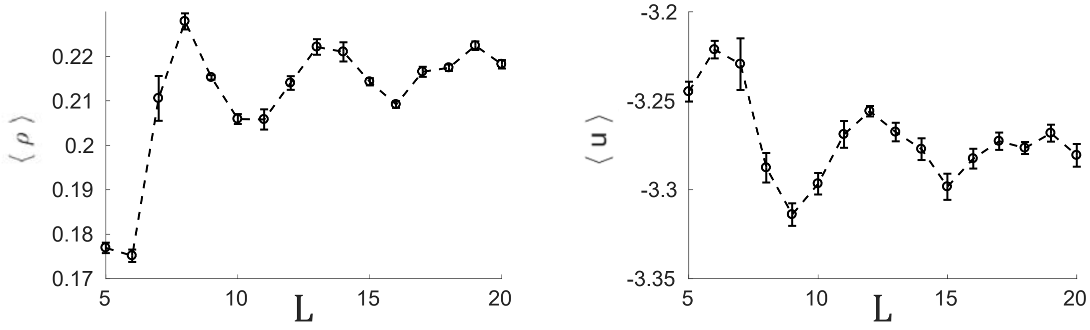

Figure 2.16: Average density,$\langle \rho \rangle$, and average energy,$\langle u \rangle$, as functions of the side length of the squared pores.

the hexagonal channel. For some pore sizes, the structure of the colloidal fluid is similar to that found in triangular pores, but, for some others, the system self-assembles into helical structures similar to those observed under cylindrical confinement in the previous section. The bulk hexagonal phase stabilizes for edge lengths within the ranges $7.0\sigma \leq L \leq 9.0\sigma$ and $13.0\sigma \leq L \leq 15.0\sigma$, as can be seen in Figure 2.13. For the rest of the edge lengths, the colloidal particles assemble into helical structures. Our first hypothesis is that, geometrically, a hexagon is not that different from a circle, which somewhat makes feasible the assembly of helical structures under confinement in hexagonal pores too. Although, unlike the case of cylindrical pores, the hexagonal channels promote competition between helical structures and straight cylindrical aggregates arranged in a hexagonal lattice, which gives us more possibilities to modulate the structure of the colloidal fluid. We note that the helical structures appear when the pore size can not fit an integer number of cylinders with values of inter-distance and cylinder radius close to those in bulk. Particularly, intertwined helices are formed for $4.0\sigma \leq L \leq 6.0\sigma$ and concentric helices for $11.0\sigma \leq L \leq 12.0\sigma$ (See Figure 2.13). Even though a hexagon has wedges as a triangle, these are wider in the hexagon, which explains why the hexagonal phase is less favoured in hexagonal than in triangular pores. Another important aspect is that the clusters formed close to the walls of the hexagonal channels are straight rather than curved cylinders.

In Figure 2.14, the results for average energy and density as functions of the edge length, L, are depicted. We identify two minima in the energy plot for $L = 8.0\sigma$ ($L_0 \approx 5.97\sigma$,$r_0 \approx 1.67\sigma$) and $L = 14.0\sigma$ ($L_0 \approx 6.08\sigma$,$r_0 \approx 1.67\sigma$) that correspond to the hexagonal phase. As we reported, in both cases, the values of the lattice constant, L_0, and radius of the clusters, r_0, are close to their counterparts in bulk. Similarly to the triangular case, local maxima in packing occur at those sizes just before the energy minima, namely, $L = 7.0\sigma$ and $L = 13.0\sigma$, which are also the sizes for which the hexagonal phase with a given number of clusters is first stabilized. The helical structures formed in hexagonal pores always exhibit higher energy than the hexagonal arrangement of straight cylinders ($L = 8.0\sigma$ and $L = 14.0\sigma$), which supports our statement that the helices only appear when the geometrical parameters of the channels are not commensurate with the equilibrium parameters of the hexagonal phase in bulk.

The last cross-section geometry that we explore is the squared one. In this case, the shape of the cross-section is completely incompatible with the symmetry of the hexagonal phase in bulk. Thus, the original hexagonal symmetry of the bulk phase is always frustrated when confined in squared channels as can be seen in Figure 2.15. Straight cylindrical aggregates are stabilized for the majority of the pore sizes. For some values of L, the system assembles into a squared array of straight cylinders. Within the range $8.0\sigma \leq L \leq 10.0\sigma$, we obtain one unit cell and for $15.0\sigma \leq L \leq 16.0\sigma$ we obtain two by two unit cells. The energy minima correspond, precisely, to square lattices as can be observed from Figure 2.16. The equilibrium geometrical parameters for $L = 9.0\sigma$ are $L_0 \approx 5.74\sigma$ and $r_0 \approx 1.51\sigma$ and for $L = 15\sigma$. Here we note that neither the lattice parameter nor the radius of the clusters is close to the values of the original hexagonal phase in bulk. This leads to some energy increases due to high repulsion experienced by the clusters that are placed closer than they would ideally be. For the largest squared pores, we notice that the cylindrical clusters in the centre tend to arrange locally in a hexagonal lattice, which results to be very distorted due to the competition with the squared lattice promoted by the channel shape.

2.3.1 Other phases under confinement

So far, in this chapter, we have been discussing the effects of confinement in channels with different geometries on the structure of the hexagonal phase. At the beginning of this study, we explored the behaviour of other phases (i.e., the cluster-crystal and lamellar phases) under cylindrical confinement, but the structures formed were not so interesting to report. However, with the knowledge we have acquired confining the system in channels with strong nucleation points (high curvature and narrow wedges), we consider that the other phases can be affected positively by these nucleation points and then form ordered structures as well. In this section, we study the morphological transitions in each type of channel when the chemical potential is varied. In Figure 2.17, we present the most relevant results obtained for $-2.50 \leq \mu \leq -1.30$. Based on the phase diagram calculated in reference [24], and the simulations we have performed in bulk, we identified the following ranges of chemical potential in which each phase is stable at $T = 0.35$:

- Cluster-crystal: $-2.60 \leq \mu \leq -2.35$
- Cylindrical:$-2.30 \leq \mu \leq -1.90$
- Lamellar:$\mu \geq -1.80$

For triangular and squared pores, we study the pore sizes that lead to lower energies in Figures 2.12, 2.16. For elliptical and hexagonal channels, since these geometries allow the formation of both helical and straight aggregates, we chose two sizes stabilizing each type of structure.

In the two top rows of Figure 2.17, we present the results for the elliptical pores. The cluster-crystal phase is frustrated in the two pore sizes considered, and only small clusters with no defined shape are formed randomly. Both the helical and straight configurations can survive over a broad range of chemical potentials ($-2.30 \leq \mu \leq -2.10$ for the helical structures and $-2.20 \leq \mu \leq -2.10$ for the straight structures), which gives us confidence on the stability and robustness of the structures. At higher chemical potentials, when the stability region of the lamellar phase is achieved, the system assembles into a layered configuration adapted to the geometry of the pores. The largest pore ($R_x = 9.0\sigma$,$R_y = 5.5\sigma$) can accommodate one layer close to the channel wall and one cylindrical cluster in the centre, whereas the smaller one ($R_x = 9.0\sigma$,$R_y = 4.5\sigma$) can only hold one layer because of the reduced space inside the pore.

In the triangular pore, (Figure 2.17, third row), similarly to the previous case, random amorphous clusters appear at low chemical potentials. The triangular array of straight cylinders survives in the same range of chemical potentials as in the elliptical pores. And, finally, the lamellar phase is composed of only one layer that now adopts a triangular shape. Nevertheless, we note that the chemical potential required to assemble the lamellar phase is substantially higher in the triangular pore in comparison to other channel geometries. We speculate that it is a consequence of triangular pore favouring the hexagonal phase due to the strong nucleation points it has at the corners.

Continuing with the discussion, we show the results for hexagonal channels in the fourth and fifth rows of Figure 2.17. The morphological changes of the phases are quite similar to those described for the elliptical and triangular channels. The only remarkable difference is that the hexagonal phase is stable for a relatively wide range of chemical potentials ($-2.30 \leq \mu \leq -2.10$) in the small pore

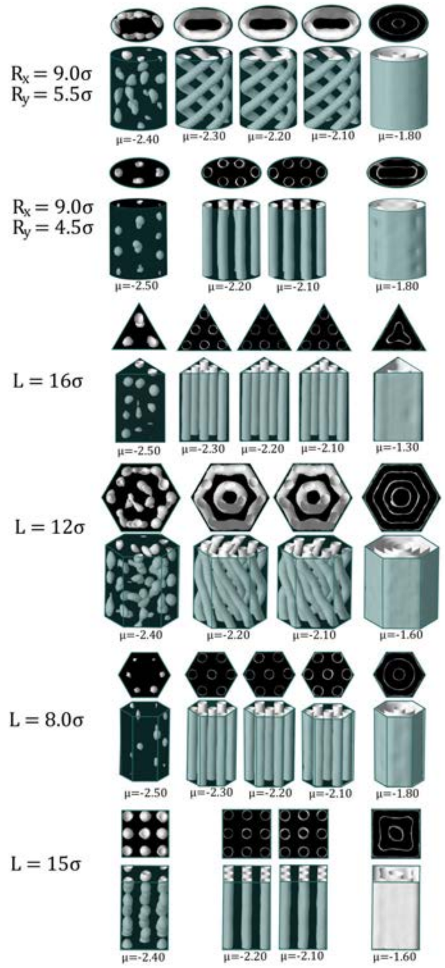

Figure 2.17: The structures of colloidal clusters confined in channels with different cross-sections when the chemical potential, μ, is varied. The temperature is fixed at $T = 0.35$. The geometrical parameters of the pores are indicated on the left. The length of the channels is $L_z = 24\sigma$. The iso-density surface is depicted in gray for a local density $\rho_{iso} = 0.4$. Periodic boundary conditions are applied along the axial direction.

($L = 8\sigma$), whereas the helical structure formed in the larger pore ($L = 12\sigma$) is more affected by changes in chemical potential.

Finally, when the colloidal fluid is confined into a squared pore (sixth row of Figure 2.17), we observe that at low chemical potentials an FCC cluster-crystal is formed. This result is expected since the FCC cluster-crystal is the most stable phase in bulk at these thermodynamic conditions and the geometry of the channel is compatible with the symmetry of such phase.

From this section, we can draw two important conclusions. First, we have shown that the stability region of the stable phases in bulk are shifted to higher chemical potentials (pressures) by confinement, depending the magnitude of such shift on the geometry of the confining channels. In particular, the shift is more pronounced when the system is confined into channels with planar edges (hexagonal, triangular and squared cross-sections). Second, the general behaviour of the cluster and lamellar phases is almost independent of the geometry of the pores, whereas the structure of the hexagonal phase is susceptible to changes in the confining geometry, which makes it the most appealing to produce structures with potential technological applications. In particular, colloidal particles confined in channels of different geometries are used to build wave-guide devices with applications in sensing [87, 88].

2.3.2 Wedged-cylindrical pores

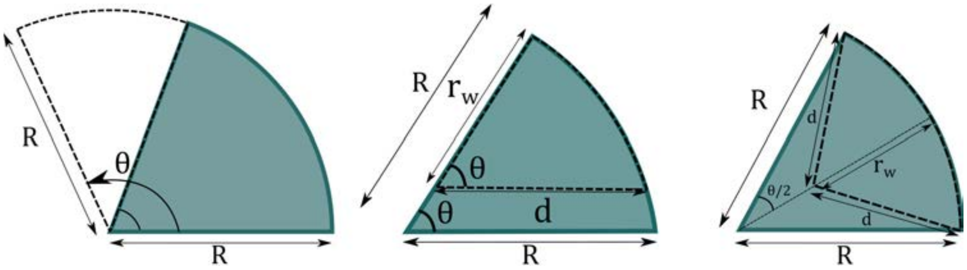

Figure 2.18: Variations of the angle and radius of the wedges inserted in the cylindrical pores. On the left panel, it is shown how the angle is varied counter clock-wise when R is maintained constant. The central panel shows how the radius of the wedge,r_w, is decreased, keeping the angle constant. On the right panel, it is shown how the radius, r_w, is decreased while the length of the wedge sides, d, are kept equal to each other (equilateral wedge). The dashed lines are examples of how the wedges change in each case.

In this chapter, we have shown that the behaviour of the bulk microphases in colloidal systems with competing interactions can be modulated by confining the system into one-dimensional channels. We have focused on the structural changes induced by confinement that leads to novel structures. Besides, we have demonstrated that confinement not only promotes the formation of new structures but helps to nucleate the bulk phases predicted by theory and simulations in colloidal systems. In particular, we showed how triangular and hexagonal channels facilitate the formation of the hexagonal phase and squared channels help to nucleate the cluster-crystal. It is an essential contribution since such microphases are still elusive in experiments with colloids in bulk [9], and we find in confinement an alternative to stabilize them when using the appropriate geometries.

With the knowledge that we have gained during this chapter, we now can be confident when saying that the bulk phase with the most interesting behaviour under confinement is the cylindrical hexagonal phase. Thus, in this section, we explore how the structure of the hexagonal phase is affected by confinement under wedged-cylindrical pores. In the previous sections, we learnt that the presence of either flat walls or narrow wedges (or regions of high curvature in elliptical pores) induce the formation of structures with straight cylindrical aggregates. To support these observations, we study the effect of flat and curved walls when both are present by the insertion of circular wedges in cylindrical pores. We propose three ways to modify the geometry of the wedges:

1. By changing the angle of the wedge that extends over the full radius of the circular cross-section.
2. By reducing one side of the wedge while keeping the angle constant.
3. By reducing the radius of the wedge while keeping the two planar sides equal to each other and the arc length constant (equilateral wedge).

In the two latter cases, the wedges are no longer circular sectors. Schemes of the three considered wedges are depicted in Figure 2.18. We choose cylindrical pores with $R = 8.0\sigma$, where intertwined helical structures surround a central cylindrical cluster, and $R = 9.5\sigma$, where concentric single helices are formed, to add the three types of wedges mentioned above. Let us start the discussion with the pore with $R = 8.0\sigma$, whose results are presented in Figure 2.19. Recalling our results from the first part of this chapter, we know that although the size of this pore is large enough to host seven cylindrical aggregates arranged in a hexagonal lattice (one central cluster surrounded by six more placed close to the pore wall), the structure of the fluid is altered by the cylindrical confinement forming the helical structure shown in Figure 2.19a. This helical structure is no longer stable when a sufficiently large wedge is inserted in the cylindrical pore. If the size and shape of the wedge are chosen appropriately, the structure of the hexagonal cylindrical in bulk can be recovered.

For the first type of wedges (Figure 2.19b), we obtained straight cylindrical clusters for angles, θ, which are integer multiples of $\pi/3$. This angle corresponds to the arc length that is occupied by one cylindrical cluster of the six distributed at the perimeter of the pore. For integer multiples of $\pi/3$, several straight cylindrical aggregates can be stabilized along the perimeter of the pore, keeping a separation between them similar to that of the bulk phase. As for the radius of the clusters, r_0, its value is also similar to that in the bulk phase. Usually, systems exhibiting a configuration similar to the bulk phase have lower average energies as can be observed in the top panel of Figure 2.20. For the rest of the angles, cylindrical clusters are deformed.

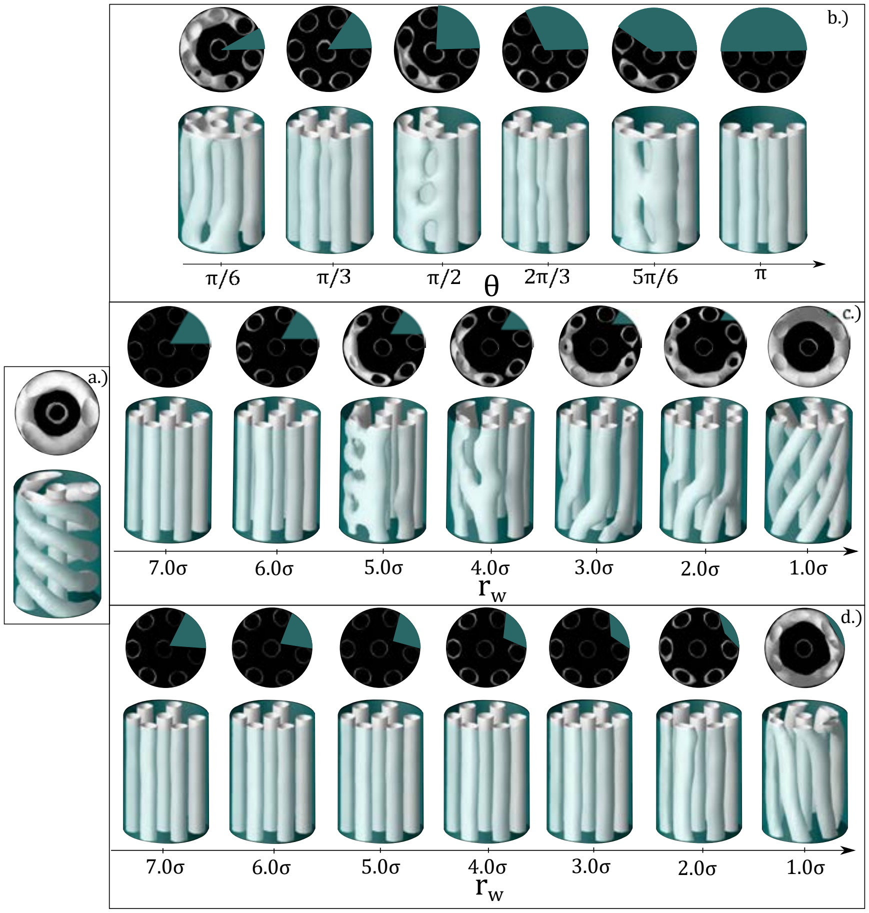

Figure 2.19: **a.)** Original helical structure formed in a cylinder of radius $R = 8.0\sigma$. **b.)** Set of structures obtained varying the angle of the wedge, θ, from $\pi/6$ to π. **c.)** Set of structures obtained varying the radius of the wedge, r_w, between 7.0σ and 1.0σ while keeping the angle constant at $\theta = \pi/3$. **d.)** Set of structures obtained varying r_w of an equilateral wedge between 7.0σ and 1.0σ. The iso-density surface is depicted for the local density $\rho_{iso} = 0.4$. Two views of each configuration are presented. The length of the channel is $L_z = 24.0\sigma$. Periodic boundary conditions along the axial direction are used. The thermodynamic conditions are $T = 0.35$ and $\mu = -2.10$.

For the second type of wedges, we observe in Figure 2.19c that, as long as the arc length is comparable to that of the wedge with angle $\pi/3$, the colloidal fluid assembles into straight cylindrical clusters arranged in a hexagonal lattice despite the smaller radius of the wedge. Once the arc length is considerably smaller, i.e. close to the value corresponding to $\pi/6$, the straight cylindrical clusters start to deform. Interestingly, we note that for a tiny wedge of $r_w = 1.0\sigma$, helical structures are stabilized again, but this time with a pitch much larger than the original structure in the absence of obstacles inside the pore. Based on the average energies reported in the central panel of Figure 2.20, the configurations with straight cylindrical aggregates are the most favoured energetically.

We want to emphasize the importance of choosing a wedge that covers the appropriate arc length

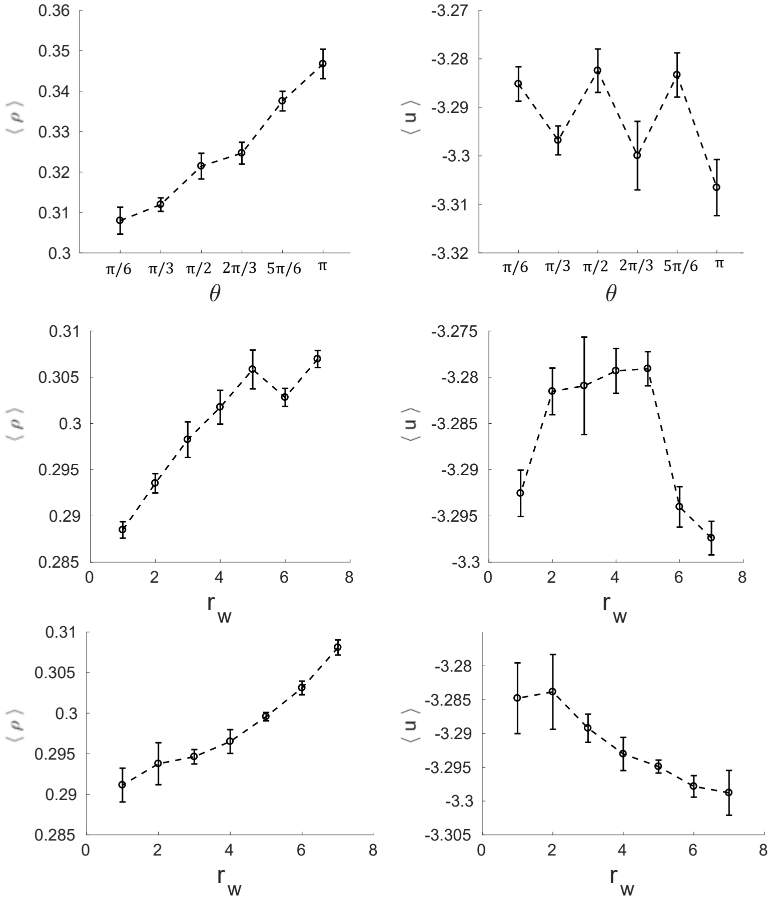

Figure 2.20: Average density,$\langle\rho\rangle$, (left column) and average energy, $\langle u\rangle$, (right column), as functions of the wedge size. The top panel corresponds to the first type of wedges (varying angle θ). The central panel corresponds to the second type of wedge (asymmetric wedge, varying r_w while θ is kept constant). The bottom panel corresponds to the third type of wedge (equilateral wedge, reducing r_w while the planar edges of the wedge remain equal to each other). The radius of the wedged-cylinder is $R = 8.0\sigma$. These results correspond to the structures presented in 2.19.

of the confining cylinder. This is further evidenced with the results obtained in the third type of wedges, whose radius is shortened while keeping the arc length constant (See Figure 2.19d). The colloidal fluid adopts, for almost all the studied radii, a configuration composed of straight cylinders. In the bottom panel of Figure 2.20, we observe that the average energy monotonically decreases up to $r_w = 7.0\sigma$ when an almost perfect hexagonal phase is formed.

With these results, we can point out one interesting observation related to the mechanism of formation of the hexagonal array of straight cylindrical clusters. The presence of wedges creates two important nucleation sites at both sides of the wedge, precisely at the joints between the confining cylinder and the wedge. Thus, two straight cylindrical aggregates grow at each side of the wedge,

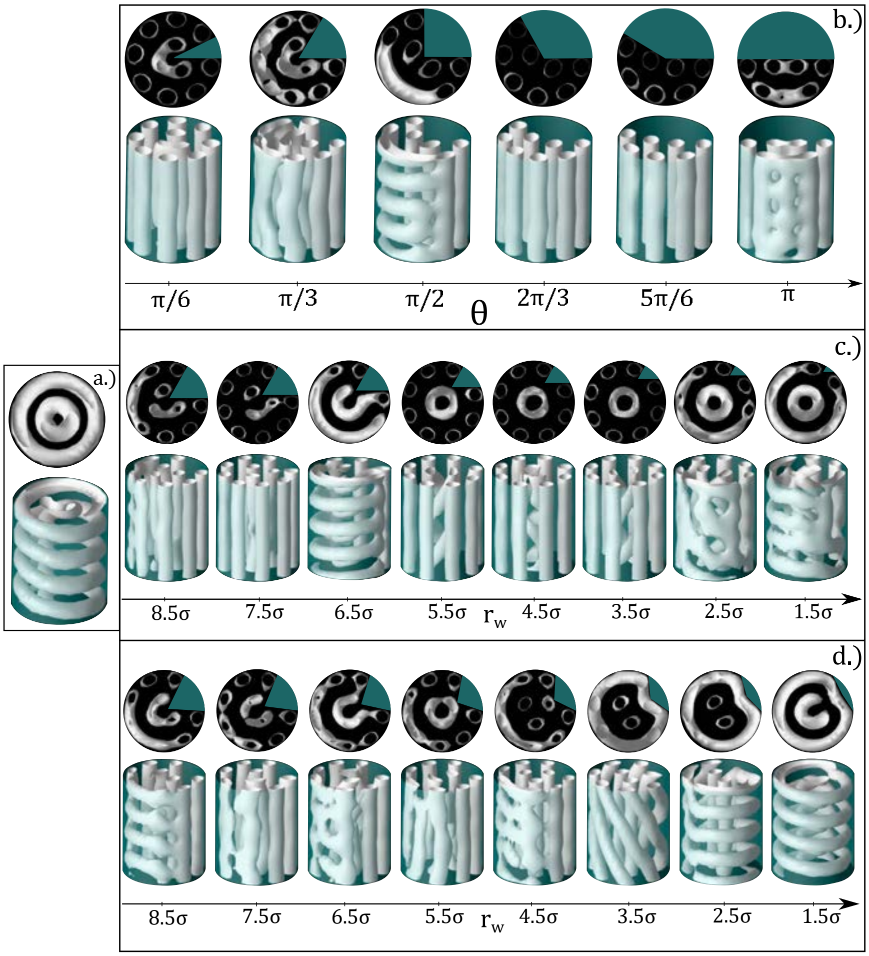

Figure 2.21: **a.)** Original helical structure formed in a cylinder of radius $R = 9.5\sigma$. **b.)** Set of structures obtained varying the angle of the wedge, θ, from $\pi/6$ to π. **c.)** Set of structures obtained varying the radius of the wedge, r_w, between 8.5σ and 1.5σ while keeping the angle constant at $\theta = \pi/3$. **d.)** Set of structures obtained varying r_w of an equilateral wedge between 8.5σ and 1.5σ. The iso-density surface is depicted for the local density $\rho_{iso} = 0.4$. Two views of each configuration are presented. The length of the channel is $L_z = 24.0\sigma$. Periodic boundary conditions along the axial direction are used. The thermodynamic conditions are $T = 0.35$ and $\mu = -2.10$.

and then such aggregates promote the formation of the rest of the hexagonal array of cylindrical clusters. The size of the wedge also defines the separation distance between those two initially formed clusters, which will affect the final structure.

As a general comment on the average density as a function of either the angle, θ, of the wedge or the radius, r_w, the behaviour is almost monotonic with an increasing tendency in all cases. This is simply reflecting that as the available volume for the colloidal particles decreases, the average density increases.

We perform the same study for a larger confining cylinder of radius, $R = 9.5\sigma$, case in which

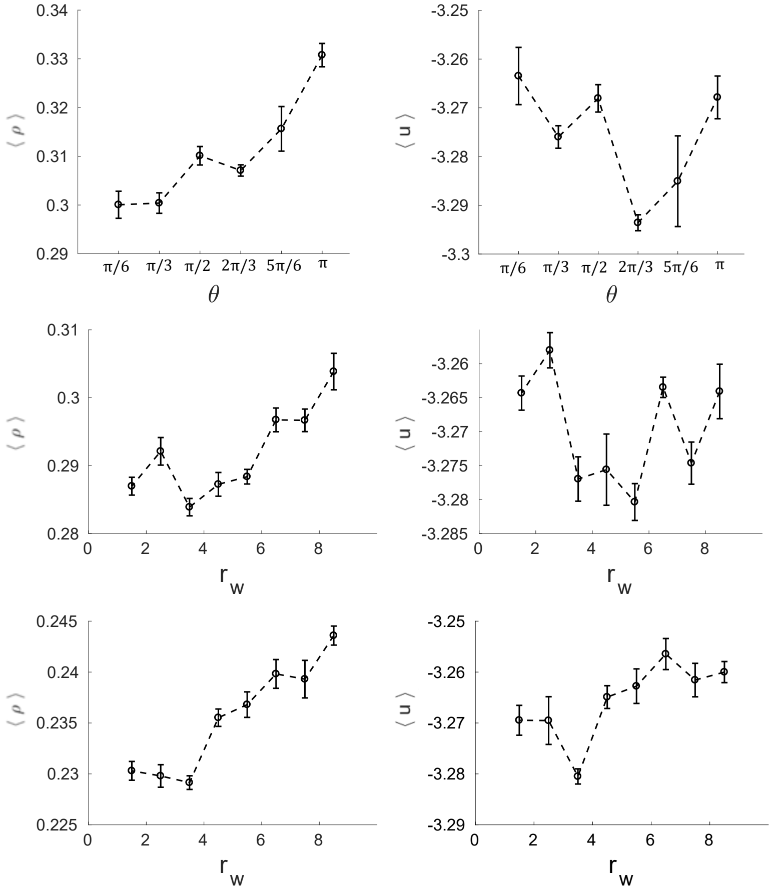

Figure 2.22: Average density,$\langle\rho\rangle$, (left column) and average energy, $\langle u\rangle$, (right column), as functions of the wedge size. The top panel corresponds to the first type of wedges (varying angle θ). The central panel corresponds to the second type of wedge (asymmetric wedge, varying r_w while θ is kept constant).The bottom panel corresponds to the third type of wedge (equilateral wedge, reducing r_w while the planar edges of the wedge remain equal to each other). The radius of the wedged-cylinder is $R = 9.5\sigma$. These results correspond to the structures presented in 2.21.

the non-wedged cylindrical pore led to the formation of two concentric helices (See Figure 2.21a). This confining cylinder has a perimeter that allows accommodating eight cylindrical clusters. This arrangement is obtained for the first type of wedge at an angle of $\theta = \pi/6$ (See the first configuration of Figure 2.21b). However, at the centre of the pore, there is a distorted cluster that comes from what would be three straight cylindrical aggregates, but due to the lack of space have merged together. This distortion makes the energy to increase . From the average energy plots presented in Figure 2.22(top panel), we can observe that the structure for $\theta = 2\pi/3$ is more energetically favourable than the structure for $\theta = \pi/6$ since the first one promotes the assembly of only straight cylindrical clusters with no defects.

For the second type of wedges (See Figure 2.21c), eight straight cylindrical clusters along the perimeter of the pore are formed for $r_w = 5.5\sigma$, 4.5σ and 3.5σ. Precisely, the average energies corresponding to such values of r_w are the lowest (See Figure 2.22 central panel). Besides, for such cases, helical structures are formed at the centre of the pore.

At this point, we notice that similarly to the case for $R = 8.0\sigma$, the arc length of the confining pore covered by the wedge is still significant to the formation of straight cylindrical clusters. If the arc length covered by the wedge is not optimal, the structure of the fluid inside the pore tends to adopt distorted configurations. In such cases, the system tries to find alternative configurations such as ladder-like structures (See Figure 2.21c, $r_w = 6.5\sigma$ and Figure 2.21d, $r_w = 8.5\sigma$) and distorted helical structures especially when the wedges are small (See Figure 2.21d for $r_w = 3.5\sigma$, 2.5σ, 1.5σ). It is interesting to note that the presence of wedges influences the whole structure of the colloidal fluid, including the structure formed in the central region of the pore. In the pristine cylinder, a single helix is formed at the centre of the pore. When wedges are inserted in the pore, such single helix can be converted into two helices (See, for example, Figure 2.21c for $1.5\sigma \leq r_w \leq 5.5\sigma$) , two or three straight cylindrical clusters(See, for example, Figure 2.21d for $2.5\sigma \leq r_w \leq 4.5\sigma$) or some more irregular shaped clusters.

As a general comment on the behaviour of the average density as a function of the size of the wedge (See Figure 2.22, left column), we observe an increasing tendency as the size of the wedge increases. Also, the local maxima correspond to distorted configurations in all cases.

2.4 Summary and conclusions

We have demonstrated that the structure of the hexagonal cylindrical phase formed in colloidal systems with competing interactions can be easily modified by confinement in one-dimensional pores.

In section 2.2, we observed that cylindrical confinement induces the formation of helical structures such as intertwined multiple helical structures and concentric helices. From our results, we learnt that the pitch and radius of the helical structures could be modulated by adjusting the diameter of the confining pore. Regarding the handedness of the helical structures, we observed that the probability of formation of clockwise and anti-clockwise helices is approximately equal. Besides, we found that, for certain geometrical parameters of the confining pore, different helical structures can be obtained with virtually the same thermodynamic properties.

We also investigated the dependence of the helices pitch with the length of the pore. We found that there is an optimum pitch that guarantees the minimum internal energy. The helical structures obtained in this chapter behave like elastic springs. We took advantage of this behaviour to estimate the optimal pitch of the single and double helices. Finally, we studied the effect boundary conditions when the cylindrical pores were closed by planar walls at the ends. We showed that inside closed cylinders, and depending on the length and radius of the pore, the system assembles into either disk-like clusters or toroidal clusters along the axial direction.

Although there have been similar studies of different colloidal systems under cylindrical confinement, we want to stress that the obtained structures in the system we have studied in this chapter are significantly different from helical structures previously reported. In particular, studies performed on systems composed of particles interacting via hard or soft repulsive potentials, such as hard spheres [89] or Yukawa [90] potentials, revealed that, under cylindrical confinement, helical structures assemble but under conditions of high pressure and very tight confinement, where the width of the confining pore is of the order of a few molecular diameters. Instead, the helical structures we report in this chapter are obtained at low pressures and for much wider pores.

We are convinced that the formation of helical structures can be realized in any system characterized by competing interactions when confined in a cylindrical pore. Examples of this kind of systems are mixtures of surfactants, lipids in water or block copolymers. In particular, we found that the behaviour of the hexagonal phase in cylindrical pores is very similar for polymeric and colloidal systems characterized by competing interactions. Thus, the universality on the phase diagram topology of systems with competing interactions[17] not only applies in bulk but also under confinement. We expect that many results obtained so far for copolymers are also applicable to colloidal systems. Thus, the knowledge already obtained for copolymers[76, 68, 77] can be used as a guide for new studies of colloidal systems with competing interactions. And the other way around, the results of our simulations might be also used to guide experiment with copolymers.

In section 2.3, we explored the behaviour of the system, mainly the hexagonal cylindrical phase, under confinement in one-dimensional channels with different cross-sections. We have found the conditions, both geometrical and thermodynamic, that promote different assemblies of the colloidal clusters in each studied geometry. One of the most important conclusions from this section is that pores with regions of high curvature (elliptical) or with narrow edges (triangular and squared) can be used to stabilize straight cylindrical clusters. Such regions act as nucleation sites that favour the assembly of straight cylindrical clusters. On the other hand, the symmetry of the cylindrical phase, which in bulk is hexagonal, can be modified at will by confinement in the appropriate geometry.

For instance, narrow channels with squared cross-sections can stabilize a square lattice of cylindrical aggregates.

Similar studies for two-dimensional colloidal fluids with competing interactions have been performed [53, 55, 54, 29, 91, 92, 60, 62]. The models used in computational simulations were either lattice models [60, 62] or continuous models[53]. Besides simulations, these systems have been studied utilizing the density functional theory[55, 54, 29, 91, 92]. Comparing our results to those just mentioned in the previous lines, we have to stress that the phase diagram of a three-dimensional system is richer than that of its two-dimensional version. Specifically, the hexagonal cylindrical phase and the double gyroid phase do not have analogues in two-dimensional systems. As we are focused on the hexagonal cylindrical phase, we are advancing the knowledge we currently have on this kind of systems. However, there are some features that the two and three-dimensional systems share. The commensurability of the period of the ordered phases in bulk with the channel geometries and sizes is key to the equilibration of the structure of the confined colloidal fluid both in two and three-dimensional systems.

Our simulation results are supported by experiments and theoretical calculations in block copolymers, which find similar structures as those presented in this chapter for the same confining geometries [68, 74, 69]. With this experimental validation, the results obtained for geometries that have not been realized in experiments yet, such as wedged-cylinders, are expected to be also reliable. Particularly, the insertion of wedges in circular pores is a versatile way to modulate at will the structure of the confined fluid. The use of wedges to modify the structure of confined block copolymers has been considered in previous works, although in such cases it was used to transform concentric lamellae into spiral ones [93, 94].

We think that the investigation of ordered structures in simple confined geometries can be easier than in bulk since the number of possible metastable states is likely reduced in tight confinement conditions. We hope that the results from computer simulations presented in this chapter can be an inspiration to design new experimental studies of colloidal systems with competing interactions.

Chapter 3

Confinement in spherical and ellipsoidal shells

We will discuss how the structure of the hexagonal phase is affected when confined in spherical and ellipsoidal shells. We use MC simulations in the grand canonical ensemble. We want to investigate how the cylindrical clusters, which are straight in bulk, will be arranged in a curved quasi-two-dimensional space. Thus, we used thin shells to realize such systems. The thickness of the shells was as small as possible to allow the nucleation of one layer of cylindrical clusters.

The main conclusion of this chapter is that the structures we obtain are geometrical solutions of the problem of the longest rope filling the surface of a sphere [95]. Furthermore, the self-assembly of block copolymers has been studied on the surface of a sphere, obtaining also solutions of the problem above-mentioned [71]. These solutions are not only observed in systems with competing interactions in equilibrium but also in Turing pattern-forming systems on spheres [96].

3.1 Model and simulation details

The colloidal particles interact via the SWL potential in the Equation 2.1 with the same parameters as in the previous chapter. Let us start by describing the confinement into spherical shells with hard walls. The system is finite and quasi two-dimensional since we are focused on narrow shells. To construct such shells, we define an inner sphere of radius, R_{inn}, and an outer sphere of radius, R_{out}. Both spheres are concentric. The region between the two spheres defines the shell in which the particles are allowed to move. Any region outside the shell is prohibited for the particles. The shell region is,

$$S = \{x, y, z \mid R_{inn}^2 \leq x^2 + y^2 + z^2 \leq R_{out}^2\} \tag{3.1}$$

Where x, y and z are the Cartesian's coordinates. Based on the shell region, S, we can define the external potential,

$$\mathcal{V}(\mathbf{r}_i) = \begin{cases} 0, & \mathbf{r}_i \in S \\ \infty, & \mathbf{r}_i \notin S \end{cases} \tag{3.2}$$

Here $\mathbf{r}_i$ denotes the position of particle i.

Similarly, we can define an ellipsoidal shell, composed of two concentric ellipsoids as follows,

$$\begin{gathered} E = \{x, y, z \mid B_{inn}^2 C_{inn}^2 x^2 + A_{inn}^2 C_{inn}^2 y^2 + A_{inn}^2 B_{inn}^2 z^2 \geq A_{inn}^2 B_{inn}^2 C_{inn}^2, \\ B_{out}^2 C_{out}^2 x^2 + A_{out}^2 C_{out}^2 y^2 + A_{out}^2 B_{out}^2 z^2 \leq A_{out}^2 B_{out}^2 C_{out}^2\} \end{gathered} \tag{3.3}$$

Where A, B and C are the principal semi-axes of the ellipsoid along x, y and z respectively. The subscripts denote the inner and outer ellipsoids. The external potential for an ellipsoidal shell can be defined equivalently to equation 3.2, but changing S for E. The total energy of the system is thus given by

$$U_{tot} = \sum_{i=1}^{N-1} \sum_{j>i}^{N} u_{SALR}(r_{ij}) + \sum_{i=1}^{N} \mathcal{V}(r_i), \tag{3.4}$$

N is the total number of colloidal particles. $u_{SALR}(r_{ij})$ is given by equation 2.1 as in the previous chapter. The parameters and their values are given in section 2.1. Examples of the simulated systems are depicted in Figure 3.1.

The structure of the colloidal fluid confined in spherical and ellipsoidal shells is investigated by Monte Carlo simulations in the grand canonical ensemble (μ,V,T). All the thermodynamic parameters (chemical potential, temperature, internal energy, density, and distance) are reported using σ and ϵ as units of distance and energy, respectively. The simulated systems contain between 1000 and 2200 particles. We first carried out an equilibration run whose length depends on the system size. The production run, where averages are taken, consists of 2×10^{10} MC steps, from which 2×10^5 independent configurations were taken for calculating the local density, following the process

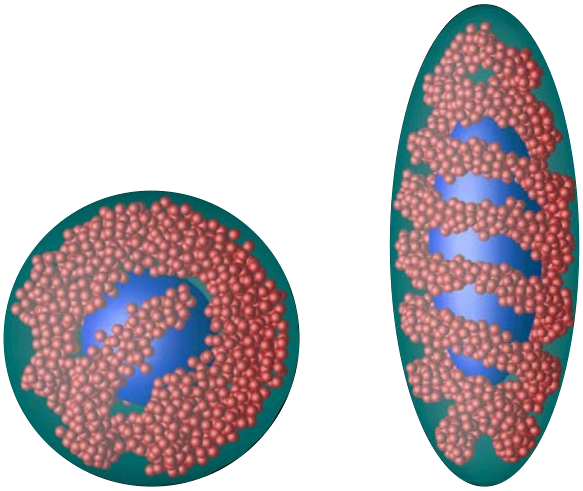

Figure 3.1: The colloidal fluid confined in spherical (left panel) and ellipsoidal (right panel) shells.

described in section 2.1 (See Figure 2.1). A Monte Carlo step is defined as a trial move that may be a displacement, addition, or deletion of a particle. We set the displacement attempt probability at 95% and the remaining 5% to the particle exchange attempt. Simulations were performed at temperature $T = 0.35$ and at values of chemical potential in the range $-2.35 \leq \mu \leq -2.10$. In these thermodynamic conditions the hexagonal cylindrical phase is stable in bulk. In a preliminary study, we found that the width, W, of the shells must be around 5σ because for lower values the cylindrical clusters are unstable, and for larger values more than one layer of cylindrical clusters can be formed.

3.2 Discussion and results

We run simulations in spherical shells keeping $W = 5\sigma$ constant while we vary the external radius so that, $R_{inn} = R_{out} - W$. We performed a set of preliminary simulations and found that the most interesting behaviour occurs for $R_{out} \geq 10\sigma$. Especially, the radii $R_{out} = 11\sigma$ and $R_{out} = 12.5\sigma$ offer the more interesting structures and thus we analyse those system sizes in detail.

In Figure 3.2, the results for a spherical shell with $R_{out} = 11\sigma$ are presented. The first interesting thing we must note is that the average energies are quite similar (virtually equal for some cases, $\mu = -2.130$ and -2.150) for all considered chemical potentials, even though the structures are different in each case. On the other hand, although the average number density does not vary too much with the chemical potential, it does change to a greater extent compared to the average energy, showing a slowly increasing behaviour as the chemical potential increases. At $\mu = -2.130$,

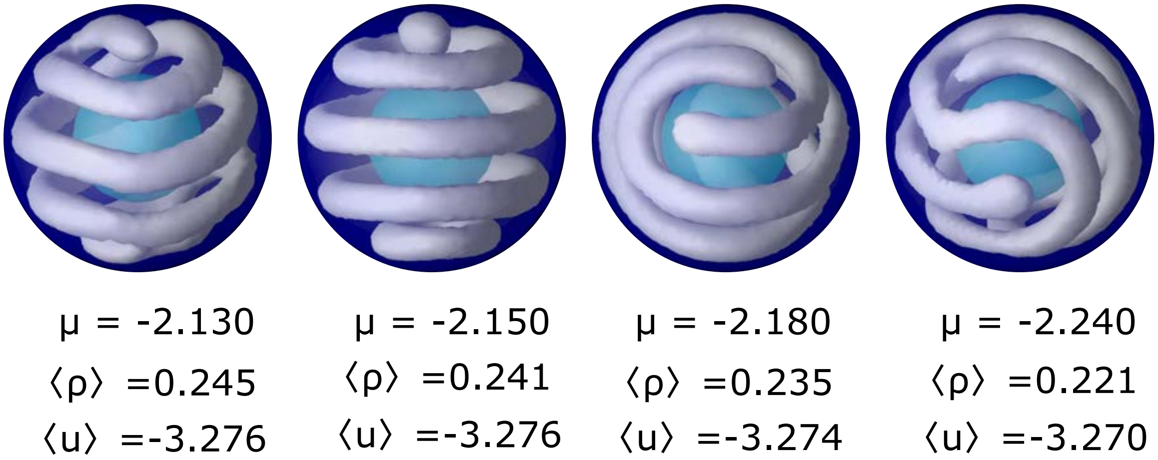

Figure 3.2: Structures obtained by confining a SWL colloidal fluid into a spherical shell with $R_{out} = 11\sigma$ and $W = 5\sigma$. Iso-density surfaces are presented in white, with $\rho_{iso} = 0.40$, and the outer and inner spheres are represented in blue and cyan respectively. The temperature is $T = 0.35$ and the chemical potential is shown in the figure. The average number density and energy are also presented for each structure.

the colloidal fluid self-assembles into one cylindrical cluster whose ends are placed at opposite poles of the sphere. The shape resembles a single helix. At $\mu = -2.150$, the colloidal fluid forms a structure made of one spherical cluster at one pole, and then four tori up to reach the opposite pole. At $\mu = -2.180$, we obtain a structure composed of one cylindrical cluster whose ends are placed at the same pole. Starting from one of the ends, the cylindrical cluster goes over the shell describing a spiral until it reaches the opposite pole where, with a turn, goes back over the shell describing a spiral and finally reaching the starting pole and placing itself by the side of the initial end. In other words, the structure resembles a double-helix whose ends are merged at the opposite pole. Finally, when $\mu = -2.240$, the structure is made of one cylindrical cluster whose ends are separated by one segment that results from the folds and turns along its path (see Figure 3.2).

In Figure 3.3, we show the results for a spherical shell with $R_{out} = 12.5\sigma$. We obtain more structures than those in the previously analysed shell since, being this one larger, it allows more freedom for the colloidal fluid to self-assemble into more different ways. At $\mu = -2.170$, the system self-assembles into one cylindrical cluster whose ends are separated by two turns of the cluster. Similarly, at $\mu = -2.180$, the ends of the cylindrical cluster are separated by one turn. As in the case of the shell with $R_{out} = 11.0\sigma$, the system can self-assemble into a structure made of a spherical cluster placed at one pole and then a succession of five tori that cover the sphere surface up to the opposite pole. We also obtained double helix-like and single helix-like structures, both at the same

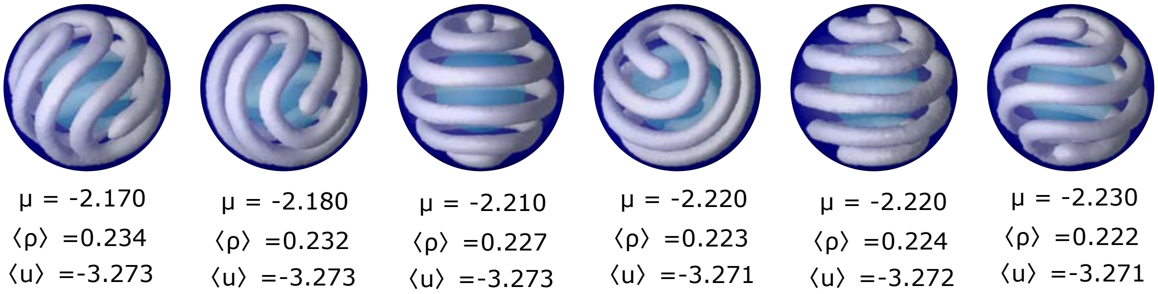

μ = -2.170 ⟨ρ⟩ =0.234 ⟨u⟩ =-3.273

μ = -2.180 ⟨ρ⟩ =0.232 ⟨u⟩ =-3.273

μ = -2.210 ⟨ρ⟩ =0.227 ⟨u⟩ =-3.273

μ = -2.220 ⟨ρ⟩ =0.223 ⟨u⟩ =-3.271

μ = -2.220 ⟨ρ⟩ =0.224 ⟨u⟩ =-3.272

μ = -2.230 ⟨ρ⟩ =0.222 ⟨u⟩ =-3.271

Figure 3.3: Structures obtained by confining a SWL colloidal fluid into a spherical shell with $R_{out} = 12.5\sigma$ and $W = 5\sigma$. Iso-density surfaces are presented in white, with $\rho_{iso} = 0.40$, and the outer and inner spheres are represented in blue and cyan respectively. The temperature is $T = 0.35$ and the chemical potential is shown in the figure. The average number density and energy are also presented for each structure.

chemical potential, $\mu = -2.220$. This case is interesting since different structures can be obtained at exactly the same thermodynamic conditions, as it happens when the system is confined in cylindrical pores (See Figure 2.7c). Finally, at $\mu = -2.230$, we obtain a cylindrical cluster whose ends are placed at opposite poles and separated by three turns of the cluster.

In both spherical shells, $R_{out} = 11\sigma$ and 12.5σ, the average energies and densities are quite close between different structures, indicating that the different solutions that the system finds are somewhat connected with optimal configurations that guarantee the minimum energy with the same amount of material (particles), given the radius of the cluster and the separation between the turns of the coiled cluster. In the case of colloidal systems with competing interactions, the radius of the cylindrical cluster is determined by the attractive range of the interactions, and the separation between folds by the repulsive range. Interestingly, the solutions that we find are compatible to those of the problem of the longest rope that fills the surface of a sphere, when the rope thickness and the sphere radius are specified [95].

Furthermore, based on our results, we speculate that small fluctuations in the number of particles might induce transitions from one configuration to another. To support this hypothesis, we run a very long MC simulation at $\mu = -2.210$ and $T = 0.35$, for a spherical shell with $R_{out} = 12.5\sigma$ to check if the system can adopt different structures at equilibrium. Figure 3.4 shows the results of an MC simulation of 10^{11} steps. From the instantaneous energy and density plots we can observe that the system is indeed at equilibrium, and that the fluctuations are within 1% of the mean values. This supports our hypothesis that the structural transitions are driven by quite small fluctuations in the density. On the right part of Figure 3.4, we show 4 out of 6 structures presented in Figure 3.3, but during the same MC run. We believe that in a longer run we could find all the 6 structures.

Thus, we conclude that all the structures that we obtained are thermodynamically and geometrically equivalent.

Now, we will continue by discussing the effects of confinement in ellipsoidal shells on the structure of the colloidal fluid (see Figure 3.1, right panel). To perform a systematic study, we propose a transformation of the spherical shell that gradually turns it into an ellipsoidal one.

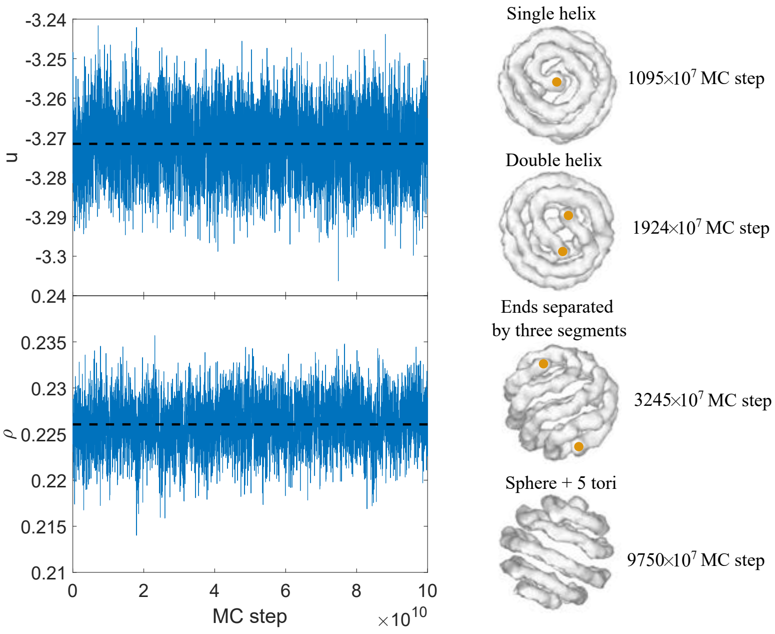

Figure 3.4: A long MC run that shows how the system fluctuates between different ordered configurations. The instantaneous energy, u, and density, ρ, are shown on the left side. The black dashed lines are the average values. The density and energy fluctuations are within 1% of the mean value, meaning that the system is probably at equilibrium. On the right side, instantaneous iso-density surfaces of different structures are presented. Orange dots are placed at the ends of the cylindrical clusters as guides to the eye. The surfaces are generated by the visualisation software OVITO [97], using the Gaussian density method with a resolution of 40, a radius scaling of 100% and an iso-value of 0.7.

We start from the volume of the ellipsoidal shell:

$$V_{Eshell} = \frac{4\pi}{3} A_{out} B_{out} C_{out} - \frac{4\pi}{3} A_{inn} B_{inn} C_{inn} \tag{3.5}$$

To keep the width of the shell equal to 5σ, we define,

$$\begin{aligned} A_{inn} &= A_{out} - 5\sigma \\ B_{inn} &= B_{out} - 5\sigma \\ C_{inn} &= C_{out} - 5\sigma \end{aligned} \tag{3.6}$$

We replace eq. 3.6 in eq. 3.5 to get the following expression,

$$V_{Eshell} = \frac{4\pi}{3}[5(A_{out}B_{out} + A_{out}C_{out} + B_{out}C_{out}) - 25(A_{out} + B_{out} + C_{out}) + 125] \tag{3.7}$$

Now we introduce the transformation,

$$\begin{aligned} C_{out} &= A_{out} \\ B_{out} &= \alpha A_{out} \end{aligned} \tag{3.8}$$

With this, the ellipsoidal shell maintains a spherical cross section in the plane xz, while the transformation occurs along the y axis. Substituting eq. 3.8 in eq. 3.7, we obtain,

$$V_{Eshell} = \frac{4\pi}{3}[5(2\alpha + 1)A_{out}^2 - 25(\alpha + 2)A_{out} + 125] \tag{3.9}$$

The final step is to calculate the volume of the spherical shell we want to keep constant, we substitute it in eq. 3.9 and then solve for A_{out} for different values of α. If $\alpha = 1.0$ we have the spherical shell case. For $\alpha < 1.0$ we shorten the sphere in the y axis converting it into an oblate. For $\alpha > 1.0$, we elongate the sphere in the y direction converting it into a prolate.

In Figure 3.5 we present the results for the system confined in ellipsoidal shells with identical volume to the spherical shell at different values of α and at the same thermodynamic conditions ($\mu = -2.180$, $T = 0.35$). The pristine structure obtained in the spherical shell is a cylindrical cluster whose ends are separated by one turn of the cluster. Let us discuss first the structural changes induced by the oblate ellipsoidal shells. Curiously, in any of the oblate ellipsoidal shells the ends of the cluster are separated by one segment as in the original one. Instead, structures in which the ends of the cylindrical cluster are separated by two ($\alpha = 0.8$ and 0.5) and three turns ($\alpha = 0.9$ and 0.6) are observed. Additionally, for $\alpha = 0.7$ the cluster forms a double-helix that merges at the opposite pole, and for $\alpha = 0.4$ five tori are formed along the y direction in which the transformation is applied.

In the prolate ellipsoidal shells, we observe that helical structures are highly favoured, being present for all values of α. This behaviour is somewhat expected since as the y-axis of the ellipsoidal shells is elongated, it becomes more similar to a cylindrical shell, geometry that strongly favours the formation of helical structures as we discussed in Section 2.2. At $\alpha = 1.5$, a single-helix is formed, but is now somewhat tilted. The ends of the helix are not placed at the highest curvature regions

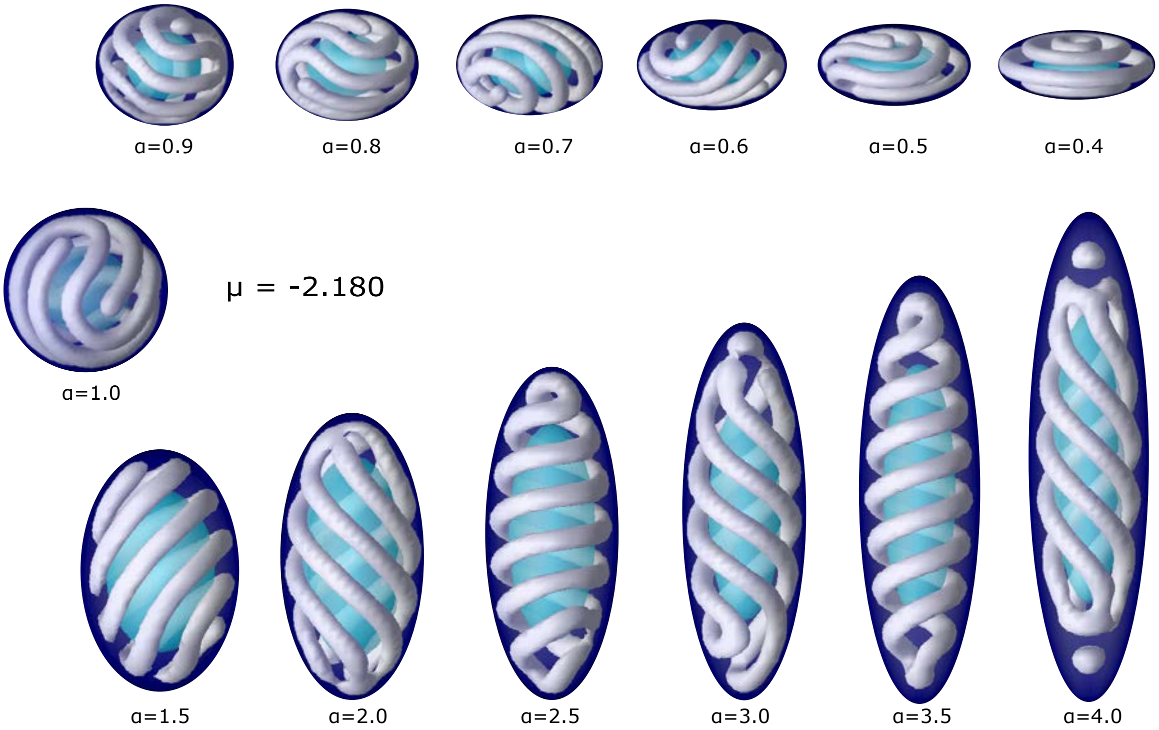

Figure 3.5: Set of structures obtained by confining a SWL colloidal fluid into ellipsoidal shells of the same volume. The temperature is $T = 0.35$ and the chemical potential $\mu = -2.180$. Starting from a spherical shell, we gradually transform the spherical shell into prolate ($\alpha > 1.0$) and oblate ($\alpha < 1.0$) ellipsoidal shells.

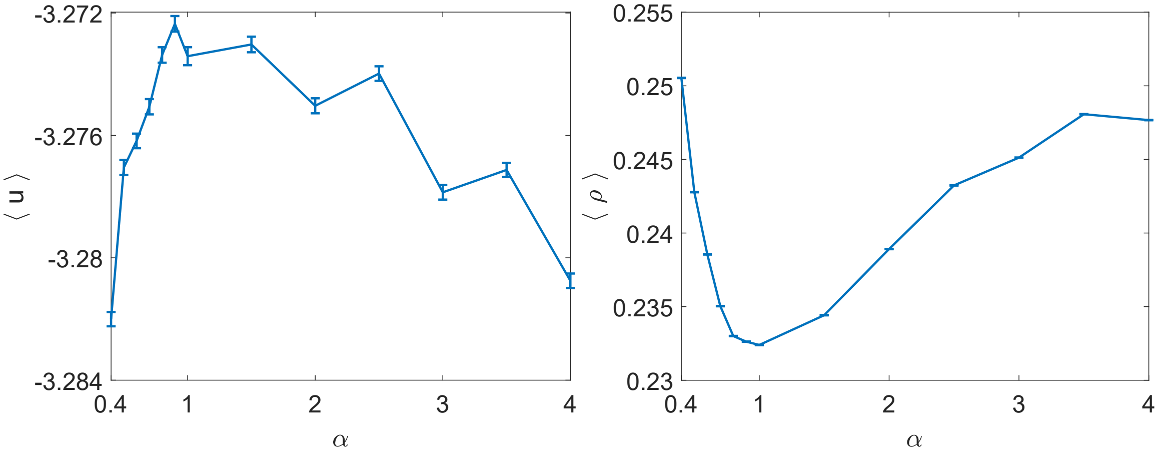

Figure 3.6: Average energy, $\langle u\rangle$, and density, $\langle \rho\rangle$, as functions of α.

(poles of the ellipsoid) of the shell because in such a case the first turn does not have enough room to form without experiencing high repulsion. Regions with less curvature provide more room for the first turn and then avoid high repulsion. At $\alpha = 2.0$, a penta-helix whose ends merge at the poles in the larger axis is formed. At $\alpha = 2.5$ and 3.5, the colloidal fluid assembles into a double-helix.

For $\alpha = 3.0$ the helical structure has some defects at the regions of high curvature. We speculate that these defects might be related to the competition of different stable structures driven by small fluctuations in the number of particles as we discussed in the case of the spherical shell (see Figure 3.4). Finally, at $\alpha = 4.0$, we obtain a tetra-helix whose ends merge into tori at the ends of the surface of the inner ellipsoid accompanied by two spherical clusters formed at the poles.

Figure 3.6 shows the average energy and density as functions of α. Curiously, the case of the spherical shell ($\alpha = 1.0$) corresponds to one of the most energetically unfavourable structures (only surpassed by the case of $\alpha = 0.9$) and also to the worst packing. In contrast, for $\alpha = 0.4$ the system reaches the best packing and the best energetic stability. The double-helices for $\alpha = 2.5$ and 3.5 correspond to local energy maxima, whereas multi-helical structures obtained for $\alpha = 2.0$, 3.0 and 4.0, correspond to local minima.

3.3 Summary and conclusions

In this Chapter, we have performed a MC study of colloidal particles with competing interactions confined in spherical and ellipsoidal shells. The particles interact through the SWL potential.

We found that the confinement into spherical shells promotes the formation of curved cylindrical clusters for conditions at which the hexagonal cylindrical phase is the stable phase in bulk. This occurs as long as the width of the spherical shell is close to the radius of the cylindrical aggregates in the bulk. Interestingly, we found that the ordered structures formed by the colloidal fluid correspond to geometrical solutions of the problem of the longest-rope on the surface of a sphere when the radius of the sphere and the radius of the rope are specified. We also observed that, from a thermodynamic point of view, different structures are very similar since small energy and density fluctuations can induce the transition from one to another. Thus, all the structures obtained for a given spherical shell size can be formed with approximately the same amount of material (average number of particles) and the same average energy.

We also showed that transforming the spherical shell with $R_{out} = 12.5\sigma$ into an ellipsoidal one can induce structural transitions in the colloidal fluid. The transformation was done in such a way the width of the shell and the total volume was kept constant. In particular, we observed that the confinement into oblate shells favours the formation of ordered flattened toroidal structures whereas the prolate shells favour the formation of multi-helical structures. We found that the packing of the system is improved by confinement in both oblate and prolate shells. Energetically, confinement in spherical shells seems unfavourable compared with confinement in ellipsoidal shells. Curiously, in the most flattened oblate shell considered ($\alpha = 0.4$), the colloidal fluid exhibits the best packing and the minimum average energy.

Chapter 4

Confinement in bicontinuous porous materials

This chapter explores the possibilities that the confinement in three-dimensional ordered porous materials offers to modulate the structure of colloidal systems with competing interactions. We model the structure of the porous materials using triply periodic surfaces which describe the interface position in bicontinuous phases. We consider three families of porous materials modelled as cubic primitive (P), diamond (D) and gyroid (G) bicontinuous phases. We tune the colloidal fluid structure by changing both the morphology and the pore size of the materials. We use Monte Carlo simulations to study the thermodynamic and structural properties of the system.

In previous works, some authors have proposed different applications of template-assisted fabrication. In particular, using this technique it has been possible to assemble colloidal particles on patterned solid surfaces to create arrays of colloidal aggregates with potential applications on photonics and electronics [98]. Furthermore, self-assembly of diblock copolymers has been used to assist the conceptual design of templates for lithography[99], to direct the synthesis of nanoparticles while confined within a matrix carbon[100], and to synthesize mesoporous materials[101].

Typically, nanofabrication techniques are used in bidimensional or quasi-bidimensional systems such as surfaces and thin films. A new method of three-dimensional template-assisted fabrication that expands the possibilities of designing novel nanomaterials is proposed in this chapter. This chapter is based on the reference[102].

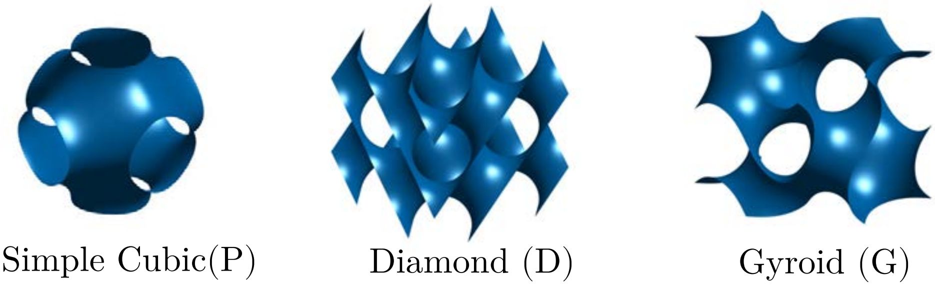

Figure 4.1: Morphology of the porous materials. One unit element of each material is depicted. The surface describes the boundary of the pores defined by equations 4.1, 4.2 and 4.3.

4.1 Model and simulation details

As in previous chapters, colloidal particles interact through the square-well-linear potential given in equation 2.1. The parameters are already explained in section 2.1, as well as the values we have assigned them according to reference [24].

We consider porous materials inspired by the topology of bicontinuous phases. Bicontinuous phases can be formed from diblock copolymers[103, 104], as well as from lipid-water and oil-water-surfactant mixtures[105]. Mathematically, porous materials with the structure of simple cubic (primitive P), diamond (D) and gyroid (G) can be expressed as[106],

$$\Psi_P(x,y,z) = \cos\left(\frac{2\pi n}{L}x\right) + \cos\left(\frac{2\pi n}{L}y\right) + \cos\left(\frac{2\pi n}{L}z\right) \tag{4.1}$$

$$\Psi_D(x,y,z) = \cos\left(\frac{2\pi n}{L}(x-y)\right)\cos\left(\frac{2\pi n}{L}z\right) + \sin\left(\frac{2\pi n}{L}(x+y)\right)\sin\left(\frac{2\pi n}{L}z\right) \tag{4.2}$$

$$\Psi_G(x,y,z) = \sin\left(\frac{2\pi n}{L}x\right)\cos\left(\frac{2\pi n}{L}y\right) + \sin\left(\frac{2\pi n}{L}y\right)\cos\left(\frac{2\pi n}{L}z\right) + \sin\left(\frac{2\pi n}{L}z\right)\cos\left(\frac{2\pi n}{L}x\right) \tag{4.3}$$

where x, y and z are the Cartesian coordinates, L is the side length of the simulation box, and n is the number of unit elements that fit along one axis in the range $[0, L]$. We present the morphology of the porous materials, depicting surfaces corresponding to the equations $\Psi_\alpha(x,y,z) = 0$, where α is P, D and G, in Figure 4.1.

Because of the presence of the porous materials, the colloidal particles experience an external potential. In this study, we consider hard impervious materials. The external potential is, thus, defined as follows,

$$\mathcal{V}(\mathbf{r}_i) = \begin{cases} \infty, & \Psi_\alpha(\mathbf{r}_i) \geq 0 \\ 0, & \Psi_\alpha(\mathbf{r}_i) < 0 \end{cases} \tag{4.4}$$

Here $\mathbf{r}_i$ is a vector containing the position of the particle i. Due to the properties of the bicontinuous surfaces, by placing the pore walls at $\Psi_\alpha(x, y, z) = 0$, the porous materials divide the simulation box into two regions of equal volume, one is occupied by the confined colloidal particles, while the other is the impenetrable porous material. To avoid ambiguity, we calculate the number density as $\rho = N/L^3$.

The total energy of the system is given by,

$$U_{tot} = \sum_{i=1}^{N-1} \sum_{j>i}^{N} u_{SALR}(r_{ij}) + \sum_{i=1}^{N} \mathcal{V}(\mathbf{r}_i), \tag{4.5}$$

Where N is the total number of particles and $u_{SALR}(r_{ij})$ is given by equation 2.1.

We investigate the structure of the SALR fluid confined in these porous materials using Monte Carlo simulations in the grand canonical ensemble (μ, V, T). Simulations are performed at temperature $T = 0.35$ and at values of chemical potential in the range $-2.65 \leq \mu \leq -2.10$. For such thermodynamic conditions, the face-centred cubic (FCC) cluster-crystal and the hexagonal cylindrical phases are stable in bulk [24]. We apply periodic boundary conditions along the three directions of the space. We can control the size of the pores by varying the number of unit elements inside the simulation box, i.e., assigning different integer values to n in equations 4.1, 4.2 and 4.3. For a given value of L, the pore size adopts discreet values depending on the integer number n. To explore different system and pore sizes, we consider $12\sigma \leq L \leq 30\sigma$ and integer values of n within the range $1 \leq n \leq 6$. We are only interested in promoting the formation of ordered microphases, thus results are only reported for those combinations of L, n and μ that lead to either ordered spherical or cylindrical clusters.

The equilibration times are different depending, mainly, on the system size. Averages are taken over 4×10^9 Monte Carlo steps, from which 4×10^5 independent configurations are taken for averaging the local density. A Monte Carlo step is defined as a trial move that can be a displacement, addition or deletion of a particle.

To analyze the structure of the cluster-crystals that we obtain, we measure different properties.

Local density is used to plot iso-density surfaces that allow us to visualize the shape and position of the clusters. We also identify the clusters using a cluster search algorithm [80], adopting the convention that two particles belong to the same cluster if the distance between them is lower than the attractive range $\lambda\sigma$. Additionally, we calculate both the particle-particle and the cluster-cluster radial distribution functions, using the centre of mass of the clusters for the latter. The cluster-cluster radial distribution function allows us to determine the superstructure formed by the clusters. We calculate both distribution functions up to a distance equal to half the diagonal of the cubic simulation box, rather to half the edge length as usual [107, 108]. Finally, we also calculate the Bond Orientational Order Diagrams (BOOD). These diagrams are created by projecting the bonds formed by the clusters and its first coordination shell on a unit sphere. The centres of mass of the clusters are used for the evaluation of the BOOD, and the first coordination shell is defined as those clusters that are at a distance shorter than the first minimum in the cluster-cluster distribution function. We project the unit sphere in a plane using the area-preserving Lambert projection for easier visualization. Different crystalline structures are characterized by different BOOD, which makes these diagrams very useful to identify the structure and symmetry of crystals [109].

4.2 Discussion and results

Our goal in this study is to investigate how the confinement in ordered three-dimensional porous materials influences the self-assembly of colloidal aggregates. We are interested in the formation of cluster-crystal phases with different symmetries that are not stable in bulk. For that purpose, we control the topology, symmetry and geometry of the porous material, looking for the right structural parameters that lead to novel cluster-crystal phases. We study three different models for porous materials: cubic primitive, diamond and gyroid.

4.2.1 Confinement in the P material

We start the discussion by presenting the results for the simple cubic material (See Figure 4.1 and Equation 4.1). This material has the simplest porous network from the ones we consider in this chapter. We can describe the P material structure as an assemblage of almost spherical cavities forming a simple cubic lattice, which are connected by necks narrower than the spherical cavities. The sizes of the necks and cavities can be modified by changing the number of unit elements, n, which are accommodated in a cubic box of constant side length, L. The diameter of the spherical cavities is given by the lattice constant of the material, $D_s = L/n$, whereas that of the cross-section of the necks is approximately, $D_n \approx 3/5D_s$. We generate three porous structures by assigning, $n = 2, 3$ and 4 unit elements in a box of length $L = 20\sigma$. The spherical cavities in these materials have diameters, $D_s = 10\sigma$, 6.667σ and 5.0σ, and the diameters of the cross-section of the connecting necks are $D_n = 6.0\sigma$, 4.0σ and 3.0σ, respectively.

First, we choose a thermodynamic state at chemical potential, $\mu = -2.40$, and temperature, $T = 0.35$, for which the FCC cluster-crystal phase is stable in bulk.

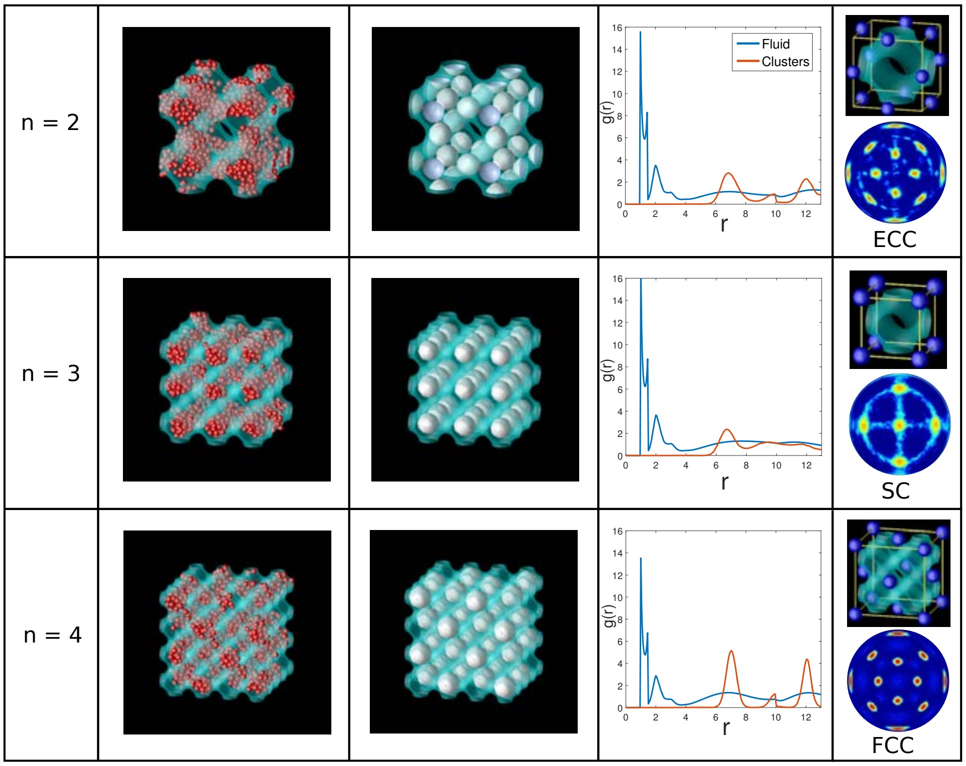

Figure 4.2: Structures of the SALR colloidal fluid confined in the material P for edge length $L = 20\sigma$ and different pore sizes,n. The simulations are performed for $\mu = -2.40$ and $T = 0.35$, conditions for which the FCC cluster crystal is stable in bulk. The values of n are shown in the first column, the second column shows a snapshot of the particles at equilibrium, and the third column shows the local density of the colloidal fluid. The gray surface corresponds to the iso density surface for $\rho_{iso} = 0.4$, and the cyan surface corresponds to the pore walls. The average densities are $\langle \rho \rangle = 0.1055(4)$, 0.1199(9), 0.1259(3) for $n = 2$, 3, 4, respectively. The fourth column shows particle-particle (blue) and cluster-cluster(red) pair correlation functions. In the fifth column, the BOOD, calculated using the centres of mass of the clusters, and the cluster crystal unit cells are depicted.

As can be observed in Figure 4.2, the size and distance between cavities in the porous network play an important role in the arrangement of the confined colloidal fluid. This figure presents all the structural information we use to characterize the obtained structures (local density isosurfaces, particle-particle and cluster-cluster pair correlation functions, unit cells and BOOD). In the three cases, the colloidal fluid assembles into spherical clusters, but the spatial distribution of such clusters changes depending on the size and distance between cavities. It is interesting to note that the cluster size does not change much with n. For all cases, the radius of the clusters is $r'_0 = 1.92\sigma$ (measured from local density plots at $\rho_{iso} = 0.4$). Thus, the cluster size is mainly determined by the pair potential rather than from the pore geometry.

For $n = 2$, clusters preferentially place at the necks of the material. The distance between adjacent spherical cavities is too large (10σ) so that placing the clusters inside the spherical cavities would lead to a low-density phase. Filling the necks of the porous network, a better packed ordered structure can be obtained, for which the distance between nearest neighbour clusters is 7.071σ. In this structure, designated as the edge-centred-cubic crystal (ECC), clusters are located at the midpoints of the bonds of a simple cubic lattice (See Figure 4.2, first row). The ECC has eight neighbours in the first coordination shell at a distance $\sqrt{2}/2L/n$ and six neighbours in the second shell at a distance L/n. The BOOD, computed up to the first coordination shell, shows twelve bright spots, instead of eight, as we would expect from the number of neighbours in the first coordination shell. However, as there are two different local orientations of nearest neighbours in the ECC, it results on the appearance of four additional bright peaks in the BOOD.

For $n = 3$, the clusters are located inside the spherical cavities, exactly one cluster per cavity, forming a simple cubic crystal (SC) (See Figure 4.2, second row). In this case, the distance between necks is too small (4.71σ) to avoid repulsion between neighbour clusters located at these sites. Instead, the distance between spherical cavities (6.67σ), allows the system to avoid repulsion between nearest clusters and still exhibit efficient packing. The BOOD has six bright regions, which are consistent with an SC lattice. Even though the SC cluster-crystal is unstable in bulk for the model considered in this work (Equation 2.1), we have demonstrated that it can be stabilized inside a P porous material. At this point, we wonder if our simulations can be affected by finite size effects, i.e. if the results would be the same for a larger system with the same pore size. To check that, besides the calculations for $L = 20\sigma$ and $n = 3$, we perform the calculations for two additional system sizes: $L = 13.33\sigma$, $n = 2$ and $L = 26.667\sigma$, $n = 4$. In the three cases, the fluid assembled into the SC cluster-crystal. Thus, we can conclude that the size of the system does not influence the ordering of the clusters in the porous material.

For $n = 4$, the clusters are still placed inside the spherical cavities, but not all are occupied. The distance between the centres of the cavities (5σ) is too short to enable full occupation. The system, thus, opts to occupy alternate cavities with clusters forming a face-centred-cubic (FCC) lattice (See Figure 4.2, third row), which is the stable phase in bulk for these thermodynamic conditions [24]. The distance between the nearest clusters is 8.66σ, large enough to avoid repulsion. The BOOD exhibits twelve bright regions distributed on the sphere in the way expected for an FCC lattice [109]. The ECC and FCC BOODs look similar due to the structural similarity between these two structures. If we shift the FCC structure half lattice constant, we obtain the ECC structure but with an additional cluster in the centre of the unit cell. Another important thing to note is that the FCC cluster-crystal exhibits a cleaner BOOD, with lower probability of finding neighbour clusters outside the lattice sites. Instead, the BOOD of the ECC shows some signs of large movements of the clusters between lattice sites. We associate this to the fact that, whereas in the two previous cases the occupied sites were directly connected, this does not apply anymore to this porous structure, enhancing the nucleation of clusters at the corresponding lattice sites.

If we compare the cluster-cluster pair distribution functions for all the obtained structures in the P material, we note that they are similar, with the first two peaks appearing at similar distances. As the ratio between distances of the first and second coordination shells is the same in the three structures ($1/\sqrt{2}$) (SC, ECC and FCC), this result is somewhat expected. However, they differ in the number of clusters in these two first shells: the ECC has eight first neighbours and six second neighbours, the SC has six first neighbours and twelve second neighbours, and the FCC has twelve first neighbours and six second neighbours. This is consistent with the pair correlation functions reported here, with the FCC exhibiting the stronger first peak and the SC exhibiting the weaker first peak. Additionally, the three structures have quite broad peaks, especially the first one, which indicates that the clusters move freely within the cavities in which they are hosted. As a final comment on the pair correlation functions, we say that the particle-particle distributions are similar for all the cluster-crystals described, meaning that the local structure of the fluid is the same in all cases.

Now, we move into a different region of the phase diagram. Keeping the same temperature, $T = 0.35$, we increase the chemical potential ($\mu = -2.10$) to reach the thermodynamic conditions at which the hexagonal cylindrical phase is stable in bulk [24]. We present the simulation results in Figure 4.3. Under these conditions, the colloidal fluid assembles into both cylindrical and spherical clusters, even though the cluster phases are not stable in bulk.

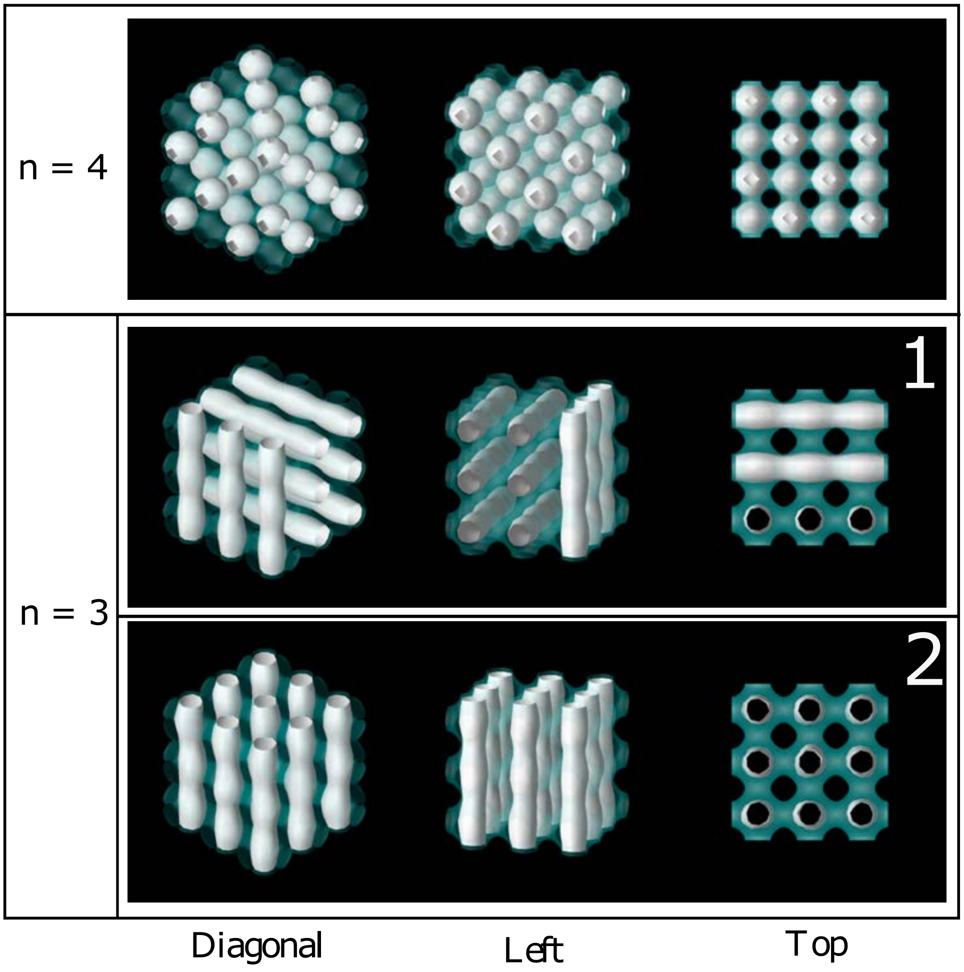

Figure 4.3: Structures of the SALR colloidal fluid confined in the material P for edge length $L = 20\sigma$ and different pore sizes,n. The simulations are performed for $\mu = -2.10$ and $T = 0.35$, conditions for which the hexagonal cylindrical phase is stable in bulk. The gray surface corresponds to the iso-density surface for $\rho_{iso} = 0.4$, and the cyan surface corresponds to the pore walls. The average densities are $\langle\rho\rangle = 0.1669(4)$, $0.1836(8)$, $0.1842(8)$, for $n = 4$, 3 case 1 and 3 case 2, respectively. Three views are shown for each structure. For $n = 4$, an FCC cluster-crystal is obtained.

When $n = 3$, the system only forms cylindrical clusters. The cylindrical aggregates grow through the cavities forming layers in which the aggregates are parallel but are stacked randomly, meaning that contiguous layers can be oriented parallel or perpendicular to each other (see Figure 4.2, $n = 3$). Since the range of the pair potential is 4σ, we expect that the interactions between colloidal particles belonging to adjacent cylindrical clusters (located in channels separated by a distance of $L/n = 6.667\sigma$) are negligible. Note that in the bulk hexagonal phase, the separation distance between adjacent cylindrical aggregates is smaller ($L_0 = 6.20\sigma$). According to our results, parallel and perpendicular configurations appear to have similar stability. The average energy and density are practically the same for both configurations (Figure 4.2, $n = 3$): (1) $\langle \rho \rangle = 0.1836$ and $\langle u \rangle = -3.2949$; (2) $\langle \rho \rangle = 0.1842$ and $\langle u \rangle = -3.2925$. The radius of the cylindrical clusters is $r_0' = 1.68\sigma$, almost identical to the equilibrium radius of the bulk cylindrical phase under the same thermodynamic conditions, $r_0 = 1.70\sigma$.

For $n = 4$, the size of the spherical cavities is smaller, and the confined colloidal fluid does not longer form cylindrical clusters as in bulk. Instead, the system assembles spherical clusters of radius $r_0' = 2.17\sigma$, slightly larger than the radius of the clusters found at a lower chemical potential in the primitive porous material, at the three considered pore sizes (Figure 4.2). An FCC cluster crystal is still formed even at these conditions for which we expect a cylindrical phase. The bottlenecks that link the spherical cavities of the porous network have a small size ($D_n \approx 3\sigma$) to host straight cylinders of radius comparable to those obtained for $n = 3$. Thus, cylindrical aggregates could only fit in these channels if they showed periodic narrowing at the necks. This is, presumably, unfavourable energetically, the reason why the confined colloidal fluid prefers to organize into spherical clusters forming an FCC lattice, similar to the behaviour observed at a lower chemical potential. The fact that the FCC cluster-crystal can survive up to higher chemical potentials than in bulk demonstrates the high stability of this phase but also the phase diagram shift experienced by fluids under confinement [59, 52].

4.2.2 Confinement in the D material

In this section, we explore the colloidal fluid behaviour when confined in pores with a diamond structure. We start by presenting the results for pores with $L = 20\sigma$ and different values of n to modulate the cavities size. We perform simulations at $T = 0.35$ and $\mu = -2.40$, i.e., the same thermodynamic conditions used in the previous section with the P material, and for which the FCC cluster-crystal is the stable phase in bulk. In this case, we obtained ordered structures for the D porous materials with $n = 1$ and 2 (See Figure 4.4).

In the D material, the distance between the nearest lattice sites is $D_s = \sqrt{3}L/4n = 8.667L/n$ and that between the midpoints of the connecting pores is $D_n = \sqrt{2}L/4n = 7.071L/n$. For $n = 1$, the clusters fill the midpoint of the pores that connect adjacent diamond lattice sites, with an analogous behaviour found for the primitive porous matrix with $L = 20\sigma$ and $n = 2$. For this arrangement, the distance between adjacent connecting pores prevents repulsion between clusters and promotes better packing than occupying the lattice nodes. Consequently, the spherical aggregates organize

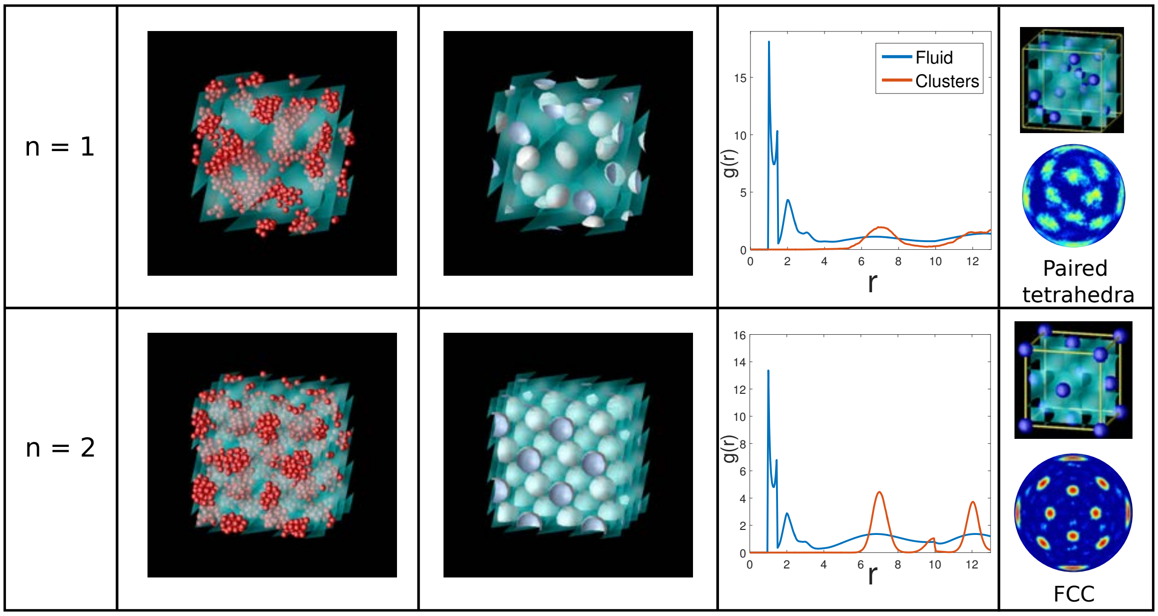

Figure 4.4: Structures of the SALR colloidal fluid confined in the material D for edge length $L = 20\sigma$ and different pore sizes,n. The simulations are performed for $\mu = -2.40$ and $T = 0.35$, conditions for which the FCC cluster crystal is stable in bulk. The values of n are shown in the first column, the second column shows a snapshot of the particles at equilibrium, and the third column shows the local density of the colloidal fluid. The grey surface corresponds to the isodensity surface for $\rho_{iso} = 0.4$, and the cyan surface corresponds to the pore walls. The average densities are $\langle\rho\rangle = 0.0884(8)$, and $0.1301(3)$, for $n = 1$, 2, respectively. The fourth column shows particle-particle (blue) and cluster-cluster(red) pair correlation functions. In the fifth column, the BOOD, calculated using the centres of mass of the clusters, and the cluster-crystal unit cells, are depicted.

into the pyrochlore crystal structure, which is the resultant structure when the midpoints of the diamond lattice sites are occupied. The pyrochlore structure has been previously observed in silicate compounds (high cristobalite), in triblock Janus particles[110, 111] and in a square shoulder isotropic model [112].

For smaller pores, when $n = 2$, the distance between the diamond lattice sites is $D_s = 4,33\sigma$ and that between the pores connecting these sites is $D_n = 3.52\sigma$. In this case, both distances are too small for the clusters to place without experiencing considerable repulsion. Thus, the alternative of the system is to fill with clusters the second neighbour cavities of the D porous structure separated by a distance $\sqrt{2}L/2n = 7.071$, forming an FCC cluster-crystal. The solution that the system finds is natural if we note that a diamond lattice can also be seen as two interpenetrated FCC lattices displaced a distance $L/4n$ along the diagonal. The resulting FCC structure can be obtained occupying only one of these two interpenetrated lattices.

We present the pair distribution functions of these two cluster-crystals in the fourth column of

Figure 4.4. The particle-particle distributions are very similar for the two values of n and for the cluster-crystals obtained in the previous section for the P material. Regarding the cluster-cluster distribution functions, there are some remarkable points to comment. The pyrochlore structure has six neighbours in the first coordination shell and twelve in the second, the latter appearing at a distance $3/\sqrt{3}$ larger than the first shell in a perfect lattice. This is consistent with the cluster-cluster distribution of the pyrochlore structure we report here whose first and second peaks appear at distances $7/\sigma$ and $12/\sigma$, approximately. The cluster-crystal obtained in the D material for $n = 2$, instead, shows peaks at distances 7σ and 10σ, with a ratio between distances close to the value $\sqrt{2}$, corresponding to a perfect FCC lattice. The BOODs also confirm what is observed from the pair correlation functions, both display twelve bright spots that are blurry in the pyrochlore and quite sharp in the FCC. The pyrochlore shows twelve peaks because, although there are six neighbours in the first coordination shell, they are oriented in two different local environments in the crystal. Note that the FCC cluster-crystal lattice obtained in the P material also exhibited sharper peaks compared to the other formed cluster-crystals. As in that case, it reflects that, besides being the stable phase in bulk, when the FCC cluster-crystal is formed the occupied sites in the D material are not directly connected.

So far, we have obtained cluster-crystals that somehow are related to the diamond structure. The pyrochlore structure is the result of the occupation of the midpoints of the diamond lattice sites, whereas the FCC is a structure from which the diamond lattice can be constructed by interpenetrating a second FCC. Nevertheless, at this point, we find it somewhat surprising that the colloidal fluid has not assembled into a diamond cluster-crystal when confined in a porous material with a diamond structure. A priori, we would expect that the D material would act as a mould to stabilize the diamond cluster-crystal. However, the confined fluid prefers to assemble into other cluster-crystals. We speculate that one possible reason for not obtaining the diamond cluster-crystal is that the dimensions of the porous material have not been chosen accordingly to promote its formation. Reviewing the cluster-crystals obtained so far for P and D materials, we observe two common features: the spherical clusters exhibit approximately the same size ($r'_0 \approx 1.92\sigma$) and the inter-distance between nearest clusters is within the range $6.7 - 8.6\sigma$, that guarantees that the repulsion between clusters is low. The distance between lattice sites in the system with $n = 1$ is within the upper limit of this range, but we obtain a higher density structure by occupying the midpoints of the pores connecting adjacent diamond lattice sites (pyrochlore). On the other hand, in the D material with $n = 2$, the distance between the lattice points becomes too short; thus repulsion between clusters located at those sites is expected to be high. Thus, we decide to look for the diamond cluster-crystal by modifying the length of the simulation box edge within the range $L = 13 - 17\sigma$, keeping $n = 1$ constant. The distance between nearest diamond lattice sites in porous networks with these dimensions ranges from 5.6σ to 7.36σ, and that between the midpoints of nearest connecting pores goes from 4.95σ to 6.01σ. In principle, these values are coherent with the formation of the diamond cluster-crystal, and simulations confirm its appearance for $13.5\sigma \leq L \leq 16\sigma$ and $n = 1$. Having identified the appropriate unit cell dimensions, we doubled the system size, i.e. we set the edge length to $2L$ and $n = 2$ so that the unit cell dimensions remain constant. We doubled the system to verify if the results obtained for one unit cell are affected by finite-size effects.

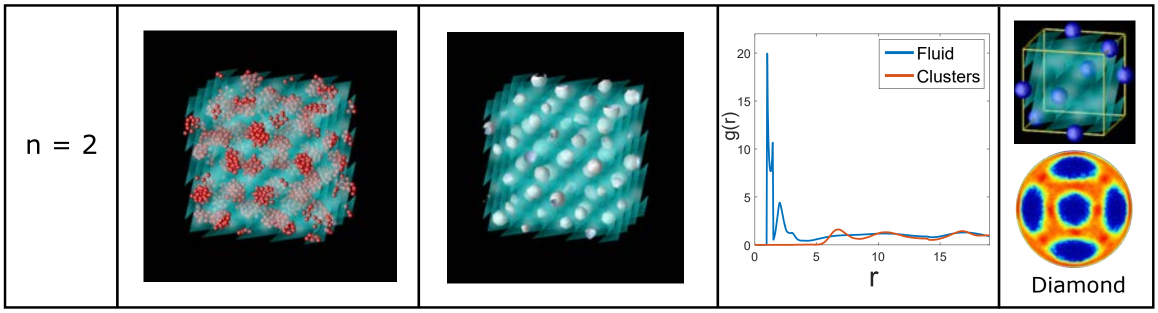

Figure 4.5: Structure of the SALR colloidal fluid confined in the material D for edge length $L = 28\sigma$ with $n = 2$. The simulations are performed for $\mu = -2.48$ and $T = 0.35$, conditions for which the FCC cluster crystal is stable in bulk. The second column shows a snapshot of the particles at equilibrium, and the third column shows the local density of the colloidal fluid. The gray surface corresponds to the iso density surface for $\rho_{iso} = 0.4$, and the cyan surface corresponds to the pore walls. The average density is $\langle\rho\rangle = 0.08386(146)$. The fourth column shows particle-particle (blue) and cluster-cluster(red) pair correlation functions. In the fifth column, the BOOD, calculated using the centres of mass of the clusters, and the cluster-crystal unit cells and are depicted.

As can be observed in Figure 4.5, in this doubled system, the fluid assembles, on average, into a diamond cluster-crystal, but the clusters are free to move and usually adopt elongated shapes. Nevertheless, the diamond lattice is distinguished in the local density plots, and the cluster-cluster pair distribution function and BOOD are consistent with those of diamond. Diamond lattice has four sites in the first coordination shell at distance $\sqrt{3}L/4n$ and twelve in the second shell at $L/\sqrt{(2)}n$. The BOOD of perfect diamond shows eight bright regions due to two possible orientations of the first shell in the crystal. The BOOD presented in the fifth column of Figure 4.5 shows the eight characteristic peaks, but they are connected by regions of large probability that evidence the high mobility of the clusters. Clusters often leave their lattice nodes, also occupying the connecting pores of the D material. We think that the diamond cluster-crystal is more stable in the smaller system with one unit cell because this small system might be over-constrained, artificially, favouring the diamond crystal formation. It is plausible that the more disordered structure found in the larger system has higher entropy but similar energy and packing than "perfect" diamond. Possibly, the increase of entropy of partially disordered structures might be negligible in small periodic systems but becomes important once that clusters can adopt different configurations in adjacent unit cells. We also note that, different from the P material in which cavities at the lattice sites were nearly spherical, in the D material the lattice nodes are delimited by surface folds that are weak nucleation points and thus they might favour more disordered structures. Some authors have obtained diamond-like structures in colloidal systems by designing specific isotropic potentials with competing interactions [112, 113], and recently using DNA strands to direct the self-assembly of such structures to develop materials with applications in photonics [114]. However, the structures obtained in the works mentioned above are simple crystals because each lattice position is occupied by an individual particle, unlike the structure we present in this chapter that is composed of clusters.

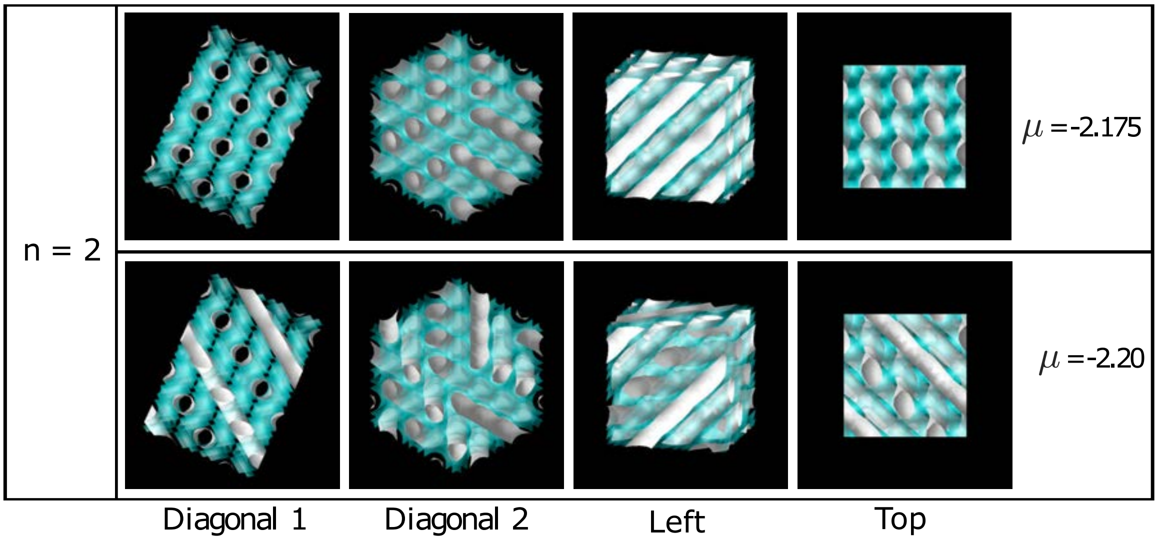

Figure 4.6: Structures of the SALR colloidal fluid confined in the material D for edge length $L = 20\sigma$ and $n = 2$. The simulations are performed for $\mu = -2.175$ and -2.200 as indicated, and $T = 0.35$, conditions for which the hexagonal cylindrical phase is stable in bulk. The gray surface corresponds to the iso-density surface for $\rho_{iso} = 0.4$, and the cyan surface corresponds to the pore walls. The average densities are $\langle\rho\rangle = 0.1877(5)$, $0.1861(4)$, for $\mu = -2.175$, -2.200, respectively. Four views are shown for each structure.

Now we move to study the structural properties of the hexagonal cylindrical phase confined in D material. Knowing the structure of the material, it seems plausible that the colloidal fluid can still form a hexagonal arrangement of cylindrical clusters growing along the pores parallel to the face diagonals of the cube ([110] direction). Indeed, this is what we found for $L = 20\sigma$ and $n = 2$, at a chemical potential, $\mu = -2.175$ (See Figure 4.6). Under these conditions, the distance between the nearest cylindrical aggregates is imposed both by the pair interaction potential and by the D network structure. In this case, the average distance between nearest cylindrical clusters is $\sqrt{2}L/2n = 7.07\sigma$. Clusters are no longer straight as in bulk; they adapt their cross-sections to a sinusoidal shape to match the morphology of the confining pore. Our results reveal that this cylindrical structure appears to be degenerate with other configuration in which cylinders in contiguous layers are randomly oriented along the possible directions allowed by the confining material. In the structure presented in Figure 4.6 for $\mu = -2.200$, the cylindrical clusters are parallel to directions [110] and [101] in alternate layers, thus cylinders that belong to two contiguous layers form an angle of $\pi/3$. Both structures exhibit virtually the same energy ($\langle u \rangle = -3.30$, within the range of fluctuations for both configurations) and density ($\langle \rho \rangle = 0.188$ for parallel cylinders and $\langle \rho \rangle = 0.186$ for cross-layered cylinders). We estimate the radius of the cylindrical clusters in both examples around $r_0' = 1.95\sigma$, which is quite similar to that found in the P material.

Using three-dimensional templating, multi-layered cylindrical arrangement with alternating orientations, similar to those reported in this chapter for P and D materials, have been already obtained in experiments with block copolymers[115]. This is further evidence that systems with competing interactions behave similarly under confinement regardless of the physical origin of their interactions.

4.2.3 Confinement in the G material

The last type of bicontinuous porous material that we consider is the G material. These pores have a gyroid structure and are the most complex ones studied in this chapter. The G bicontinuous network exhibits channels running along the diagonal of the simulation box ([111] direction) and along the x-axis, which are interconnected by additional small cavities. Thus, three channels meet at each junction (8 junctions per unit cell, and $8(3/2) = 12$ connecting cavities). The junctions and connecting cavities form octagonal helical structures of alternating handedness that are interconnected by porous segments. The porous materials are built by setting the edge length of the simulation box, $L = 24\sigma$.

We perform the simulations in thermodynamic conditions at which the FCC cluster crystal is the stable phase in bulk ($\mu = -2.46$, $T = 0.35$). We found cluster-crystals that are not stable in

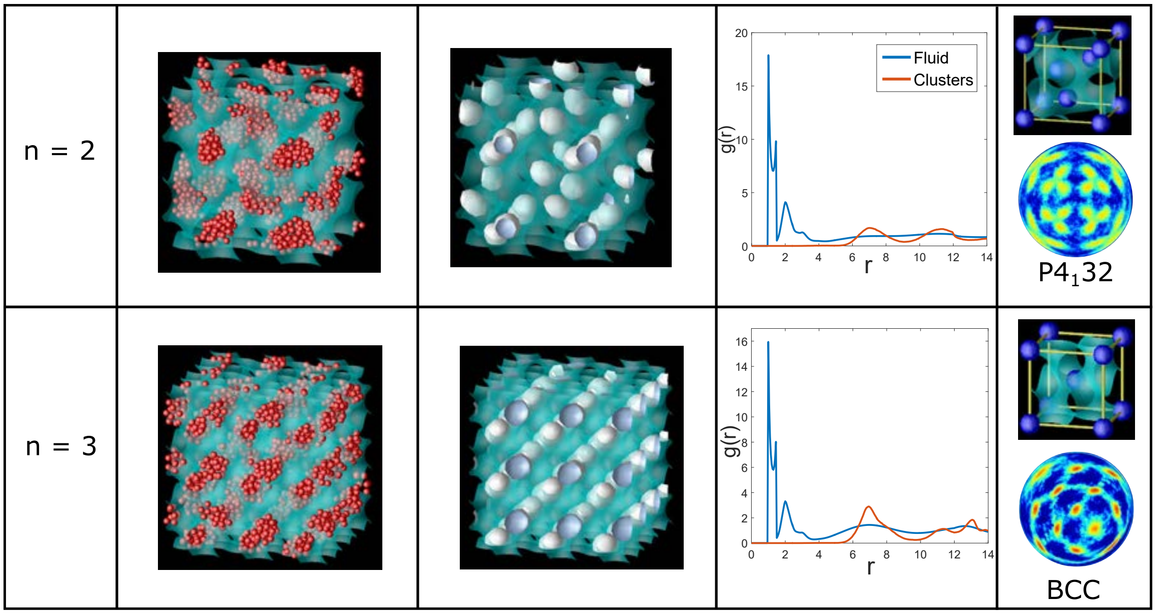

Figure 4.7: Structures of the SALR colloidal fluid confined in the material G for edge length $L = 24\sigma$ and different pore sizes,n. The simulations are performed for $\mu = -2.46$ and $T = 0.35$, conditions for which the FCC cluster crystal is stable in bulk. The values of n are presented in the first column, the second column shows a snapshot of particles at equilibrium, and the third column shows the local density of the colloidal fluid. The gray surface corresponds to the iso density surface for $\rho_{iso} = 0.4$, and the cyan surface corresponds to the pore walls. The average densities are $\langle\rho\rangle = 0.08743(109)$, and $0.1148(6)$, for $n = 2$, 3, respectively. The fourth column shows particle-particle (blue) and cluster-cluster(red) pair correlation functions. In the fifth column, the BOOD, calculated using the centres of mass of the clusters, and the cluster crystal unit cells and are depicted.

bulk for porous matrices with $n = 2$ and $n = 3$. We present the results in Figure 4.7.

In the case of $n = 2$, spherical clusters are arranged into an ordered structure whose unit cell contains four lattice positions. The clusters place at the three-channel junctions, but only half of them are occupied. After identifying the unit cell with the aid of the local density of the confined fluid, using the FindSym software [116, 117], we determine that this structure exhibits $P4_132$ point group symmetry, corresponding to space group 213 in crystallographic tables. In this crystal, each cluster is surrounded by other six clusters in the first coordination shell at an average distance of approximately 7.35σ, and twelve clusters in the second shell at 11.2σ, as shown in the cluster-cluster pair correlation function. The BOOD diagram shows a very distinctive signature formed by 24 bright peaks arranged in clover-shaped groups of three. The appearance of so many peaks in the BOOD is, again, caused by the fact that the first coordination shell of each cluster in the unit cell is oriented differently from each other.

For the porous material with $n = 3$, the spherical aggregates assemble into a BCC lattice.

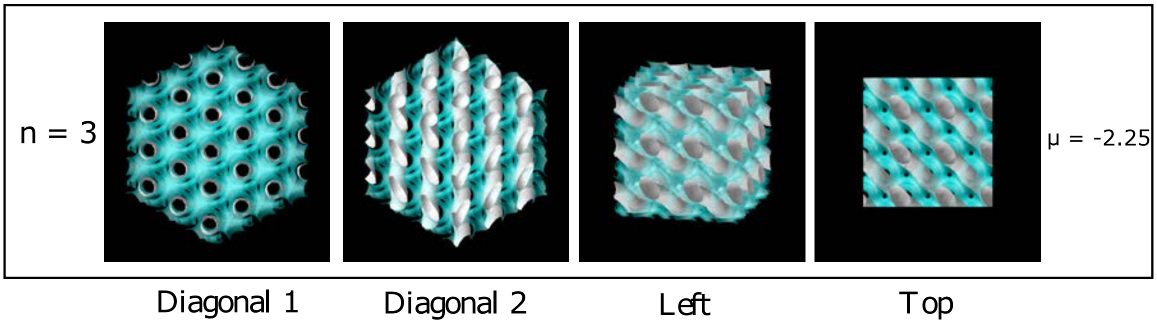

Figure 4.8: Structures of the SALR colloidal fluid confined in the material G for edge length $L = 24\sigma$ and $n = 3$. The simulations are performed for $\mu = -2.250$ and $T = 0.35$, conditions for which the hexagonal cylindrical phase is stable in bulk. The gray surface corresponds to the iso-density surface for $\rho_{iso} = 0.4$, and the cyan surface corresponds to the pore walls. The average densities are $\langle\rho\rangle = 0.1817(4)$. Four views of the structure are presented.

Clusters are now located at the connecting pores between junctions, but only two per gyroid unit element are occupied. The average distance between nearest neighbour clusters, in this case, is about 6.90σ, large enough to avoid significant repulsion. The distance between nearest neighbours in this structure is consistent with the other cluster-crystals obtained in P and D materials. The second coordination shell that contains six clusters is located at about 8.0σ. The distances of the first and second coordination shells are reflected in the cluster-cluster distribution function, that shows a double peak with maxima around these two distances. The BOOD diagram, measured up to the first minimum in the cluster-cluster distribution function, shows 14 bright spots, as it is typical of BCC materials [109]. We can observe a small, but not negligible, probability of finding the clusters at orientations outside the lattice sites, showing that the clusters are relatively mobile in this structure.

To conclude this section, we set a higher chemical potential while keeping the temperature the same ($\mu = -2.25$, $T = 0.35$), conditions at which the hexagonal cylindrical phase is stable in bulk. For such conditions, we only obtain ordered structures for the porous network with $n = 3$. In this case, the confined colloidal fluid assembles into approximately cylindrical clusters arranged into a hexagonal lattice with cylinders oriented along the cube diagonal, as shown in Figure 4.8. The cylinders are not entirely straight, they, again, show a somewhat wavy shape to adapt to the pore morphology. The confining material morphology determines the average distance between the nearest cylindrical aggregates. Six cylindrical aggregates are formed along the cube diagonal so that the distance between nearest cylinders is $\sqrt{3}L/6 = 6.93\sigma$. The estimated equilibrium radius, $r_0' = 2.05\sigma$, is of the same order as those of the cylindrical phases found in the other confining materials.

4.2.4 The effect of temperature

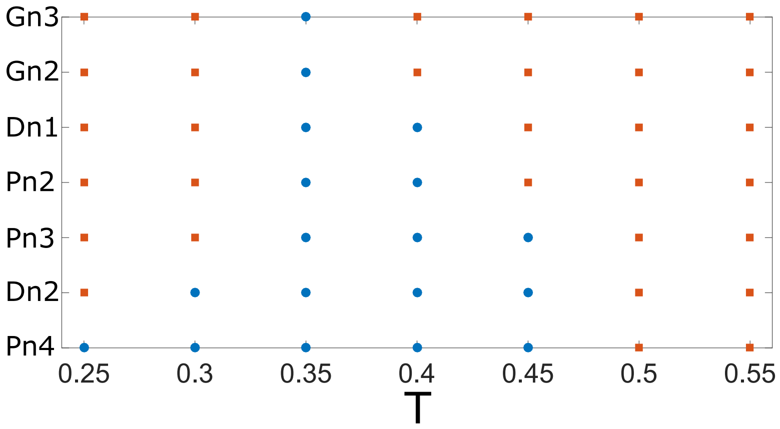

Figure 4.9: Scheme of temperature stability of the cluster-crystals obtained under confinement in different porous materials. Red squares represent states where the structure is not stable, and blue circles represent states of stability. The structures are organized from the most stable (bottom) to the less stable(top).

After identifying the stable cluster-crystals under confinement in different porous materials, we wonder about the stability of such structures when the temperature is varied. We are also interested in investigating if low temperatures can induce intracluster ordering in the crystals. To address this question, we perform simulations in the grand canonical ensemble at the same chemical potential at which cluster-crystals were obtained in the previous sections, and the temperature is varied in the range $0.25 \leq T \leq 0.55$. We expect all the cluster crystal phases to be stable at low temperature, but the region of stability shifts to lower chemical potential as the temperature decreases. However, local order within the clusters might only occur at low temperature for the upper limit of densities for which cluster-crystals are stable.

As we expected, at low temperatures, the amount of confined colloidal fluid increases. In many cases, this results in the growing of elongated clusters through the cavities of the material that link the lattice nodes of the original structure.

On the other hand, as the temperature increases, the amount of confined colloidal fluid decreases, and clusters reduce their size until the structure melts into a cluster-fluid. Nevertheless, as shown in Figure 4.9, there are differences between the different cluster-crystals. As we might expect, the FCC is the most stable phase, whereas those stabilized in the G material are the less stable. Interestingly,

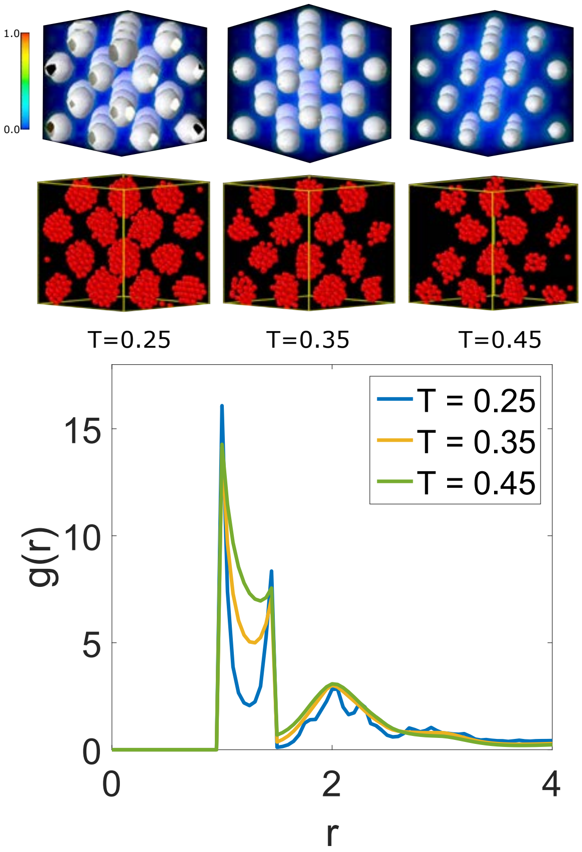

Figure 4.10: Effect of temperature on the FCC cluster crystal obtained for the material P with $n = 4$. The walls of the P material are not shown to visualize better the effect of the temperature on the structure of the system at the particle-scale. The local density maps with iso-density surfaces for $\rho_{iso} = 0.4$ are shown in the top panels. The central panels show snapshots of the particles at equilibrium. The pair correlation functions of the particles, at different temperatures, are shown in the bottom panel. The average density is $\langle\rho\rangle = 0.1960(26)$, $0.1259(3)$ and $0.0767(27)$ for $T = 0.25$, 0.35 and 0.45, respectively.

the FCC cluster-crystal formed in the D material ($n = 2$) seems to be less stable than the one formed in the P matrix ($n = 4$). In the P material, the clusters place at alternate spherical cavities that act as strong nucleation sites. Furthermore, the necks connecting the cavities are too narrow ($D_s \approx 3.0\sigma$) for the clusters to grow through them. Thus, the system achieves a better packing by reordering of the clusters in the spherical cavities. Differently, in the D material, cavities at the lattice nodes are connected along the face diagonals of the simulation box by pores of a comparable dimension to that of the lattice cavities, favouring that adjacent clusters can merge as the temperature decreases.

At $T = 0.25$, the improved packing inside the cavities must be accompanied by a reordering of the particles within the clusters in the FCC structure formed in the P material. In Figure 4.10, we present the results of the effect of the temperature on such structure. From the local density maps, we observe that as the temperature increases, the size of the clusters decreases, as expected. On the other hand, at low temperature, the size increases, reflecting the higher density. As anticipated, colloidal particles within the clusters become often ordered, forming a stacking of triangular layers. The building up of intra-cluster ordering is reflected in the particle-particle distribution function at $T = 0.25$. The two first peaks are sharp, and the third and fourth peaks are now split into additional smaller but visible peaks. Some previous works have reported solid-like ordered microphases [36, 118, 119]. This feature seems to be common in colloidal systems interacting via potentials with a minimum in the short-attractive range. Since the square-well-linear potential has a constant-energy attractive interaction, solid-like microphases are not often found, although they might appear at very low temperature [18, 24, 25]. Our results reveal that confinement can be used to promote local ordering of clusters. In Chapter 5, we will discuss more on local ordering within clusters, in both bulk and confinement.

4.3 Summary and conclusions

In this chapter, we have studied the possibility of using ordered porous materials as three-dimensional templates to direct the self-assembly of colloidal fluids with competing interactions into ordered microphases that might be potentially useful in nanotechnology. We study the assembly of a SALR fluid in porous materials modelled as primitive cubic (P), diamond (D) and gyroid (G) bicontinuous phases. We used both the pore size and the topology of the network as control variables to promote the formation of novel ordering of colloidal clusters.

These porous materials, indeed, modulate the structure of the confined colloidal fluid. For a given porous structure, and thermodynamic conditions at which the cluster-crystal phase is stable in bulk, different cluster-crystals can be obtained by varying the size of the unit elements of the porous networks, so that both the pore size and distance between pores change. Besides having obtained cluster-crystals with the same structure as the confining material (in the case of P and D porous materials, although with some defects in the latter case), we found that it is also possible to obtain cluster-crystals with different structure by tuning the unit element of the porous material. If the unit element of the porous network is so big that the distance between nearest lattice positions becomes too large compared to the interaction range, cluster-crystals form by occupying a sub-lattice for which the nearest neighbour sites achieve a better compromise between avoiding repulsive interactions and efficient packing. As a very interesting finding, we could stabilize pyrochlore and diamond structures that are often difficult to achieve using isotropic particles.

Setting the thermodynamic conditions at which the hexagonal phase is stable in bulk, the confined fluid can also adopt different configurations from that found in bulk. Besides having a certain control over the distances between cylindrical aggregates, it is also possible to obtain stacking of layers of cylinders with different orientations.

Despite considerable effort, ordered cluster phases formed by colloids with competing interactions have not been experimentally observed [9, 49]. Our results suggest that an achievable route to obtain such ordered microphases is to use three-dimensional porous materials as templates. The reduced configuration space might promote the formation of ordered microphases with less interference from dynamically arrested states as in bulk [26, 120, 121, 44]. The ordered porous structure enhances the formation, ordering, and stability of clusters. We speculate that the time necessary to form a well-ordered cluster-crystal can depend on the sizes of the pores and their connectivity.

Part II

MD Simulations

Chapter 5

Self-assembly dynamics of colloidal systems with competing interactions

It is somewhat surprising that researchers have not observed ordered microphases yet in experimental colloidal systems. Both theoretical[17, 19] and simulation[24, 25] studies have demonstrated that such ordered microphases should be observed in colloidal systems with competing interactions. The reason why the ordered microphases remain elusive is not clear. Some hypotheses have been formulated, pointing to the slow kinetics of these systems[122, 44, 42], to the typical polydispersity in experiments[47], or even to effects caused by the colloidal suspension that are not correctly accounted for in a simple SALR effective potential[9] (see Section 1.1).

In this chapter, we perform an extensive simulation study using Molecular Dynamics(MD) of a model system of colloidal particles with competing interactions that forms cluster-crystal, hexagonal and lamellar phases. Firstly, we characterize the bulk behaviour of the system, emphasizing the stability and dynamic aspects of the typical microphases observed in systems with competing interactions. Secondly, we conduct a similar study of the system under confinement in slit pores of different widths.

5.1 Model and simulation details

To perform MD simulations, we need to compute the derivative of the pair potential to calculate the forces. We change the potential that we have been using in the previous chapters since it is a piece-wise discontinuous function, which would imply some difficulties in the implementation because it is not differentiable for some values of the distance between particles. Thus, in this chapter, the interaction between colloidal particles is modelled with the effective SALR potential, which results from the combined contributions of a Lennard-Jones $2\alpha - \alpha$, for the attractive part, and a screened electrostatic interaction represented by the Yukawa potential, for the repulsive part.

$$u_{SALR}(r_{ij}) = 4\epsilon \left[\left(\frac{\sigma}{r_{ij}} \right)^{2\alpha} - \left(\frac{\sigma}{r_{ij}} \right)^{\alpha} \right] + \frac{A}{r_{ij}} \exp\left(-r_{ij}/\zeta\right) \tag{5.1}$$

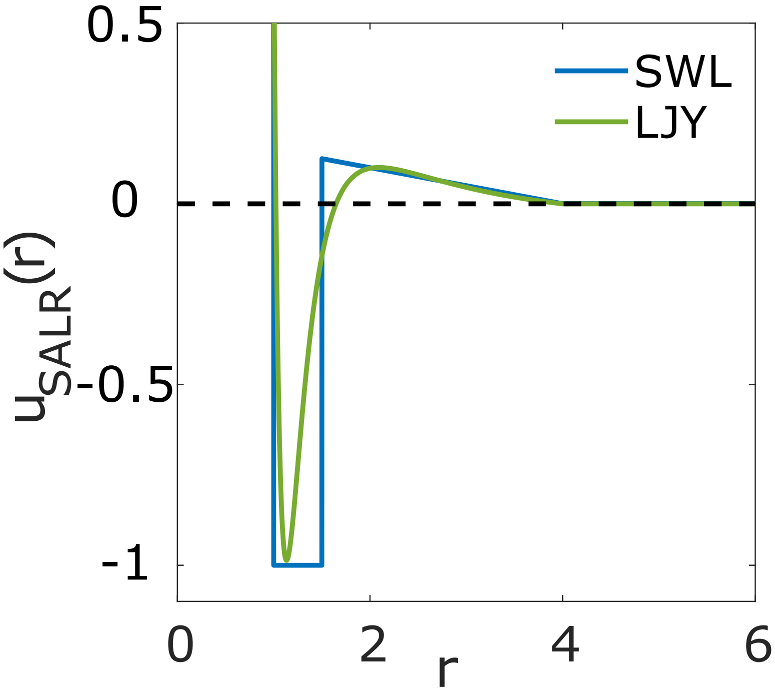

Figure 5.1: Comparison between the SWL from reference [24] and the LJY potential used in this chapter.

The dynamic behaviour of this model potential has been already studied in previous works[122, 22, 23, 123, 124]. Often, the interest is to understand the dynamics of solutions of proteins [4]. We choose a set of parameters so that the model potential exhibits similar features (i.e. similar strength and interactions ranges of the repulsive and attractive contributions) to the square-well-linear potential used in previous chapters and for which the equilibrium phase diagram, at the microphase regime, was reported [24]. We will show that, despite the differences in the functional form, both systems exhibit a qualitatively similar phase behaviour so that we can use the phase diagram of the square-well-linear potential as a guide, knowing beforehand which conditions we should look at for the ordered microphases. In particular, we chose a set of model parameters matching the minimum and maximum of energy in the SWL model, $\epsilon = 1.6$, $\sigma = 1.0$, $\alpha = 6$, $A = 1.3$ and $\zeta = 2.0$. We shifted and truncated the pair potential at a cut off radius $r_c = 4.0\sigma$. In what follows, all the thermodynamic quantities are expressed in reduced units taking σ and ϵ as units of length and energy, respectively. A comparison between the square-well-linear and Lennard-Jones + Yukawa potentials is depicted in Figure 5.1. It is important to stress that our intention is not to directly compare the two models in the spirit of the law of corresponding states [125, 126]. We want to find a continuous SALR potential that stabilises periodic microphases, but that is more suited to MD simulations than the SWL potential.

5.2 Bulk system

This section is based on reference [127]. Before performing the MD simulations, we explored the phase behaviour of the system via MC simulations in the grand canonical ensemble for a range of chemical potential($-1.5 \leq \mu \leq 0.5$) and a temperature of $T = 0.30$. Once we found the region for which the ordered microphases are stable, we chose an equilibrium configuration at the conditions: $\mu = -0.6$, $T = 0.3$ and $L = 20\sigma$ as the initial configuration for the MD simulations. This configuration corresponds to the hexagonal phase with a number of particles, $N = 1991$. We chose this configuration because it is placed roughly at the centre of the ordered microphases stability region.

With the initial configuration ready, the thermodynamic, structural and dynamic behaviour of the model system in equation 5.1 was investigated employing MD simulations using LAMMPS [84].

The simulations were carried out in the isobaric-isothermal (NpT) ensemble to relax the possible strain associated with the incommensurability of the ordered microphases formed with the simulation box. The system was, then, evolved for 10×10^6 MD steps for equilibration and for 2×10^6 steps for averaging with a time step, $dt = 0.005$. We used the Nose-Hoover thermostat and barostat with the recommended relaxation times, $100dt$ and $1000dt$, respectively. We simulated systems with pressures (p) between 0.01 and 0.55 and temperatures (T) between 0.10 and 1.0.

We perform two studies on the system, the first one at constant pressure and the second one at constant volume. In the first study, we choose three isobars for which the periodic microphases are stable at low temperatures, then we start from a fluid phase and gradually cool the system down far beyond the phase transition temperature. From these simulations at constant pressure, we calculate thermodynamic properties such as the enthalpy per particle and local order parameters to characterise the structure of the microphases at the particle-particle scale. We also identified clusters by performing a cluster analysis [80], in which two particles are considered to be linked in the same cluster if the distance between them is lower than $r_{cut} = 1.6$, i. e. the distance to the first minimum in the pair correlation function. Intending to determine the lattice structure of the cluster-crystal, we computed the cluster-cluster pair correlation function using the centres of mass of the clusters. As in Chapter 4, we calculate the BOOD using again the centres of mass of the clusters.

In the second study, we choose three isochores and again cool the system down beyond the phase transition temperature. We obtain these results from (NVT) simulations, using the same time step and relaxation time for the thermostat as specified above. Dynamic (the mean squared displacement (MSD), the coherent and incoherent scattering functions) and structural (pair distribution function and static structure factor) properties were calculated from these constant volume simulations. Typically, these NVT simulations consisted of 10^6 MD steps for equilibration, followed by another 10^6 steps for taking averages.

5.2.1 Phase behaviour and equilibrium properties

In this section, we study the equilibrium properties of the model system to characterise the phase or structural transitions that the colloidal fluid undergoes. The qualitative phase diagram obtained from NpT MD simulations is shown in Figure 5.2. For the set of parameters that we have chosen, the cluster-crystal, the hexagonal and the lamellar phases spontaneously form at low temperatures. Local density plots of such ordered microphases are shown in the bottom panel of Figure 5.2.

The local density profiles were calculated by averaging 10000 independent equilibrium configurations. At low densities ($\langle\rho\rangle \lessapprox 0.15$), the colloidal fluid assembles into a cluster-fluid phase, which turns into a cluster-crystal at low temperatures. At intermediate densities ($0.22 \leq \langle\rho\rangle \leq 0.32$), a percolating fluid is observed at high temperatures, becoming a hexagonal phase after decreasing the temperature below $T \approx 0.35$. At higher densities ($\langle\rho\rangle \gtrapprox 0.35$), a percolating fluid is formed, which, upon decreasing the temperature, turns into the lamellar phase. To determine whether a percolating fluid is formed or not, we use a percolation algorithm, based on the references [128, 23], that looks for infinite clusters. The criterion to consider a system as a percolating fluid is that a hundred per cent of 1000 independent equilibrium configurations analysed have at least one percolating cluster. Two structural parameters characterise the ordered microphases: l_0, which is the lattice constant (centre-to-centre separation distance between the clusters), and d_0, which is the size of the clusters

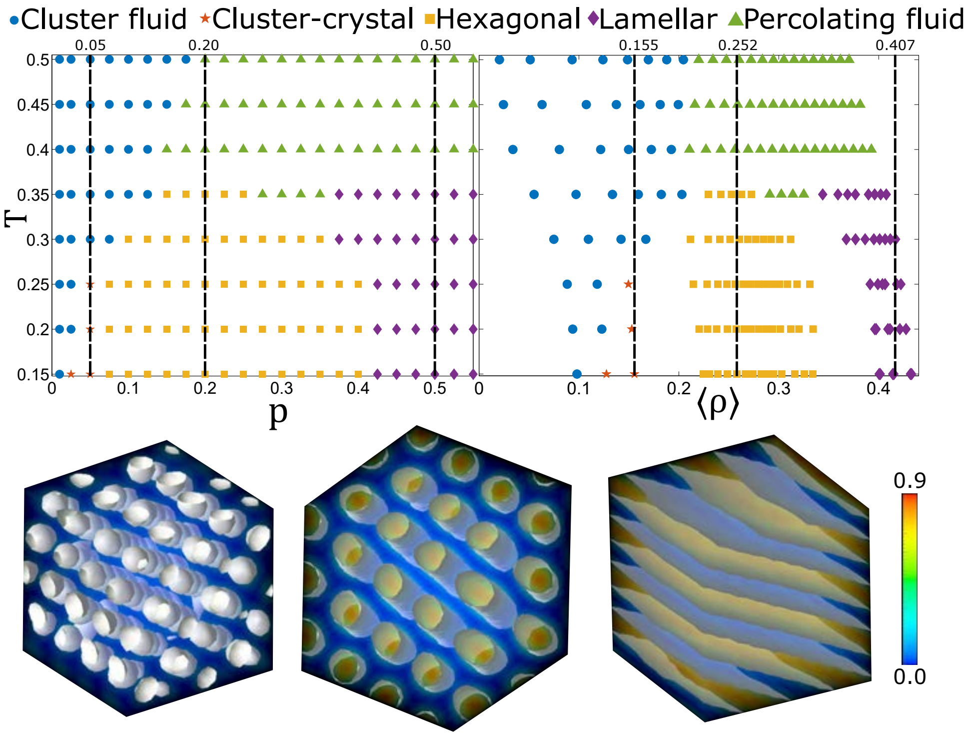

Figure 5.2: Top panel: structural phase diagrams in the planes Tp (left) and $T\rho$ (right). We choose three isobars and three isochores to analyse the system, they are depicted as vertical dashed lines. Bottom panel: local density plots of representative ordered phases, the iso-density surfaces in gray correspond to $\rho_{iso} = 0.30$. The cluster-crystal phase (left) was obtained for $T = 0.20$, $p = 0.050$, with $\langle\rho\rangle = 0.153$, the hexagonal phase (centre) for $T = 0.30$, $p = 0.175$, with $\langle\rho\rangle = 0.251$ and the lamellar phase (right) for $T = 0.30$, $p = 0.425$ with $\langle\rho\rangle = 0.385$.

(diameter in case of cluster-crystal and hexagonal phases, and width in case of lamellar phase). We estimate such distances from iso-density surfaces with $\rho_{iso} = 0.30$, at temperatures at which the ordered microphases are stable. For the cluster-crystal phase, $l_0 = 5.63\sigma$ and $d_0 = 3.27\sigma$, for the hexagonal $l_0 = 5.57\sigma$ and $l_0 = 2.75\sigma$, and for the lamellar $l_0 = 4.80\sigma$ and $d_0 = 2.28\sigma$. These quantities vary slightly with temperature within the region of stability; thus, we can consider them approximately constant.

Regarding the lattice structure of the cluster-crystal, the pair correlation function and BOOD calculated from a simulation with $N = 1991$ (i. e. with a box edge length $L = 23.42$) exhibit a behaviour intermediate between that expected for the FCC and the BCC lattices. We attribute this behaviour to finite size effects that persist up to very large system sizes due to the commensurability of the lattices with only certain box sizes. To clarify this, we performed additional NpT simulations (at $T = 0.20$ and $p = 0.05$) using numbers of particles compatible with the formation of the FCC or the BCC lattices in a cubic box. We found that the colloidal fluid self-assembles into a BCC cluster-crystal when the system size is chosen compatible with this lattice, whereas system sizes compatible with the FCC lattice always lead to the formation of defective crystals. The cluster-cluster pair correlation function and BOOD obtained from simulations with $N = 1200$ are shown in Figure 5.3.

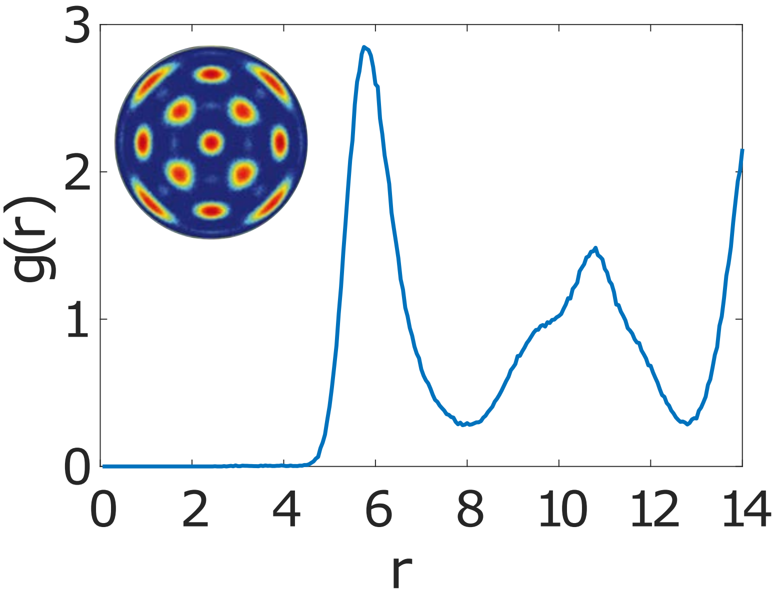

Figure 5.3: Pair correlation function, $g(r)$, and bond-orientational order diagram (BOOD) measured using the centres of mass of the clusters in the cluster-crystal obtained at $p = 0.05$ and $T = 0.2$. These $g(r)$ and BOOD are compatible with the BCC crystal lattice.

The BOOD shows the typical pattern of the BCC lattice [109]. Although a more rigorous study is needed to unambiguously determine which one is the most stable cluster-crystal at these conditions, the present results indicate that for the LJY model we are considering, the BCC is likely more stable than the FCC crystal. In studies on the HSDY potential, theoretical approaches predict the stability of the BCC cluster-crystal [17, 15]. However, the hexagonal-close packed (HCP) cluster-crystal, almost degenerate with the FCC cluster-crystal, can also be stable at low temperature for the HSDY potential. As for the SWL considered in [24], the FCC cluster-crystal was found to be the stable phase. These differences in the symmetry of the cluster-crystal phase might be related to differences in the steepness of the effective repulsion in SALR models.

Even though we have already mentioned that the LJY model here considered and the SWL model studied in reference [24] cannot be directly compared, another worth mentioning difference between them both is that the cluster-crystal forms more easily from the fluid phase for the LJY than for the SWL model. For the LJY potential, we have quickly obtained the cluster-crystal from NpT

MD simulations at the appropriate thermodynamic conditions, but also from grand canonical MC simulations performed with a bespoke code. However, using the same MC code, we never obtained the cluster-crystal in the SWL potential. This is surprising since the periodic microphases are stable up to higher temperatures for the SWL potential from reference [25] than for the LJY model here considered. Possibly, this is related to the reduced attraction when the flat minimum of the SWL is replaced by the sharp minimum of the LJY model.

The only phase that is often predicted by theory and simulations in systems with competing interactions that we did not find in our simulations is the gyroid phase [24, 15]. We conducted a preliminary study in which we sweep temperatures and densities in the ranges $T = 0.30 - 0.20$ with $\Delta T = 0.01$ increments and $\rho = 0.290 - 0.370$ whit $\Delta\rho = 0.001$ increments. We partially identified ordered structures reminiscent of the gyroid phase at $\rho \approx 0.325 - 0.335$ and $T = 0.25 - 0.30$, which suggests that this phase might also be stable for the LJY model. Nevertheless, this question is beyond the scope of this Chapter.

The phases obtained are further analysed by computing the pair correlation function, $g(r)$, and the static structure factor (SSF),

$$S(\boldsymbol{q}) = \left\langle \frac{1}{N} \sum_{i,j=1}^{N} \exp\left(i\boldsymbol{q} \cdot (\boldsymbol{r}_i - \boldsymbol{r}_j)\right) \right\rangle, \tag{5.2}$$

where $\mathbf{q} = (2\pi/L)(n_x, n_y, n_z)$, with n_x, n_y and n_z integers, is the wave-vector. The SFF is often used to identify microphase separation because the aggregation process leads to the appearance of a low-q peak arising from the nearest neighbour clusters, at q's lower than the medium-q peak coming from nearest neighbour particles. The dependence of the $g(r)$ and the SSF with temperature along three isochores of which the periodic microphases spontaneously from at low temperature is presented in Figure 5.4 (these isochores are marked as vertical lines on the phase diagram sketched in the right panel of Figure 5.2). The peaks of the $g(r)$ become increasingly more pronounced at low temperatures, indicating the ordering of the colloidal fluid. This is clearly observed for the first peak (located at a distance $r \approx 1.2\sigma$), but also at long distances. The $g(r)$ of the lamellar phase exhibits particularly pronounced maxima and minima at low temperatures, which is consistent with the freezing of the lamellae. The presence of a low-q peak in the SFF up to $T = 0.5$ signals the tendency of the particles to aggregate. This peak becomes sharper for $T \leq 0.4$. The second peak in the SFF, corresponding to nearest neighbour particles, shifts to higher values of q as temperature decreases at the three considered densities. This reflects that the nearest neighbour particles get better packed as the temperature decreases.

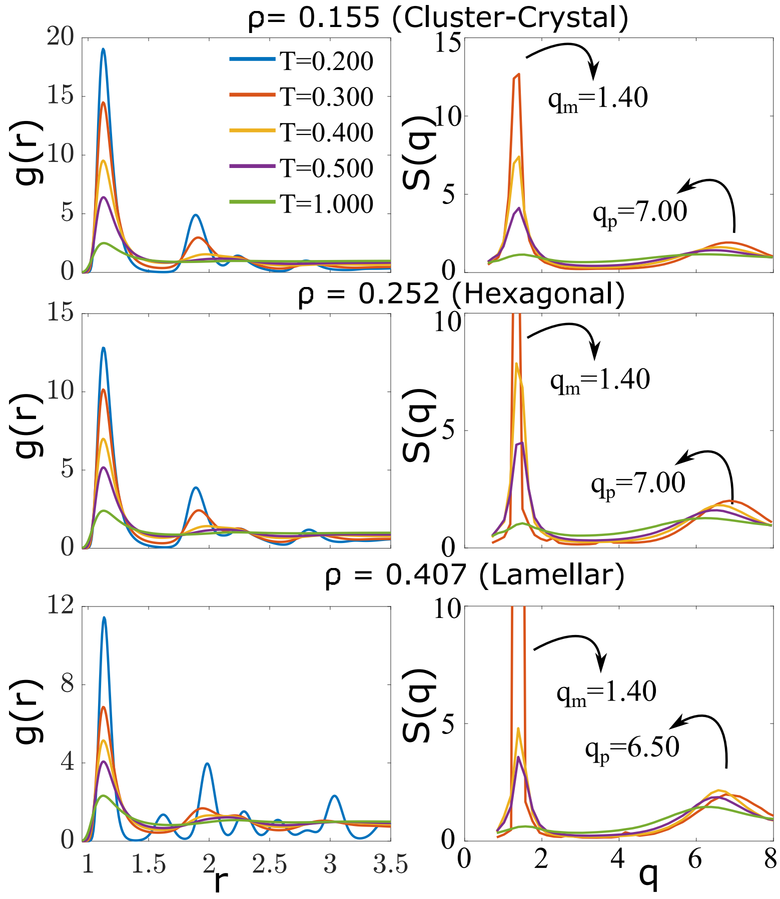

Figure 5.4: Pair distribution function, $g(r)$, and static structure factor, $S(q)$, as functions of temperature along three isochores at which the periodic microphases form spontaneously at low temperatures. Densities and their corresponding microphases are indicated in the figure. The wave-vectors corresponding to the first and second peaks in $S(q)$ emerging from correlations between nearest clusters (q_m) and between nearest particles (q_p) are marked. The coherent and incoherent intermediate scattering functions were evaluated at these wave-vectors (See Figure 5.10)

With the aim of obtaining a more detailed picture of the thermodynamic and structural transitions that the colloidal fluid undergoes with temperature, we performed additional simulations along the three isobars marked with vertical lines in the phase diagram outlined in the left panel of the Figure 5.2. Heating and cooling runs were performed in a temperature range spanning from high temperatures at which the colloidal fluid forms clusters but remains disordered ($T = 0.5$) to low temperatures at which the periodic microphases are stable ($T = 0.24$). Besides calculating the average internal energy ($\langle U\rangle/N$) and density ($\langle\rho\rangle$), the enthalpy ($\langle H\rangle/N = \langle U\rangle/N + p/\langle\rho\rangle$) was also calculated.

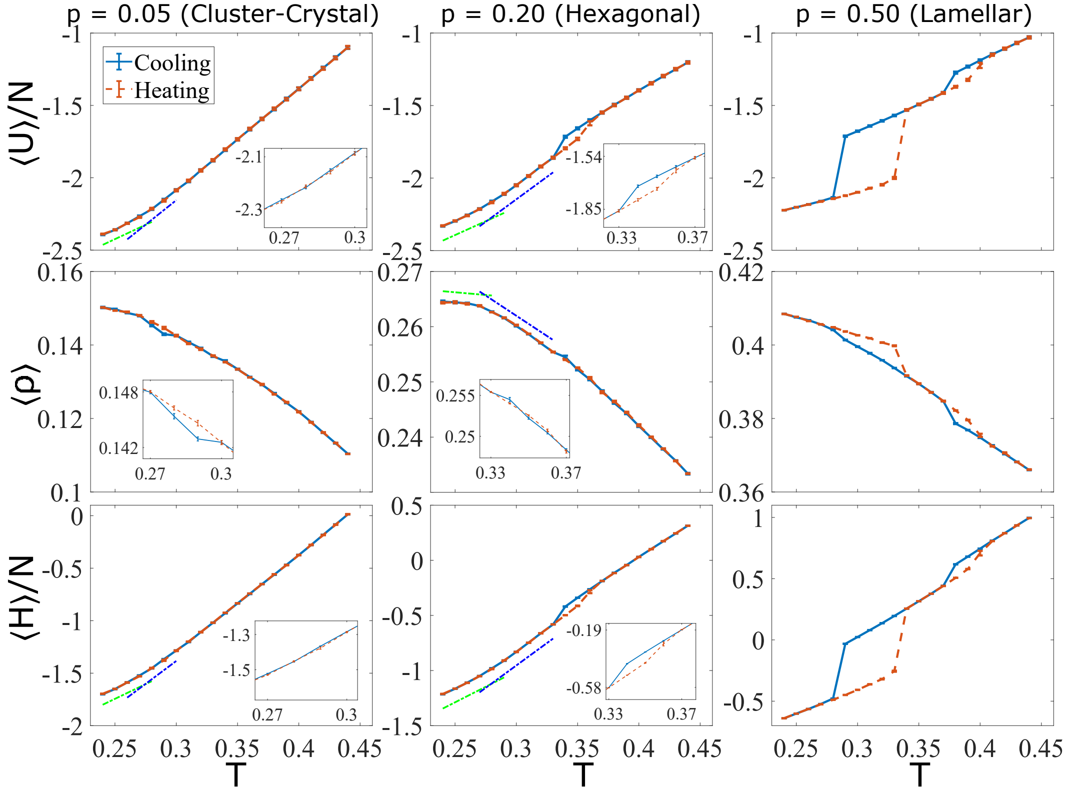

Figure 5.5: Thermodynamic data obtained from heating and cooling runs in the NpT ensemble for the cluster-crystal ($p = 0.05$), hexagonal ($p = 0.25$) and lamellar ($p = 0.50$) phases. The top row panels show the internal energy (U/N), the central panels the density (ρ), and the bottom panels the enthalpy (H/N). The blue and green dashed lines are guides to better visualize the changes of slope.

At high pressure ($p = 0.5$), for which the lamellar phase forms at low temperature, the enthalpy shows two discontinuities with their corresponding hysteresis loops (See Figure 5.5). This means that the system undergoes two first-order phase transitions: one at $T = 0.37 - 0.41$ from the percolating fluid to a liquid lamellar phase (particles in the lamellae behave like liquid), and a second transition at $T = 0.28 - 0.34$ from liquid to crystalline lamellae (particles in the lamellae behave like solid). Visual inspection of configurations at temperatures above ($T = 0.32$) and below ($T = 0.20$) the latter transition shows that in both cases the colloidal particles self-assemble into lamellae, the difference being that lamellae become crystalline at the lower temperature (see Figure 5.6).

A useful tool that might give us more information on the structure of the lamellae, and thus help us to confirm that this first-order transition corresponds to the internal freezing of the lamellae, is the Lechner and Dellago bond order parameter, $\bar{q}_6$ [129]. This order parameter has been used in bulk systems to distinguish particles in a liquid environment from particles in compact solid environments

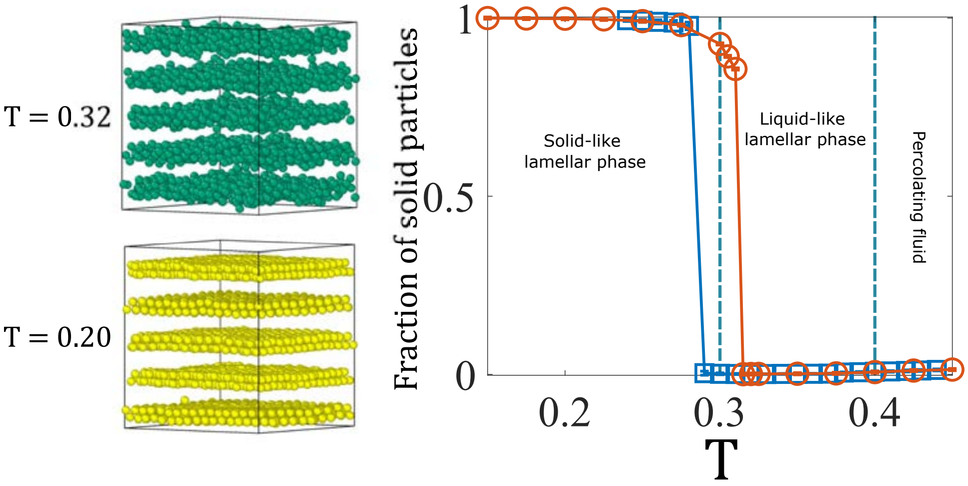

Figure 5.6: Left panel: equilibrium configurations of the liquid-like ($T = 0.32$, top) and solid-like ($T = 0.20$, bottom) lamellar phase for $p = 0.50$. Particles with hexagonal symmetry are coloured in yellow, and particles with no symmetry in green. Right panel: the average fraction of particles with hexagonal symmetry as a function of the temperature. The structure of the colloidal fluid in each region is indicated. The simulations were carried out in the NpT ensemble, and 20 independent configurations were used at each temperature to evaluate the average fraction of solid particles.

(FCC and HCP). As presented in Figure 5.6, lamellae consist of a stack of two hexagonally-packed layers with few small islands on each surface of the lamellae. Even in this situation, the order parameter $\bar{q}_6$ distinguishes liquid-like from solid-like environments. We use $r_{cut} = 1.40\sigma$ to define the first coordination shell and $\bar{q}_{6,limit} = 0.43$ as the threshold that separate particles with liquid-like from those with solid-like environments. The probability of finding particles in solid local environments as a function of temperature along the isobar $p = 0.50$ is shown in Figure 5.6. The curves of the fraction of solid-like particles in the lamellae exhibit a hysteresis cycle. In the heating run, this function adopts values close to one at very low temperature, decreases slowly as the temperature increases, and then at $T = 0.315$, it exhibits a sudden drop to values close to zero, proving that lamellae are crystalline below this temperature and liquid above it.

Continuing with the hexagonal phase, we observe that the enthalpy exhibits a discontinuity with an associated hysteresis loop at $0.33 < T < 0.37$, followed by a subtle change of slope at $T = 0.28$ (See Figure 5.5). In this case, the discontinuity in the enthalpy comes mainly from the energy, as density only shows a small jump along this transition. We attribute this discontinuity to the transition from the percolating fluid to the hexagonal phase. Moreover, we observe a change of slope at lower temperatures ($T \approx 0.27$), which is visible in both the energy and the density and might be related to the internal ordering of the cylindrical clusters. In fact, for $T < 0.27$ the

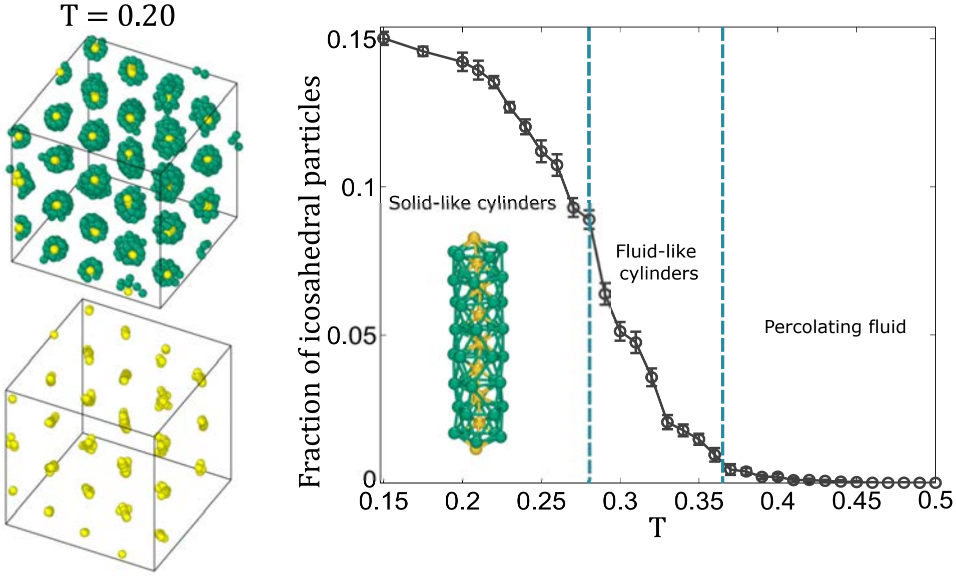

Figure 5.7: Left panel: equilibrium configuration of the hexagonal phase at $p = 0.20$, the particles with icosahedral neighbouring are coloured in yellow and the surface particles in green. Right panel: the average fraction of solid-like particles with icosahedral symmetry. The structure of the colloidal fluid in each region is indicated. The simulations were carried out in the NpT ensemble, and 20 independent configurations were used at each temperature to evaluate the average fraction of solid particles.

cylinders adopt a very ordered internal configurations can be seen in Figure 5.7. The structure of the cylindrical clusters with temperature was monitored by performing a common neighbour analysis (CNA) [130], taking a fixed cut-off radius of 1.6σ to consider that two particles are nearest neighbours. This analysis allows us to distinguish nearly perfect local icosahedral environments from disordered ones. The CNA was performed with OVITO visualisation tool [97]. For each temperature along the isobar $p = 0.20$, the fraction of particles with icosahedral symmetry was estimated by averaging the CNA results for 20 independent configurations. As can be seen in the right panel of Figure 5.7, at low temperature, about 15% of particles have an icosahedral environment. Note that it actually corresponds to 75% of the particles being solid-like, since in a perfect pentagonal tube of interpenetrated icosahedra only 20% of the particles, those at the core, have icosahedral environments, whereas those that are on the surface are not identified as icosahedral with the CNA due to the missing bonds. The solid-like cylindrical clusters are a succession of interpenetrated icosahedra, forming a spiral structure, similar to the Bernal spiral [37]. The Bernal spiral consists of three strands of particles forming a structure of face sharing tetrahedra, in which each particle has six neighbours. The Bernal spiral has been extensively reported in colloidal systems with competing interactions both in experiments[42, 49] and in simulations [23, 36, 118]. As temperature increases, the average fraction of particles with an icosahedral environment decreases gradually and adopts values close to zero at high temperature (i. e., above the transition from the hexagonal phase to the percolating fluid, at $T = 0.36$). Interestingly, the faster change of slope of the fraction of icosahedral particles occurs at exactly the same temperature (T = 0.28) at which a small change of slope is observed in the enthalpy (See Figure 5.5).

Finally, at low pressure ($p = 0.05$), for which the cluster-crystal phase is stable at low temperatures, the enthalpy does not exhibit any discontinuity, neither in heating nor in cooling runs. Only a small change in the slope is observed at $T \approx 0.27$. However, whereas the average energy remains continuous, the density does show a mild discontinuity with an associated hysteresis loop in the neighbourhood of the change of slope in the enthalpy ($0.27 < T < 0.30$). This hysteresis loop should also be observed in the enthalpy, but as the pressure is relatively low, the energy is the dominant contribution to the enthalpy and the hysteresis loop is not visible. This means that the phase transition from the cluster-fluid to the crystal-cluster, which can be classified as a first-order due to the presence of hysteresis in the density, is mainly driven by the rearrangement of the fluid, at both cluster-cluster and particle-particle scales, leading to better packing.

We also analysed the internal ordering of the clusters along the isobar $p = 0.05$ using the CNA again. The average fraction of particles with icosahedral symmetry and the cluster size distribution at different temperatures are shown in Figure 5.8. The cluster size distributions for $T < 0.25$ takes the maximum values for sizes between $n = 19$ and $n = 25$. These clusters often adopt non-spherical configurations, and their shapes can be described as interpenetrated icosahedra (See Figure 5.8). In particular, for $n = 19$ the structure consists of two interpenetrated icosahedra sharing a five-fold axis so that the two core particles have icosahedral symmetry. Interestingly, these geometries correspond to putative global minima of clusters in which interactions between particles are described by Lennard-Jones and other simple models [131, 132], suggesting that the enhanced probability found for these sizes might be related to their higher energetic stability. The average fraction of particles with icosahedral symmetry adopts values slightly above 10% at low temperature, which means that nearly all the particles belong to ordered clusters (about 10%, 13% and 15% of particles with $n = 19$, $n = 23$ and $n = 26$ have local icosahedral environments, respectively). As temperature increases, the fraction of icosahedral particles decays smoothly, reaching a value close to zero at $T > 0.35$, at which the cluster-crystal has already melted into a cluster-fluid. In this case, the transition from the

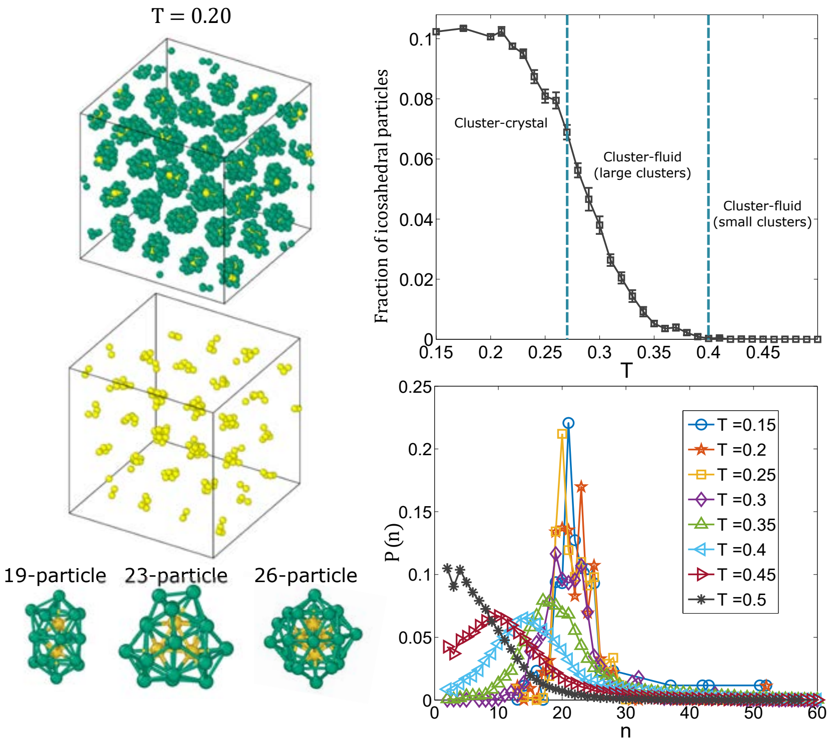

Figure 5.8: Left panel: equilibrium configuration of the cluster-crystal phase at $p = 0.05$, the particles with icosahedral neighbouring are coloured in yellow and the surface particles in green. Right panel: in the upper part, the average fraction of solid-like particles with icosahedral symmetry as a function of temperature; in the lower part, the cluster size distribution for different temperatures. The structure of the colloidal fluid in each region is indicated. The simulations were carried out in the NpT ensemble, and 20 independent configurations were used at each temperature to evaluate the average fraction of particles with icosahedral environments.

cluster-fluid to the cluster-crystal occurs at similar temperatures as the internal ordering of clusters.

The internal ordering of the modulated phases formed by colloids with competing interactions has already been reported in previous experimental[47], and simulation [36, 118, 133, 119] studies. However, simulations of the SWL model at temperatures well below the temperature at which the periodic microphases become thermodinamically stable did not show evidence of such ordering at the particle scale [25]. This suggests that the internal ordering of the periodic microphases might be a common feature of colloidal systems interacting via a potential with a sharp minimum in the short-attractive range, in contrast to the flat minimum in the SWL model, at least at moderate temperatures.

So far, we have observed that at low enough temperature, the ordered microphases experience an internal ordering within the clusters. The growth of internal ordering is steep and discontinuous in the lamellar phase (See Figure 5.6). In the hexagonal phase, the internal ordering is smoother, still pronounced, but it seems to be continuous (See Figure 5.7). Regarding the cluster-crystal phase, its behaviour is different from the other two ordered microphases, since once the conditions to stabilise the phase are reached, the conforming clusters adopt a solid-like structure with no need of further cooling, i.e. the internal ordering occurs at the cluster-cluster and particle-particle scales roughly at the same time.

We propose a correlation between the clusters dimensions and the characteristics of the internal ordering. In zero-dimensional clusters (cluster-crystal phase), the stabilisation of the ordered phase is accompanied by local intra-cluster ordering. In one-dimensional clusters (hexagonal phase), the internal ordering is steep but continuous and occurs gradually as the temperature decreases. Finally, in two-dimensional clusters (lamellar phase), such internal ordering occurs steeply and with a large discontinuity. In the last decades, there has been plenty of interest in colloidal crystals. Since the seminal articles on two-dimensional colloidal crystals in the decade of 1980 by Pieranski [134, 135], this type of ordered structures has been used in nanofabrication with applications in lithography [136] and templating [137] among others.

5.2.2 Dynamic properties

With the model system already characterised from structural and thermodynamic points of view, we study the dynamics. We use different properties to characterise the dynamics of the system, such as the mean-squared displacement (MSD) and the coherent and incoherent scattering functions. These analyses are performed along the three isochores previously studied and marked in the right panel of Figure 5.2. The colloidal fluid is systematically cooled down from high temperatures at which disordered phases are stable for each density.

Let us start with the MSD, which provides information of the single-particle dynamics. It can be written as:

$$\left\langle \Delta r(t)^2 \right\rangle = \left\langle \frac{1}{N} \sum_{i=1}^{N} \left(\boldsymbol{r}_i(t) - \boldsymbol{r}_i(0) \right) \right\rangle, \tag{5.3}$$

The evolution of the MSD with the temperature is shown in Figure 5.9.In the three cases, at high temperatures, the fluid reaches the diffusive regime at long times and, as temperature decreases, the movement of the particles slows down. Nevertheless, the temperature at which this slowing down occurs depends on the density.

At low densities ($\rho = 0.155$), corresponding to the cluster-crystal, the MSD reaches the diffusive regime at long times for $T \geq 0.30$, and becomes sub-diffusive below $T = 0.275$ (Figure 5.9, left panel). This temperature coincides fairly well with that at which the enthalpy ($T \approx 0.27$) exhibits a small discontinuity that signals the transition from the cluster-fluid to the cluster-crystal. At $T = 0.20$, the MSD remains low for the whole duration of the simulation, with a behaviour that is reminiscent of a solid. At this low temperature, the particle movement occurs mainly via vibrational and rotational moves of the clusters about the lattice positions of the cluster-crystal, and to a lesser extent to exchange of particles between the clusters are severely hindered. This can be seen from movies made out of instantaneous configurations of the particles. At this low density, the MSD exhibits three different regimes at short, intermediate and long times. After the initial ballistic movement at short times, the movement of the particles moderately slows down at distances of the order of the typical bond length, $d_{min}/\sigma = 2^{1/6} - 1 = 0.12$, followed by another deceleration at intermediate time and distances comparable to the cluster size $d_{clust}/\sigma = d_0/\sigma - 1 \approx 2.27$ (taking the value of d_0 provided in the previous section). Beyond this distance, the movement of the particles enters the diffusive or sub-diffusive regimes depending on the temperature, as explained above.

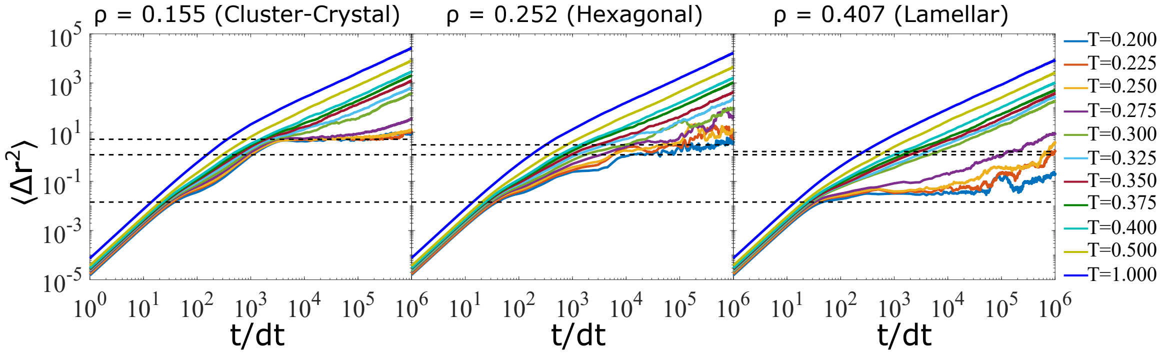

Figure 5.9: The mean squared displacement as a function of temperature at low ($\rho = 0.155$, left panel), intermediate ($\rho = 0.252$, central panel) and high ($\rho = 0.407$, right panel) densities. These densities stabilise, respectively, the cluster-crystal, the hexagonal and the lamellar phases at low temperature. From bottom to top, the horizontal dashed lines mark the MSD compatible with the distance of the minimum in energy $d_{min}/\sigma = 2^{1/6} - 1 = 0.12$, with the maximum bond distance $d_{max}/\sigma = 2.1 - 1 = 1.1$, and with the average cluster size $d_{clust}/\sigma = d_0 - 1$ in each periodic microphase. In the cluster-crystal and hexagonal phases, the MSD exhibits two changes of slope at these distances d_{min} and d_{clust}, but in the lamellar phase only a change of slope coincident with d_{min} is clearly seen.

This picture is compatible with a scenario in which particles first rattle around their positions (short times), then move within the clusters by single particle displacements or by vibrations and rotations of the clusters (intermediate times), and finally travel long distances by jumping to neighbour clusters and by translations of the clusters as a whole (long times). This behaviour is similar to that reported by Fernandez Toledano *et. al.* [122] in a study of the LJY model but with a different set of parameters so that the attractive range is much shorter than that of the model considered here. In this model with a shorter range attraction, the second change of slope occurs at the maximum bond distance d_{max}, but in our system it correlates better with the size of the clusters (see Figure 5.9).

At intermediate density ($\rho = 0.252$), corresponding to the hexagonal phase (Figure 5.9, central panel), the MSD reaches the diffusive regime at long times at $T \geq 0.325$ and gradually becomes sub-diffusive below this temperature. This threshold temperature is below the transition from the percolating fluid to the hexagonal phase (that occurs at $0.33 < T < 0.37$ as revealed by the hysteresis loop in the enthalpy curve). This suggests that the particles diffusion mechanisms are probably not so different in the percolating fluid and in the hexagonal phase at temperatures just below the transition. This behaviour is completely different from that observed in the cluster-crystal, in which the movement of the particles at long times starts to be sub-diffusive exactly at the transition from the cluster-fluid to the cluster-crystal. We attribute this different behaviour to the fact that the particles in the cluster-crystal can only travel long distances either by migrating to other clusters or by large translational moves of the clusters as a whole. These two types of movements are largely impeded at low temperatures in the cluster-crystal. However, in the hexagonal phase, particles might still move long distances by displacements along the axial direction of the cylinders. Note that the long-time MSD exhibits large departures from the diffusive behaviour at temperatures starting at $T = 0.30$ and especially below $T = 0.275$, indicating that the particle movement is further impeded below this temperature coincident with the transition to solid-like cylindrical clusters at $T = 0.28$. At short and intermediate times, three different regions are again observed in the MSD at $\rho = 0.252$. There is an initial slowing down of the movement of the particles at distances similar to the average bond length d_{min}/σ, followed by a second slowing down at distances comparable to the cylinder diameter $d_{clust}/\sigma = d_0/\sigma - 1 = 1.75$ (taking the value of d_0=2.75 reported in the previous section). Displacements larger than the diameter of the cylinder can only be achieved either by particle displacements along the axial direction of the cylindrical aggregates or by particle jumps between neighbouring clusters.

Finally, at high density ($\rho = 0.407$), at which the lamellar phase forms at low temperature (Figure 5.9, right panel), the movement of the particles at long times is diffusive at $T \geq 0.30$ and sub-diffusive below this temperature. This change in the dynamic behaviour occurs at the same temperature at which the freezing of the lamellae takes place ($0.28 \leq T \leq 0.34$). Note that the MSD at $T = 0.30$ was obtained in a simulation from the cooling branch of the hysteresis loop. At lower temperatures, the diffusion of the particles is reduced, behaving like a solid. As for the behaviour at short and intermediate times, the MSD exhibits only one slowing down at the typical bond distance (d_{min}/σ). The second slowing down observed at distances compatible with the cluster size for the cluster-crystal and hexagonal phases is not significant for the lamellar phase. As the lamellae are infinite in two dimensions of space, the width of the lamellae does not pose a strong constrain on the displacements of the particles.

It is essential to mention that the MSD was measured using a configuration in which lamellae are oriented along the diagonal of the simulation box. Curiously, when the lamellae are oriented parallel to one of the sides of the simulation box, lamellae can slide with respect to the adjacent lamellae at temperatures below the freezing transition when their surface becomes smooth, entailing large MSD at low temperatures. We have characterised such a curious effect by calculating the MSD of the lamellae and the MSD of the particles within the lamellae, concluding that the source of the phenomenon is the collective movement of the lamellae, whereas the particles within them behave as in solid. The quantification of the drift magnitude is difficult to achieve since it might be affected by finite size effects, the simplification of the effective pair-potential and the neglect of the hydrodynamic interactions. Thus, all the analysis was performed over the configuration in which the lamellae are oriented along the diagonal, in which collective movement is prevented because all the lamellae are connected by the periodicity imposed in the simulations. However, there are many examples in the literature in which floating or sliding non-interacting sheets and hexagonal phases have been found, such as S-layer proteins [138], CdTe nanocrystals [139], nanosheets of diblock copolymers [140], the columnar phase formed by DNA-cationic-lipid complexes [141], or inverse patchy colloids [142, 143].

Now, we analyse the time evolution of the spatial correlations for the collective movement, using the coherent (or total) intermediate scattering function,

$$F(q,t) = \left\langle \frac{1}{NS(q)} \sum_{i,j=1}^{N} \exp\left(-i\boldsymbol{q} \cdot (\boldsymbol{r}_j(t) - \boldsymbol{r}_i(0))\right) \right\rangle, \tag{5.4}$$

that can be measured in the laboratory from light scattering experiments [144]. Correlation between single particle movement can be obtained from the incoherent (or self part) intermediate scattering function,

$$F_s(q,t) = \left\langle \frac{1}{N} \sum_{i=1}^{N} \exp\left(-i\boldsymbol{q} \cdot (\boldsymbol{r}_i(t) - \boldsymbol{r}_i(0))\right) \right\rangle . \tag{5.5}$$

These functions quantify the time correlation at a given length scale and are often used to characterise the structural relaxation of colloidal systems with competing interactions [26, 23, 133, 144]. We evaluate these functions at wave-vectors close to the first (q_m) and second (q_p) peaks that emerge the SSF at intermediate and low temperatures (See Figure 5.4), the first coming from correlations between nearest neighbour clusters and the second from nearest neighbour particles, respectively.

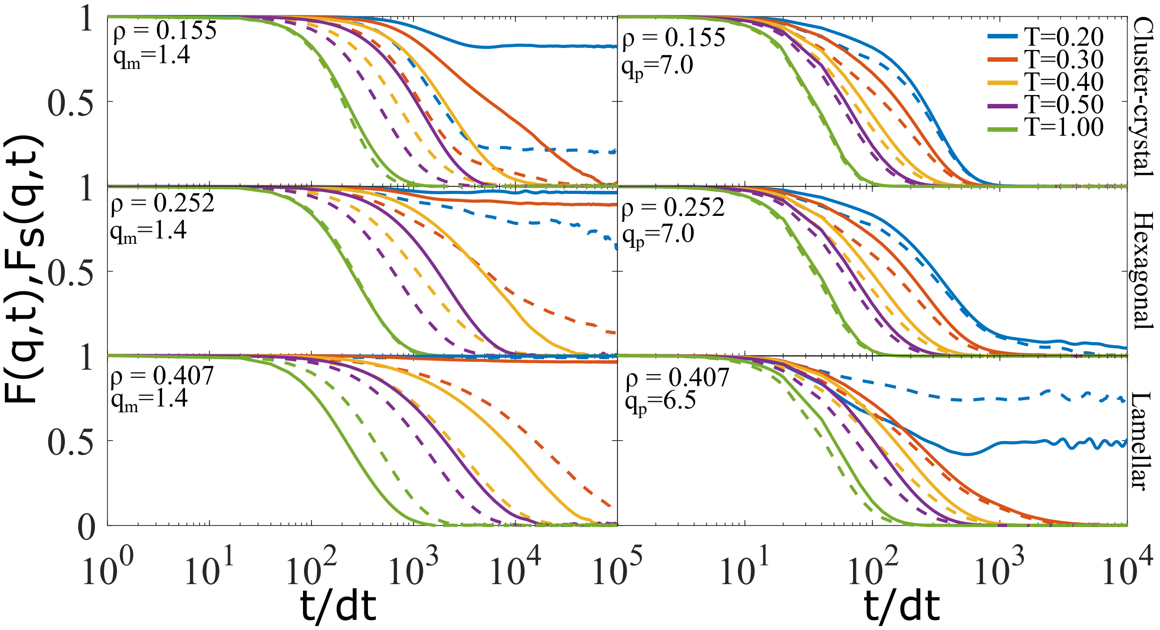

Figure 5.10: Coherent ($F(q,t)$, solid lines) and incoherent ($F_s(q,t)$, dashed lines) intermediate scattering functions for q_m and q_p at different temperatures along three isochores: $\rho = 0.155$ (cluster-crystal), $\rho = 0.252$ (hexagonal phase) and $\rho = 0.407$ (lamellar phase).

The evolution with the temperature of the correlations at the microphase scale (corresponding to the pre-peak at $q_m = 1.40$ for all ordered microphases) is shown in the left panels of Figure 5.10. The first observation is that at $T > 0.40$, both the coherent and incoherent functions exhibit a seemly one-step decay at the three densities considered, going to zero in the timescale of our simulations with similar relaxation times. At $T < 0.30$, the behaviour is markedly different depending on the density. At the lower density ($\rho = 0.155$), both the coherent and incoherent correlations decay to zero at $T = 0.30$, at which the fluid of clusters is the stable phase. Especially in the incoherent correlation function, two decay steps can be identified, which indicates that at least two mechanisms with different relaxation times are involved. At $T = 0.2$, both the coherent and incoherent scattering functions experience a first decay followed by a plateau that survives over the timescale of our simulations. At this low temperature, large translational movements of the clusters are largely impeded, but they experience vibrational and rotational movements about the lattice positions of the cluster-crystal. This is consistent with the fact that the plateau value is significantly higher for the coherent than for the incoherent scattering functions. Note that cluster rotational moves had already been reported in a previous study by Toledano *et. al.* [122]. We speculate that the first decay is associated with these vibrational and orientational moves of the clusters.

At intermediate density ($\rho = 0.252$) and $T < 0.30$, neither the coherent nor the incoherent correlation functions at the microphase scale decay to zero in the timescale of our simulations, indicating that much longer times are needed to achieve a good sampling at these conditions. In particular, we observe that at $T = 0.20$, the difference between the collective and single particle correlations is lower than that in the cluster phase. We speculate that equivalent rotations of the cylinders as those observed in the cluster-crystal are largely impeded in the hexagonal phase due to the periodic boundary conditions. On the other contrary, at high density ($\rho = 0.407$), the incoherent correlations decay to zero at $T = 0.30$, but the collective correlations do not. At $T = 0.20$, large correlations are observed either in the coherent and incoherent correlation functions at the microphase scale.

The evolution with the temperature of the correlations at the particle scale, measured at the second peak in $S(q)$ ($q_p = 7.0$ for the cluster-crystal and hexagonal phases and $q_p = 6.50$ for the lamellar phase) is shown in the right panels of Figure 5.10. In this case, the correlations decay to zero quite rapidly at all temperatures and all densities, except for the lamellar phase at $T = 0.2$.

5.3 Confinement in slit pores

With the characterization of the bulk system done, we proceed to study the system under confinement in narrow slits. The confinement is applied along the z coordinate in the form of two repulsive structureless parallel walls, whereas periodic boundary conditions are used in x and y directions. The parallel confining walls are placed at $\pm W/2$, and thus the centre-centre separation between walls is, W. Particles interact with the walls via a Lennard-Jones model truncated and shifted at the energy minimum:

$$\mathcal{V}_{z_w}(z_{iw}) = \begin{cases} 4\epsilon_w \left[\left(\frac{\sigma_w}{z_{iw}} \right)^{12} - \left(\frac{\sigma_w}{z_{iw}} \right)^{6} \right] + \epsilon_w & : z_{iw} < 2^{1/6}\sigma_w \\ 0 & : z_{iw} \geq 2^{1/6}\sigma_w \end{cases}, \tag{5.6}$$

with $\epsilon_w = 1.0$, $\sigma_w = \sigma = 1.0$, and z_{iw} is the distance from particle i to the pore wall, z_w. Thus, we can express the total energy of the system as,

$$U_{tot} = \sum_{i=1}^{N-1} \sum_{j>i}^{N} u_{SALR}(r_{ij}) + \sum_{i=1}^{N} \left(\mathcal{V}_{W/2}(z_{iw}) + \mathcal{V}_{-W/2}(z_{iw}) \right). \tag{5.7}$$

where $u_{SALR}(r_{ij})$ is given by equation 5.1.

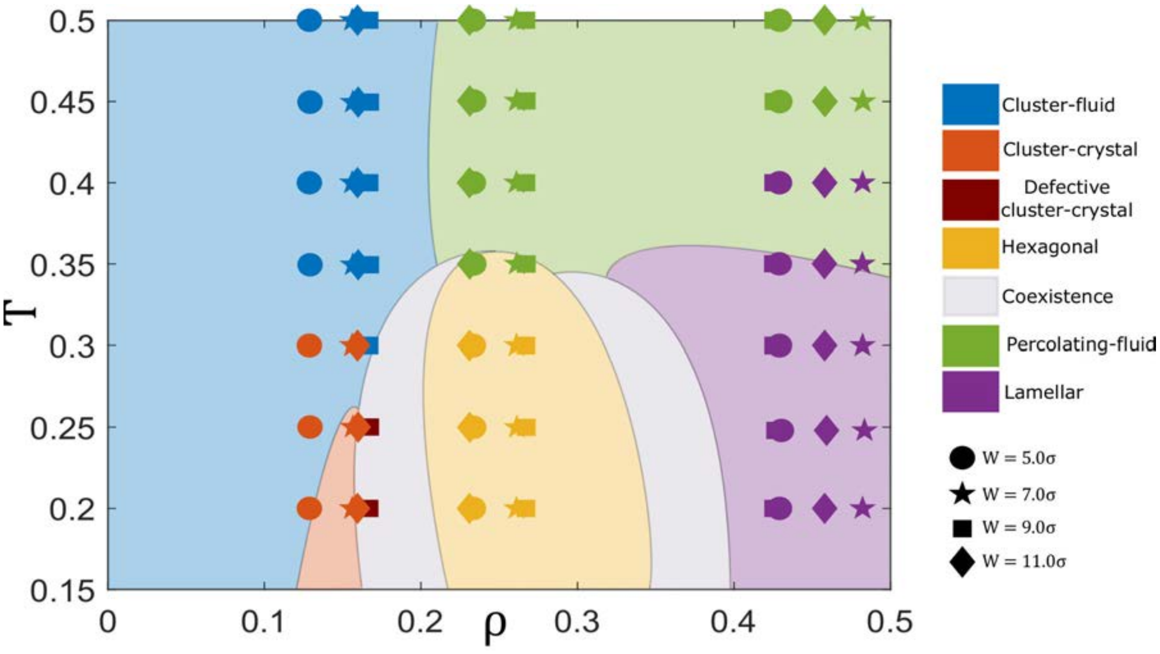

Figure 5.11: Comparison of the phase behaviour between bulk and confined systems. The estimated bulk phase diagram is represented in coloured regions based on Figure 5.2. The colour and marker codes are listed on the right side.

We consider that the slit width is given by the centre-centre separation between the confining walls, W. The particle-wall interaction is purely repulsive. The simulation box dimensions are $L_x = L_y = 40\sigma$, and $L_z = W$, with W being 5.0σ, 7.0σ, 9.0σ and 11.0σ. Thus, the number density is calculated as $\rho = N/L_xL_yW$. With these dimensions in the xy plane, we expect that finite-size effects will not be significant in the periodic directions.

As in the bulk case, we first run GCMC simulations at $T = 0.30$ for a range of chemical potentials ($-1.2 \leq \mu \leq 0.5$) to explore the phase behaviour of the confined systems. We chose three densities corresponding to periodic microphases for each slit width, W. The configurations for which the cluster-crystal, hexagonal and lamellar phases exhibited the most ordered structure (to be compared to that obtained at other chemical potentials) for each slit width were chosen. We study the temperature dependence of the ordered microphases obtained in GCMC simulations by performing MD simulations. The numbers of particles for each system and the chemical potential at which we obtain the initial configurations for the MD simulations are presented in Table 5.1.

Table 5.1: Number of particles adsorbed in the slit pores at which the fluid organizes into ordered structures at $T = 0.3$.

Phase	$W = 5.0\sigma$	$W = 7.0\sigma$	$W = 9.0\sigma$	$W = 11.0\sigma$
Cluster-Crystal	$N = 1030$ $\mu = -1.20$	$N = 1748$ $\mu = -1.00$	$N = 2403$ $\mu = -1.00$	$N = 2807$ $\mu = -1.00$
Hexagonal	$N = 1868$ $\mu = -0.60$	$N = 2923$ $\mu = -0.40$	$N = 3845$ $\mu = -0.40$	$N = 4065$ $\mu = -0.60$
Lamellar	$N = 3432$ $\mu = 0.50$	$N = 5399$ $\mu = 0.20$	$N = 6124$ $\mu = 0.50$	$N = 8058$ $\mu = 0.40$

We perform MD simulations, using LAMMPS [84], in the canonical ensemble (NVT). We use a time step, $dt = 0.005$, and the Nose-Hoover thermostat with a relaxation time of $100dt$. The systems are evolved for 10^6 MD steps for equilibration and for 10^6 MD steps for averaging. We analyse the spatial distribution of the colloidal fluid along the direction perpendicular to the pore walls by calculating the density profiles. We divide the pore volume in small slabs of width δz and then average the number density in each slab:

$$\rho(z) = \frac{\langle N(z + \Delta z)\rangle}{L_x L_y \Delta z} \tag{5.8}$$

Here $\langle N(z + \Delta z)\rangle$ is the ensemble average of the number of particles in the slab between z and $z+\Delta z$. As we did in the bulk system in the previous section, we also investigate the internal ordering of the clusters at the particle scale as the temperature decreases. Again, we use the CNA for the cluster-crystal and hexagonal phases looking for icosahedral environments using OVITO [97](with a cutoff radius of 1.6σ), and the Lechner and Dellago order parameter[129] (with a cutoff radius of 1.4σ) for the lamellar phase, in which the colloidal particles are arranged in stacks of hexagonaly-packed layers within the lamellae at low temperatures. The MSD was also measured using equation 5.3. From the MSD, we extract the diffusion coefficient, D, using Einstein's relation,

$$D = \frac{1}{2d} \lim_{t\to\infty} \frac{\partial \left\langle \Delta r(t)^2 \right\rangle}{\partial t} \tag{5.9}$$

Here d is the dimensionality of the system. We use $d = 2$ for the confined systems since we are focused on narrow slits, and the majority of the displacement occurs in two dimensions. Of course, for the bulk system, we use $d = 3$. This relation only applies at long times when the MSD behaves linearly with time.

This section presents a general comparison between the behaviour in bulk and under confinement in slit pores. Thermodynamic, structural and dynamic aspects will be discussed.

5.3.1 Equilibrium properties

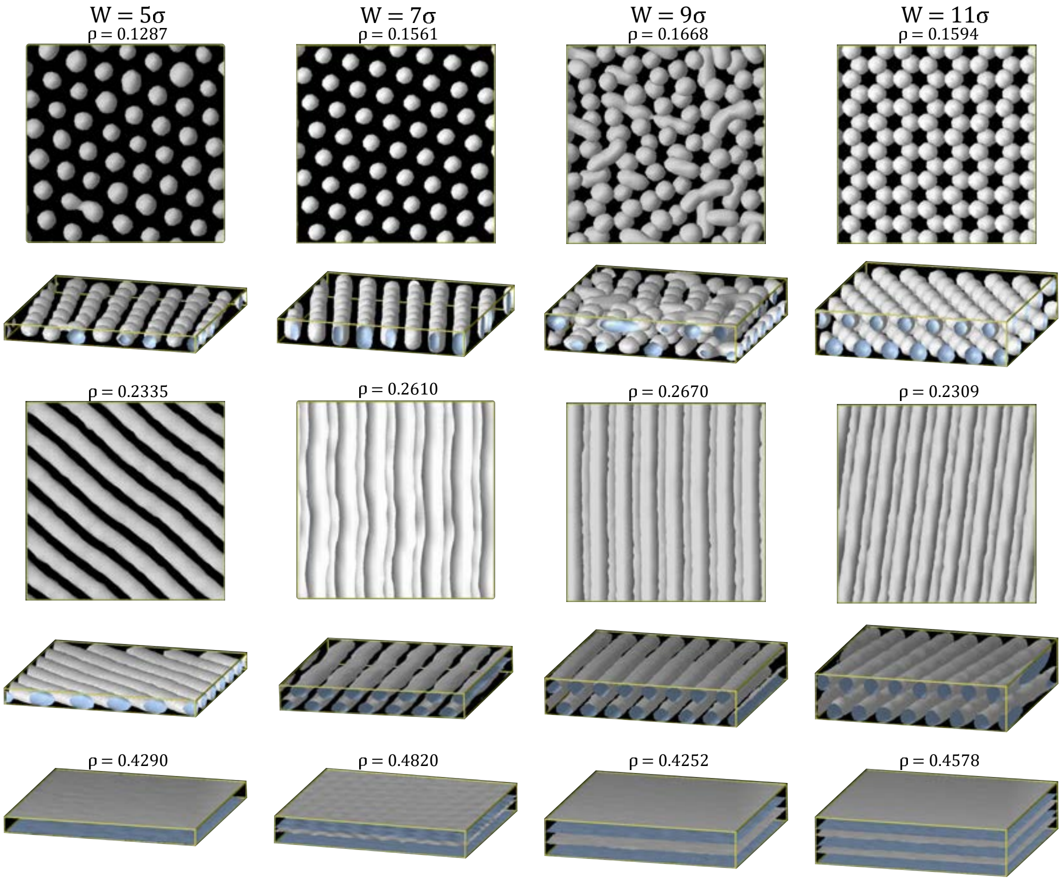

Figure 5.12: Local density isosurfaces at $\rho_{iso} = 0.30$ for all the ordered microphases obtained at different slit widths, W. Two views are presented for the cluster-crystal and hexagonal phases and one for the lamellar phase. Local density maps were calculated by averaging 1000 independent configurations of the systems. The number densities, ρ, are specified and the temperature is $T = 0.30$.

Table 5.2: Estimation of l_0 and d_0 in bulk and confined systems.

	$W = 5.0\sigma$	$W = 7.0\sigma$	$W = 9.0\sigma$	$W = 11.0\sigma$	Bulk
Cluster-Crystal	$l_0 = 5.9(2)\sigma$ $d_0 = 3.3(2)\sigma$	$l_0 = 5.8(1)\sigma$ $d_0 = 3.1(1)\sigma$	$--$ $--$	$l_0 = 6.0(1)\sigma$ $d_0 = 3.3(1)\sigma$	$l_0 = 5.6(1)\sigma$ $d_0 = 3.2(2)\sigma$
Hexagonal	$l_0 = 5.3(1)\sigma$ $d_0 = 3.0(1)\sigma$	$l_0 = 5.5(1)\sigma$ $d_0 = 2.9(2)\sigma$	$l_0 = 5.8(1)\sigma$ $d_0 = 3.2(1)\sigma$	$l_0 = 6.2(3)\sigma$ $d_0 = 2.9(2)\sigma$	$l_0 = 5.6(1)\sigma$ $d_0 = 2.8(1)\sigma$
Lamellar	$--$ $d_0 = 3.4(1)\sigma$	$l_0 = 3.9(1)\sigma$ $d_0 = 2.3(1)\sigma$	$l_0 = 5.5(1)\sigma$ $d_0 = 2.5(1)\sigma$	$l_0 = 4.0(1)\sigma$ $d_0 = 2.0(1)\sigma$	$l_0 = 4.8(2)\sigma$ $d_0 = 2.2(1)\sigma$

Structure of the confined colloidal fluid at low temperature

Figure 5.11 presents the isochores we chose for each W superimposed on the qualitative bulk phase diagram already presented in Figure 5.2. We chose three isochores for each pore width W. They are marked with symbols in the diagram and correspond to densities at which the cluster-crystal, hexagonal and lamellar phases are stable at low temperatures in bulk. Let us first discuss the self-assembled structures at $T = 0.30$. As we explained above, the phase behaviour of the colloidal fluid was studied by performing MC simulations in the grand canonical ensemble along this isotherm. In Figure 5.12, we collect the iso-density surfaces at $\rho = 0.30$. At low densities, ($\rho \approx 0.12 - 0.16$), at which the cluster-crystal is stable in bulk, the colloidal fluid is arranged into one layer of hexagonally-packed spherical aggregates when confined into a narrow pore of $W = 5\sigma$. For a slightly wider pore ($W = 7\sigma$), the fluid still forms one hexagonal layer of clusters, but the clusters are rather elongated, adopting a spherocylindrical shape. These clusters are mainly aligned towards the perpendicular direction to the pore walls. For $W = 9\sigma$, the cluster-crystal was not observed for any value of the chemical potential, meaning that this pore size is incommensurate with the periodicity of the bulk cluster-crystal phase. Instead, the system forms a structure composed of two layers of spherocylindrical clusters, in which a local hexagonal order is still visible. However, the merging between first neighbour clusters belonging to the same layer makes the structure globally disordered. For $W = 11\sigma$, the clusters adopt ordered configurations again, forming a stack of two layers of spherical clusters arranged in a hexagonal lattice.

The diameter of the clusters (d_0) measured from the iso-density surfaces projected on a plane parallel to the pore walls xy as well as the distance (l_0) between nearest neighbour clusters are reported in Table 5.2. For the three pore sizes for which we observed ordered structures, both magnitudes take values close to those of the bulk system at similar thermodynamic conditions, with the maximum deviation from the bulk value being less than 6%. These data allow us to understand why the cluster-crystal becomes incommensurate for a slit width $W = 9\sigma$. This pore size is too wide for the fluid to assemble into a single layer of spherocylinders, since inside a spherocylinder with an approximate height of 7σ, many particles would experience repulsion interactions. Alternatively, the system could form a two-layer cluster-crystal. Taking the values of d_0 and l_0 form the bulk system, two layers of the bulk cluster-crystal can be fitted in a slit pore of width $W \approx d_0 + \sqrt{l_0^2 - (l_0/\sqrt{3})^2} + 2\sigma = d_0 + \sqrt{2/3}l_0 + 2\sigma = 9.9\sigma$, where d_0 is the cluster diameter and $\sqrt{2/3}l_0$ is the distance between two perfect layers of hexagonally-packed clusters with lattice constant l_0. Thus, to accommodate two layers of spherical clusters in the $W = 9\sigma$ pore without incurring in a large energy increase, nearest clusters within the same layer would have to be placed at larger distances to avoid the repulsion between clusters belonging to different layers. A compromise between low energy and efficient packing is achieved by forming a two-layer structure of spherocylindrical aggregates that are oriented parallel to the pore walls to fill the gap between the distant clusters within each layer. When $W = 11\sigma$, two layers of the bulk cluster-crystal can be fitted, leaving some extra room in the pore. In this case, the cluster-crystal phase is expanded to occupy the whole pore volume, as can be seen in the larger values of d_0 and l_0 as compared to the bulk.

At densities at which the hexagonal phase is stable in bulk ($\rho \approx 0.23 - 0.27$), the confined colloidal fluid still self-assembles into cylindrical clusters at the four pore sizes considered, but there are some worth mentioning structural differences depending on the pore size. For $W = 5\sigma$, one layer of cylindrical aggregates with a circular cross-section is formed, meaning that $W = 5\sigma$ is compatible with the diameter of the cylindrical clusters in bulk (see Table 5.2). In this case, the cylinders are aligned with the diagonal of the simulation box to achieve a separation between cylinders similar to that in bulk. For $W = 7\sigma$, two layers of cylindrical clusters are formed, this time approximately aligned with one of the edges of the simulation box. These cylindrical aggregates are deformed with respect to the bulk phase since they adopt a rather ellipsoidal cross-section in contrast to the circular cross-section observed in bulk. This suggests the incommensurability of the pore size with the bulk hexagonal phase. However, the mismatch is not that high to frustrate completely the hexagonal phase. Two layers of the bulk hexagonal phase can fit in a pore of width $W \approx d_0 + \sqrt{3}/2l_0 + 2\sigma = 9.5\sigma$. This value is significantly larger than the slit with $W = 7\sigma$, but the hexagonal phase is still able to survive by deforming the cross-section of the cylinders and adjusting the distance between cylinders. The incommensurability at $W = 7\sigma$ is also reflected on the average energy of the system, which is larger in this confined case ($\langle u \rangle = -1.904$) than in bulk

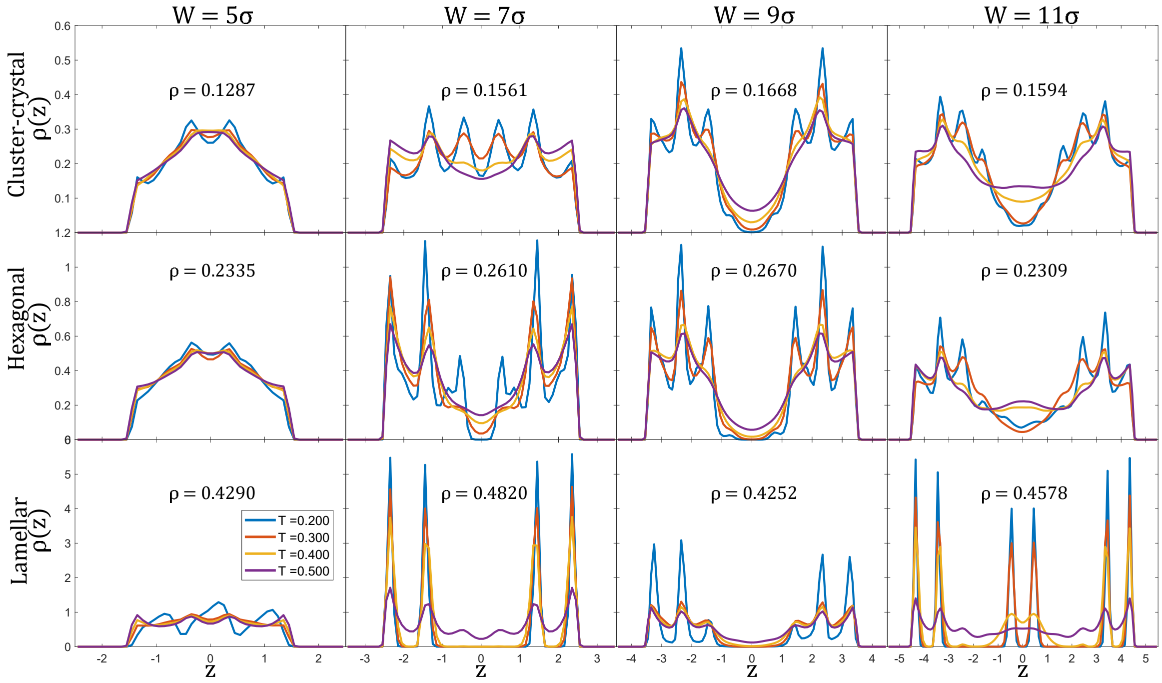

Figure 5.13: Density profiles along z-direction at different temperatures and slit widths.

($\langle u \rangle = -2.065$). Following the same discussion, the pore size $W = 9\sigma$ has a more suitable size to accommodate two layers of cylindrical clusters, so we expect fewer strains in this case. Indeed, our simulations reveal that the colloidal fluid self-assembles into two layers of cylindrical clusters with a nearly circular cross-section as in bulk. Differently, for $W = 11\sigma$, the pore size is wider than needed to host two perfect layers of the bulk hexagonal phase. Thus, the system compensates this issue by forming slightly thicker cylinders and expanding the centre-to-centre distance between adjacent clusters compared to the bulk phase (see Table 5.1).

At high densities ($\rho \approx 0.42 - 4.49$) at which the lamellar phase is stable in bulk, the colloidal particles form the lamellar phase for all the pore considered widths. It was expected since the geometry of the pores is completely compatible with the lamellar phase. Of course, depending on the pore size, the width and distance between adjacent lamellae are different. At $W = 5\sigma$, only one lamella is formed with a thickness of the same order of the pore size, *i.e.* much larger than that of the bulk system. The pore is too wide to host one lamella with the width of the bulk phase but too narrow to host two, and thus a thicker lamella is formed trying to find a compromise between packing and low energy. For $W = 7\sigma$, two lamellae with the width of the bulk phase are formed, but this time the separation between them is slightly shorter than that in bulk (see Table 5.2). For $W = 9.0$, the system still assembles two lamellae, but with some islands of particles on the surface oriented towards the centre of the slit. For $W = 11\sigma$, the pore size allows the formation of a third lamella. Both the lamellar width and the distance between layers are reduced with respect to the bulk phase to adjust to the available volume inside the pore.

Effect of temperature on the inter and intra-cluster ordering

Once we have characterised the ordered microphases obtained under confinement, we study their stability with temperature. We perform simulations, starting from the configurations just described, for temperatures ranging from $T = 0.2$ to $T = 0.5$. The results are summarised in Figure 5.11, where we indicate with symbols the various structures formed.

At low densities, as long as the cluster-crystal is not incommensurate with the pore size, the cluster-crystal survives up to higher temperatures in slit pores than in bulk. For instance, the cluster-crystal is able to survive up to $T = 0.30$ when confined in pores of sizes $W = 5\sigma$, 7σ and 11σ, whereas in bulk it melts at $T = 0.2 - 0.25$ depending on the density. This is another example of the change that the phase diagram undergoes in confinement, which has already been reported in complex and simple fluids [52, 59]. On the contrary, for the pore size $W = 9\sigma$, which is incommensurate with the cluster-crystal periodicity, the structure remains only locally ordered even when temperature is decreased to $T = 0.2$.

We can further study the structure of the confined colloidal fluid by calculating the density profiles along the direction perpendicular to the pore walls, $\rho(z)$. In the first row of Figure 5.13, the local density exhibits a layered structure for all pore widths and at all temperatures, starting from rounded peaks at high temperatures that gradually become sharper as the temperature decreases. At low temperature, for $W = 5\sigma$ and 7σ, the density profiles show a number of different maxima: four for $W = 5\sigma$ and six for $W = 7\sigma$, two smaller ones close to the pore walls and the sharper ones in the centre of the slit. For these two pore sizes, the local density is not zero anywhere within the pore, reflecting that a single layer of clusters has been formed. The distance between two adjacent maxima is of the order of the particle diameter, being a bit shorter at the pore central region (about 0.7σ for $W = 5\sigma$ and 0.9σ for $W = 7\sigma$) than that at the pore walls (about σ in both cases). This is related to some internal ordering in the clusters imposed by the confining walls; particles within the clusters tend to be aligned in planes parallel to the walls. For the two widest pores, $W = 9\sigma$ and 11σ, the formation of two different layers of clusters is evident by the presence of a pronounced depression in the central region of the slit. Interestingly, this depression is more pronounced for

$W = 9\sigma$ than for $W = 11\sigma$. It is remarkable that at $T = 0.5$, the two layers are significantly washed out for $W = 11\sigma$ but remain visible for $W = 9\sigma$. Since the shape of the clusters at $W = 9\sigma$ is more elongated, and the ordered microphase is formed with defects, both the interpenetration of the two layers and the particle exchange between them is more impeded than in the stack of two hexagonal layers of spherical clusters formed at $W = 11\sigma$. Additionally, for $W = 9\sigma$, the layers of clusters are placed at a shorter distance to be compared with the optimal arrangement. Thus, the particles from different layers feel a high repulsion that hinders the exchange. As the temperature is lowered, smaller peaks appear within each of these two layers, with an inter-distance again of the order of the particle diameter (about 0.95σ for $W = 9\sigma$ and 0.90σ for $W = 11\sigma$), evidencing the stratification of the particles forming the clusters induced by the pore walls.

The dependence of the cluster size distribution with the pore width and the temperature are shown in Figure 5.14. At $T = 0.3$, the bulk cluster size distribution is bi-modal, showing two peaks of similar probability at $n = 19$ and $n = 23$. Differently, in the confined systems, the cluster size distributions become uni-modal, with the cluster size maximum probability depending on the pore size. For $W = 3\sigma$, the peak is reached at $n = 19$. At this temperature the clusters adopt the structure of two interpenetrated icosahedra, which is one of the two nearly equally probable structures found in bulk (See Section 5.2). For $W = 7\sigma$, the maximum of the cluster size distribution is located at a larger size with respect to the other pores and the bulk, which is consistent with the elongated spherocylindrical clusters that are formed for this pore size. Visual inspection of the configurations of the particles reveals that at low temperature these spherocylinders adopt well-defined geometries consisting of tubes formed by the interpenetration of four icosahedra. For $W = 9\sigma$, the elongated shape of the clusters is also reflected in the cluster size distribution that reaches its maximum at

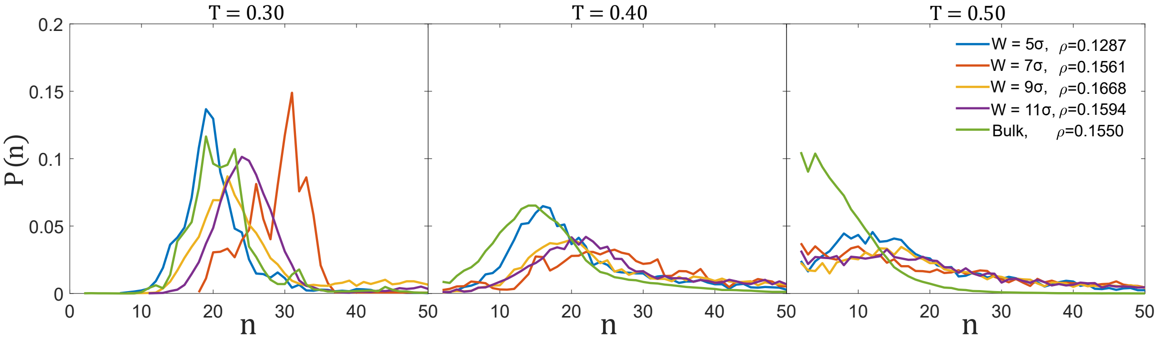

Figure 5.14: .Comparison of the cluster size distributions between bulk and confined systems at different temperatures

$n = 22$, corresponding to aggregates made of three interpenetrated icosahedra. For $W = 11\sigma$, the maximum probability shifts again to a slightly larger size $n = 24$, corresponding to aggregates with three icosahedral cores with the extra two particles attached to the surface. Naturally, as the temperature increases, the cluster size distributions widen until they eventually show rather uniform distributions. These uniform distributions expand to large cluster sizes, indicating percolating states. This occurs to all pore sizes at $T = 0.5$, but not for the bulk system, in which the distribution adopts the maxima values at small sizes, consistent with the formation of a cluster-fluid in which small clusters are more frequent than big ones ($n \leq 10$) (see figure 5.14, right panel).

Following the analysis on the bulk system in Section 5.2, we study the evolution of the internal order of the clusters with temperature by performing a CNA[130] (with a cutoff radius of 1.6σ) using OVITO visualisation tool [97]. The results are shown in Figure 5.15 (top panel). At these low densities, the internal ordering exhibits a similar temperature dependence as in the bulk system. Clusters are internally ordered at low temperature, as evidenced by a fraction of particles close to 10%, which is consistent with the number of particles within icosahedral centres in the cluster geometries just described. As the temperature increases, the fraction of icosahedral particles gradually decreases until it vanishes around $T = 0.4$.

Now, we move to discuss the results at intermediate densities, at which the hexagonal phase is formed at low enough temperatures. Figure 5.11 shows that the hexagonal phase remains stable in roughly the same range of temperatures as in the bulk system. The number of layers of cylinders can again be inferred from the density profiles $\rho(z)$ and, except in the narrowest pore, the stratification of the particles within the clusters at low temperature is intensified as compared to low densities (See Figure 5.13). At $W = 5\sigma$, one single layer of cylindrical aggregates is formed with two rounded peaks of enhanced local density, indicating a mild tendency of the particles in the cylinders to sit preferentially in these two planes. For $W = 7\sigma$ and 9σ, two layers of cylinders (each one composed of three sharp peaks at $T = 0.2$) are formed separated by a region of vanishing or low local density. The height of the peaks depends on the pore width. In the two cases, the central peak is the highest, but at $W = 9\sigma$, the two edge peaks are symmetric, whereas, at $W = 7\sigma$, the peak closer to the pore centre is smaller. The inner peaks become shoulders at $T = 0.3$ for $W = 7\sigma$, but they survive up to $T = 0.4$ for $W = 9\sigma$. The same occurs for the region of very low density between the two layers of cylinders that persists up to $T = 0.3$ for $W = 9\sigma$, but that becomes a region of small density for $W = 7\sigma$. This suggests that the cylinders are more symmetric and less deformed for $W = 9\sigma$, which coincides with our observation that two layers of bulk hexagonal phase fit better in the pore width $W = 9\sigma$. For $W = 11$, the two layers of cylinders are not separated by a region of negligible density even at the lowest considered temperature. The reason behind this is that for $W = 11\sigma$, the distance between layers of cylindrical aggregates is much larger than that in bulk, and the formation of only two layers of cylinders leads to a rather low density within the pores, which is compensated by the growth of small islands of particles on the surfaces of the cylindrical clusters that point to the centre of the slit pore.

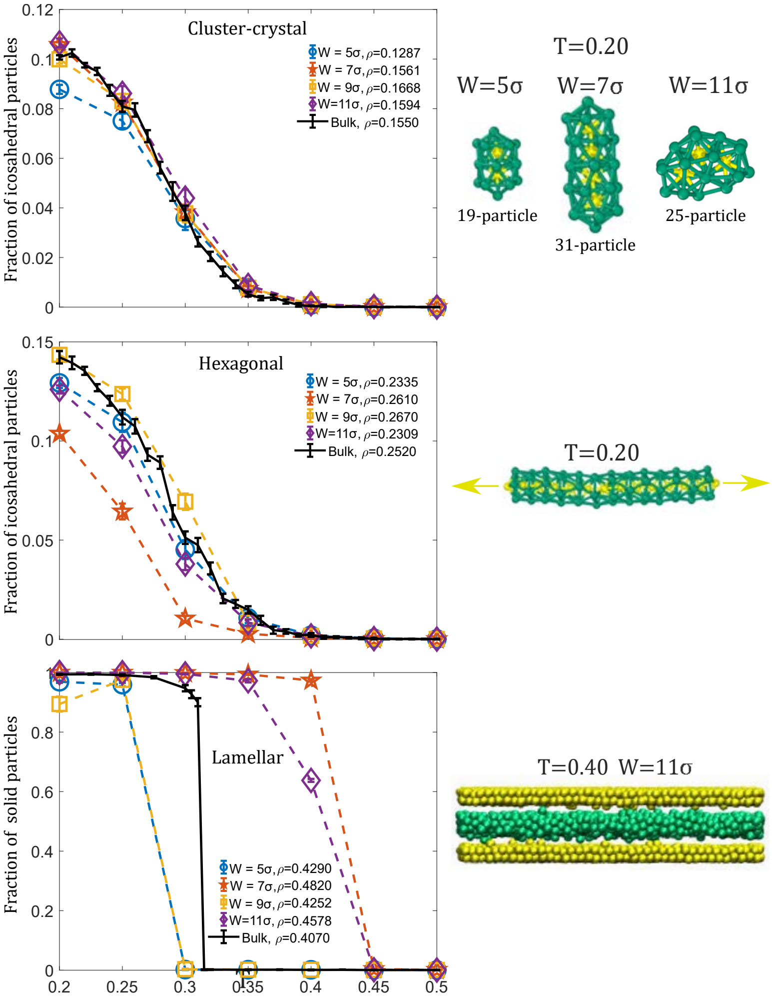

Figure 5.15: The fraction of icosahedral particles as a function of temperature for bulk and confined systems. Top panel: low densities at which the cluster-crystal phase is stable at low temperatures. Central panel: intermediate densities at which the hexagonal phase is stable at low temperatures. Bottom panel: the fraction of solid particles as a function of temperature for bulk and confined systems at high density at which the lamellar phase is stable at low temperatures.

Visual inspection of the configurations reveals that, as in the bulk system, at low temperatures, the cylindrical clusters adopt ordered configurations consisting of tubes made of a succession of interpenetrated icosahedra sharing a five-fold axis. As can be seen in Figure 5.15 central panel, the evolution of the fraction of icosahedral particles with temperature exhibits similar behaviour to the bulk system. Unsurprisingly, the results are almost exactly the same as that of bulk for $W = 9\sigma$, and the larger reduction of order is observed for the most incommensurate pore with $W = 7\sigma$.

Finally, at high densities, the lamellar phase is able to survive up to $T = 0.4$ for all pore widths, *i.e.* above the bulk system in which the transition occurs at $T \approx 0.35$ (See Figure 5.11). This is the expected behaviour as the geometry of the pores is compatible with that of the lamellar phase; thus, it is favoured even at temperatures at which it is not stable in bulk. The density profiles (See Figure 5.13, bottom panels), $\rho(z)$ further reveal that the lamellar phase is particularly stable, especially for the pore sizes $W = 7\sigma$ and $W = 11\sigma$, in which the colloidal fluid self-assembles into two and three lamellae, respectively. These lamellae contain two layers of colloidal particles, as evidenced by the two sharp peaks observed in each lamella up to relatively high temperatures ($T = 0.4$). Curiously, for $W = 11\sigma$ and $T = 0.4$, the two lamellae close to the pore walls are still very structured (solid-like), but the one in the middle exhibits two much more rounded peaks (liquid-like). For the pore with $W = 9\sigma$, only two lamellae are formed, but each lamella is now composed of two equally populated layers of particles (next to the pore walls) and by an incomplete third layer facing the centre of the pore, signalled by a less sharp peak. In this case, the peaks that indicate the ordering of the particles in layers are already rounded at $T = 0.3$, meaning that in this case the internal ordering of the lamellae is not able to survive up to high temperature. For the narrowest pore, $W = 5\sigma$, as found at lower densities, the tendency of the particles to form planes parallel to the walls is significantly reduced in the narrowest pore, which only exhibits mild peaks for $T \leq 0.3$. At $T = 0.20$, the density profile is not symmetric, indicating that the lamella is frozen and the sampling process becomes too slow. The lamella is formed by three layers of colloidal particles, one complete in the middle and two incomplete close to the pore walls. This is observed from the density profile, with the highest peak in the centre of the pore and two lower peaks close to the walls.

The evolution of the internal ordering of the lamellae with temperature was monitored using the Lechner and Dellago [129]order parameter, which allows us to distinguish particles within liquid-like local environments from those in compact solid-like environments. The results are presented in the bottom panel of Figure 5.15. In this case, the local order within lamellae depends strongly on the pore size, differing from the bulk phase for all pore widths. At $T = 0.2$, the fraction of solid particles is very high (close to 100%) for all pores, except for $W = 9\sigma$, in which case the number of solid particles drops to 90%. This can be explained by the formation of a third incomplete layer of colloidal particles in each lamellae facing the centre of the pore. For $W = 7\sigma$, the transition from solid-like to liquid-like lamellae is abrupt as in bulk but occurs at a higher temperature than in the homogeneous system. For $W = 11\sigma$, the decay of the fraction of solid particles is more gradual since at $T = 0.4$ about 63% of the particles remain solid. The reason is that, as mentioned before, the two lamellae at the pore walls melt at higher temperature ($T = 0.4$) than that at the middle ($T = 0.30$). From these results, it is clear that the walls promote the internal freezing of the lamellae, but those lamellae that are not next to the walls freeze at similar temperatures as in bulk. Finally, for $W = 5\sigma$ and $W = 7\sigma$, the lamellae become liquid-like at a lower temperature than in bulk, which is attributed to the incommensurability of the bulk lamellar phase with these pore widths.

5.3.2 Dynamic properties

After the thermodynamic and structural characterisation of the system, we move on to study the dynamic properties at temperatures around which the transition from the fluid to the periodic microphases occurs. Strictly, the comparison between the bulk and the confined systems should be done at the same chemical potential. However, due to the phase diagram changes induced by the confinement, we often found that at the same chemical potential, the ordered microphases were not properly formed for some pore sizes. Thus, we decided to compare the densities at which the ordered microphases exhibit fewer defects since our purpose is to find the conditions (thermodynamic and pore size) that lead to an easier formation of the periodic microphases.

We show the MSD measured in the four pore sizes at densities at which the cluster-crystal, the hexagonal and the lamellar phases are formed in Figure 5.16.

Let us start the discussion with the results of the cluster-crystal phase. We analyse two temperatures: one above the transition from the cluster-fluid to the cluster-crystal ($T = 0.4$) and one below ($T = 0.3$). At $T = 0.4$, the behaviour is qualitatively similar in the four considered pore sizes and also in the bulk system. The MSD at long times adopts a linear behaviour, indicating a diffusive regime. The diffusion coefficient (D), calculated using Einstein's relation, as a function of the pore size, is shown in Figure 5.17. We observe that, at this temperature, the diffusion coefficient strongly depends on the pore width. The maximum diffusion is achieved for the narrowest pore ($W = 5\sigma$), case in which the diffusion coefficient is even higher than that in the bulk system. The minimum

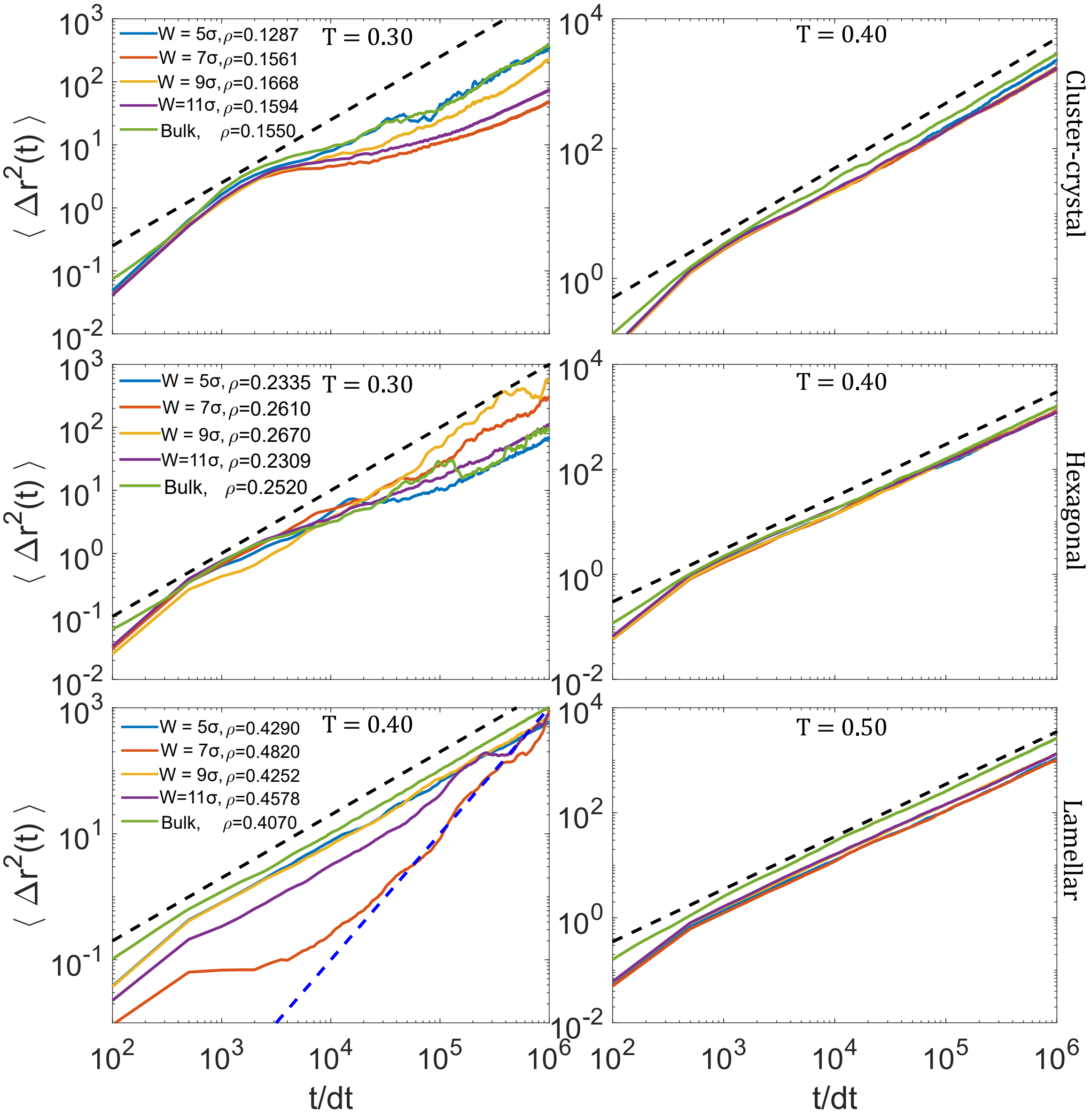

Figure 5.16: Particle mean squared displacement (MSD) of the colloidal fluid confined in slit pores of different width W at different temperatures and densities at which the cluster-crystal (top row), the hexagonal (middle row) and the lamellar (bottom row) phases are stable. For comparison, the MSD for the bulk system at similar thermodynamic conditions is also included.

diffusion coefficient corresponds to the $W = 7$ pore, a value from which it increases with the pore size until it reaches the bulk behaviour. We stress that the narrowest pore is the only one in which the colloidal fluid is still organised in intermediate size clusters at $T = 0.4$, as in the bulk system. This can be seen from the cluster size distributions from Figure 5.14. Differently, in the remaining pore sizes, the maxima of the cluster size distributions are shifted to larger sizes. We speculate that the arrangement of the particles in smaller clusters facilitates the particle diffusion, which can occur by single particle displacements but also by displacement of the clusters as a whole. This enhancement of the diffusion under confinement in quite narrow pores has been already reported in systems with interactions at two different ranges[145, 146]. Our hypothesis is that the repulsive interaction between the colloidal particles and the pore walls pushes the particles away from the walls, but because of the spatial constraints, they only can move in the xy plane, which induces an enhancement of the single particle and cluster displacements and, in consequence, a higher diffusion coefficient with respect to the other pore sizes and the bulk.

At $T = 0.3$, the behaviour of the MSD at long times depends on the pore size. For the narrowest pore, the particle movement is diffusive as in bulk, but for the remaining pores, it becomes subdiffusive. This effect is more pronounced for $W = 7\sigma$. We speculate that the elongated shape of the clusters in this pore size inhibits the displacement of the clusters as a whole. Another possible reason is that at $W = 7\sigma$, the cluster-crystal still exhibits a very ordered distribution of the clusters whereas at $W = 5\sigma$ and $W = 9\sigma$, there are defects that can favour the displacement of clusters as a whole since the clusters are continuously rearranging. This hypothesis is supported by the fact that at $W = 11\sigma$, case in which the cluster-crystal is perfectly ordered, the MSD adopts a very similar behaviour to that observed at $W = 7\sigma$.

Now, we move to the hexagonal phase. The particle movement is diffusive at long times either at temperatures just above ($T = 0.4$) and below ($T = 0.3$) those at which the hexagonal phase is formed. At $T = 0.4$, the MSD are very similar for both confined and bulk systems. The diffusion coefficient adopts similar values for the four pore sizes, being higher in confinement than in the bulk system (See Figure 5.17, central panel). Our hypothesis is that although a percolating fluid is formed in the four pores considered and in bulk, at $T = 0.4$, the fluid is further from the microphase separation under confinement than in bulk (see Figure 5.11). In this situation, it is reasonable that the diffusion coefficient and the MSD are higher in the confined systems.

At $T = 0.3$, the MSD behaviour changes with the pore size. In particular, we observe that it takes higher values at long times for $W = 9\sigma$ and $W = 5\sigma$ than those of the remaining systems. However, it is important to note that cylinders are parallel to one of the edges of the square section of the simulation box in the $W = 7\sigma$ and 9σ pores, whereas, for $W = 5\sigma$ and 11σ, they are tilted (See Figure 5.12).

Thus, in the former cases, each cylinder is an independent cluster, but in the latter cases, all

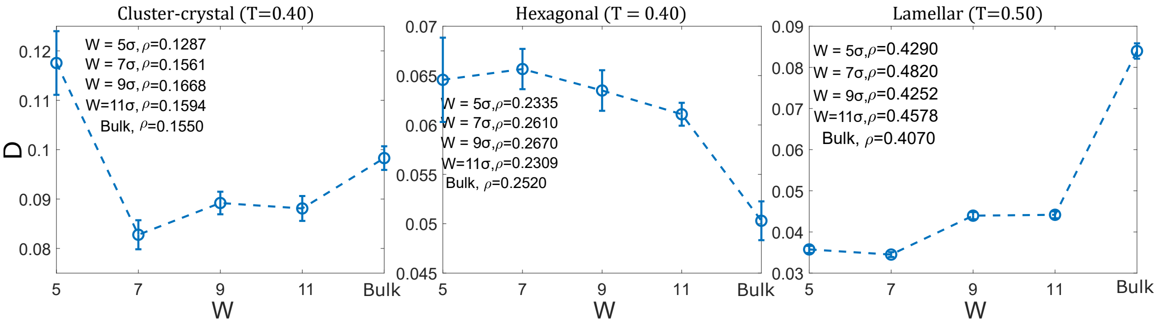

Figure 5.17: Diffusion coefficient for different slit widths at temperatures just above the formation of the ordered microphases.

the cylinders belonging to the same layer are connected to each other due to the periodic boundary conditions. Consequently, the cylindrical clusters can move with respect to their neighbours in the narrowest and the widest considered pores, but not in the $W = 7\sigma$ and 9σ pores.

Finally, we discuss the dynamic behaviour of the lamellar phase. Again, we consider temperatures above ($T = 0.5$) and below ($T = 0.4$) those at which the lamellar phase starts to form.

At $T = 0.5$, the MSD show diffusive behaviour for all systems, but it is clearly larger in the bulk system (see Figure 5.16, bottom-right panel). The diffusion coefficients under confinement are significantly lower than that in bulk for the four considered pore sizes (See Figure 5.17). Our hypothesis is that this might be related to the more efficient packing obtained in the four confined systems compared to that in the bulk system.

At $T = 0.4$, the MSD show two different types of behaviour at long times: for $W = 5\sigma$, 9σ, 11σ and the bulk system, the behaviour is diffusive, whereas for $W = 7\sigma$ is super-diffusive (*i. e.* the MSD is proportional to t^{α}, α being an exponent higher than 1). Our hypothesis is that this enhanced MSD is related to the uniform surfaces (*i e.* surfaces with only small defects) of the lamellae in this pore size. For $W = 7\sigma$, the colloidal fluid organises into two lamellae, each one made of two hexagonally packed layers of particles. As a consequence, the two lamellae can slide with respect to each other, leading to a high MSD. This effect is not observed either at $W = 9\sigma$ or $W = 11\sigma$, because the lamellae surface is no longer uniform due to the formation of an incomplete third layer at $W = 9\sigma$ and to the liquid-like structure of the central lamella at $W = 11\sigma$. We also observed this phenomenon in the bulk lamellar phase when the lamellae are solid-like and are oriented parallel to one of the simulation box axes as discussed in Section 5.2.2.

5.4 Summary and conclusions

This Chapter begins with an extensive analysis of the bulk behaviour of a system of colloidal particles with competing interactions modelled with the LJY potential (Section 5.2). We performed a thermodynamic, structural and dynamic study. We have found that the cluster-crystal, cylindrical and lamellar phases freeze at low temperature. Such phenomenon has already been documented in the lamellar phase in former studies [36, 118], but in this Chapter, we show that similar freezing transitions can also occur in the cluster-crystal and cylindrical phases. However, discontinuities in the energy, the density or the order parameter coincident with the freezing of the microphases were only observed in the lamellar phase. Note that as thermodynamic phase transitions are not possible in one-dimensional systems, and as cylindrical clusters can be considered as systems whose dimension is intermediate between one- and -two, the cylindrical phases formed in SALR systems could be used to investigate the nature of the internal order-disorder transition as the radius of the cylinders increases, which might be achieved by increasing the attraction range. In the dynamical analysis, we did not find any signal of dynamic arrest at temperatures just above those at which the periodic microphases emerge, which could kinetically prevent their formation in experiments. We also found that the three periodic microphases formed readily in our simulations, which indicates that the nucleation of the periodic microphases from the fluid phase can be achieved, at least for the chosen model parameters. We believe that, although the strength of the attractive and repulsive contributions can be modified in experiments with colloids, these phases have not yet been observed in the laboratory due to, probably, the difficulty of finely tuning the appropriate ranges of the effective interactions [9]. On the other hand, the phase diagram has not been sufficiently explored in experimental colloidal systems so far [26]. A good alternative to improve the tunability of the ranges of interaction of colloidal systems is to add on the surface of the particles functionalised hydrophobic molecules as proposed in a recent experimental study [49].

As for the system under confinement (Section 5.3), we have studied the assembly of colloids with competing interactions when confined in narrow slit pores at densities for which the cluster-crystal, the cylindrical, and the lamellar phases are stable in bulk at low enough temperatures. We found that those periodic microphases are also stable under confinement. Our results predict that the stability of the cluster-crystal and the lamellar phases are higher than in bulk system, but that of the cylindrical phase is lower than in bulk (see Figure 5.11). For the cases in which the pore size is not perfectly commensurate with the lattice constant and size of the microphases, the colloidal fluid can often adjust the cluster shape, size and inter-distance to adjust the available volume inside the pore. One exception to this general behaviour is that the cluster-crystal was not formed even at low temperatures in the $W = 9\sigma$ slit, which can be understood because this pore size is incommensurate with the bulk cluster size, d_0 and inter-distance l_0. We conclude that, in general, the presence of walls promote the formation of the lamellar phase, as expected, but also of the cluster-crystal.

We have also observed that the presence of walls induces the stratification of the particles forming the clusters (spherical, cylindrical or lamellar) in planes of particles parallel to the pore walls. This has already been observed in simple and complex fluids [147, 148, 149], and also recently in the adsorption of colloids with competing interactions at an attractive surface [67]. In the case of the lamellar phase, this leads to the freezing of the lamellae at higher temperatures than in bulk system and to an interesting behaviour in which the lamellae adjacent to the pore walls have solid-like structures, whereas those at the central region of the slit show a liquid-like behaviour. This phenomenon was observed in the widest considered pore.

Regarding the dynamic behaviour, we have calculated the MSD (see figure 5.16) and the diffusion coefficient (see figure 5.17) of the confined and bulk systems for selected temperatures. We observe that the MSD behaviour depends on the pore width, especially at temperatures in which the ordered microphases are stable. In particular, the lamellar phase at $T = 0.4$ can exhibit super-diffusive behaviour when confined in a slit of $W = 7\sigma$, due to the sliding of the frozen lamellae. The diffusion coefficient as a function of the pore size reveals that at low densities, the diffusion is enhanced when the colloidal fluid is confined in the narrowest considered pore, a phenomenon that has been already reported in different confined systems composed of molecules interacting with pair potentials with two different ranges of interaction[145]. On the other hand, the cylindrical phase exhibits an enhanced diffusion when the cylindrical aggregates are aligned parallel to either x or y axes of the simulation box. This alignment implies that each cylinder is an independent cluster that can slide with respect to each other in a similar way as in the lamellae with solid-like structure. This phenomenon only occurs at $T = 0.3$ at which the cylindrical clusters still have some internal icosahedral order (see Figure 5.15). In the lamellar phase, the diffusion coefficient at $T = 0.5$ is significantly higher for the bulk than those of the confined systems. The reason behind this is the differences between the densities of the bulk and confined systems, being the latter always larger, and thus the more dense percolating fluid in the confined systems somewhat impede the diffusion. At $T = 0.4$, the sliding of frozen lamellae explains the maximum diffusion coefficient at $W = 7\sigma$.

Also, the bulk system diffuses slightly faster than the confined systems since, at this temperature, the lamellar phase is already molten into a percolating fluid in bulk.

In previous Chapters, we showed that confinement could favour the formation of ordered microphases. In this Chapter, we further demonstrate that confinement helps in the nucleation of periodic microphases since it can even induce the enhancement of the dynamic properties of the microphases for some appropriate conditions.

Chapter 6

Thesis summary

We have studied the effects of confinement on the self-assembly of colloidal systems with competing interactions. We have considered two model systems with different SALR potentials: the SWL (Chapters 2,3 and 4) and the LJY (Chapter 5).

In the SWL system, we used the bulk phase diagram calculated in [25] as a reference to carry out our investigation under different types of confinement. Using MC simulations in the grand canonical ensemble, we have focused on the thermodynamic and structural properties of the system under different types of confinement such as channels with different cross-sections (Sections 2.2 and 2.3), spherical and ellipsoidal shells (3.2), and three-dimensional ordered pores (Section 4.2). The morphology and size of the confining walls strongly affected the structure of the colloidal fluid, not only promoting the formation of novel structures but also favouring the formation of the bulk ordered microphases. The main results of the thesis regarding the SWL model are now summarised:

1. **The confinement into cylindrical pores promotes the formation of helical structures.** At conditions at which the hexagonal cylindrical phase is stable in bulk, the confinement into axially-infinite cylindrical pores favours the formation of helical structures. Depending on the radius of the confining cylinders, the colloidal fluid self-assembles into single, double, and triple helices. Upon increasing the radius of the pore, the system can self-assemble into multi-helical structures close to the pore wall with an additional straight cylindrical aggregate in the centre of the pore. Finally, for the largest pores considered, concentric helices were obtained (see Figure 2.2).

   We found that the system does not prefer a specific handedness when it is assembled into single and double helices (see Figures 2.7 a and b). Different structures can be obtained at the same thermodynamic conditions for a large enough pore radius. Within the numerical accuracy of the calculations, the average energy and density of a double-helix and a triple-helix are the same when the radius of the confining cylinder is $R = 5.5\sigma$(see Figure 2.7 c).

When the colloidal fluid is confined into finite cylindrical pores with planar walls closing its ends, either disk-shaped ($R = 3.5\sigma$) or torus-shaped ($R = 4.5\sigma$) clusters are favoured over the helical structures, which now are stable only for selected values of the pore length, those that are commensurate with the pitch of the helices (see Figure 2.8).

Helical structures under cylindrical confinement have also been obtained in block copolymers [73, 76, 77]. This supports our hypothesis that the universality of the phase behaviour of systems with competing interactions in bulk can also be extended to confinement conditions.

2. **The geometry of the cross-section of the confining pore can either promote novel structures or favour the bulk ordered phases.** At conditions at which the hexagonal cylindrical phase is stable in bulk, the structure of the colloidal fluid is influenced by the geometry of the confining pore. When the geometry of the confining pore is not compatible with the symmetry of the bulk phase, it promotes either novel ordered structures or disordered structures. If the phase periodicity and the pore geometry are slightly incommensurate, new ordered structures emerge. If the incommensurability is too high, then disordered structures are formed. For example, in cases of slight incommensurability, elliptical pores promote the formation of either helical structures or arrangements of straight cylindrical clusters (see Figure 2.9), whereas squared pores promote the formation of straight cylindrical clusters arranged into square lattices (see Figure 2.15). When the incommensurability is too high, both elliptical and squared pores induce disordered structures.

   On the other hand, when the geometry of the confining pore is compatible with the symmetry of the bulk ordered phases, again depending on the incommensurability, the colloidal fluid can self-assemble into either novel ordered structures or into the bulk ordered phases, but the latter case showing an improvement in the nucleation of the ordered phases with respect to the unconfined homogeneous system. Thus, the colloidal fluid is organised in a hexagonal lattice of cylindrical clusters when confined into triangular pores (see Figure 2.11), as long as the size of the pore is large enough for hosting an integer number of cylinders with a radius and a separation distance between cylinders similar to those in bulk. Besides, confinement in hexagonal pores promotes the formation of the hexagonal cylindrical phase when the pore size is commensurate with the periodicity of the phase. Interestingly, in cases with slight incommensurability, helical structures are promoted under hexagonal confinement due to the geometrical similarity between a hexagon and a circle (see Figure 2.13.

The inclusion of the colloidal fluid into wedged-cylindrical pores promotes the formation of straight cylindrical aggregates over helical structures. Moreover, depending on the size and shape of the wedges the bulk hexagonal phase is formed (see Figures 2.19 and 2.21). This suggests that the inclusion of planar walls into the cylindrical pores favours the formation of straight structures even if the pore mostly has curved walls.

We note that the structures observed in the different geometries we considered have also been observed in block copolymers [74, 68, 72], reinforcing our hypothesis of an extended universality in systems with competing interactions in confinement again.

3. **The confinement into spherical shells produces geometrical solutions to the problem of the longest rope on the surface of a sphere.** This type of confinement promotes the formation of cylindrical clusters that adopt configurations compatible with the solutions of the above mentioned geometrical problem, given the radius of the sphere, the thickness of the rope and the separation between turns of the rope. Our results reveal that these structures have very similar energy since small fluctuations in the density can induce the transition from one structure to another (see Figures 3.2 and 3.3). In fact, from our simulations, we observed that the colloidal fluid adopts different configurations (solutions of the geometrical problem) during the same MC run in which the thermodynamic conditions are kept constant (see Figure 3.4).

4. **Confinement into three-dimensional porous materials with a regular structure promotes the formation of new ordered phases composed of spherical and cylindrical clusters.** At conditions at which the cluster-crystal is stable in bulk, the confinement into ordered bicontinuous pores can promote the formation of novel cluster-crystals that are not stable in bulk. Both the topology and the pore size play an important role, and thus these parameters should be properly tuned. In particular, we obtained that the confinement into a P material leads to the formation of SC-cluster and ECC-cluster crystals (see Figure 4.2); confinement into a D material promotes the formation of Pyrochlore-cluster and Diamond-cluster crystals (see Figures 4.4 and 4.5); and confinement into a G material induces the formation of

$P4_132$-cluster and BCC-cluster crystals (see Figure 4.7). In the SWL model, the FCC-cluster crystal is stable in bulk [24]. Our simulations show that, under confinement, the FCC-cluster crystal is obtained more readily than in bulk. Thus, confining the system can be a good strategy to nucleate ordered microphases with the symmetry of the cluster-crystal bulk phase in experimental colloidal systems.

Similarly, at conditions at which the hexagonal cylindrical phase is stable in bulk, the confinement into P and D materials induces the formation of new layered structures in which cylindrical clusters belonging to one layer are rotated with respect to the cylinders in the adjacent layers (see Figures 4.3 and 4.6). Furthermore, the bulk cylindrical phase can be obtained in D and G materials for the appropriate size of the pores (see Figures 4.6 and 4.8).

In the LJY system, using MD simulations, we started by characterising in detail the bulk behaviour of the system (Section 5.2). We found that for this model potential, the colloidal clusters exhibited an internal ordering at low temperatures. Additionally, we investigated the dynamic behaviour of the system, finding that, for the chosen model parameters, the ordered microphases were kinetically accessible from the fluid phase. After investigating the bulk properties, we study the colloidal fluid properties under confinement in slit pores of different widths. We found that the pore size affects the structural and dynamic properties of the microphases. The main results of the thesis regarding the LJY model are now summarised:

1. **The ordered microphases exhibit local ordering at low temperatures**. In the LJY model, besides the transition from the fluid phase to ordered microphases at low temperatures ($T \approx 0.35 - 0.30$), we also observed an internal ordering within the colloidal clusters at lower temperatures ($T \approx 0.27 - 0.25$). Although this internal ordering has been already reported in simulation studies [36, 118, 119], we characterised such internal ordering from the thermodynamic, structural and dynamic points of view. In the cluster-crystal and hexagonal phases, the clusters adopt local icosahedral ordering at low temperatures (see Figures 5.8 and 5.7). In the lamellar phase, the lamellae freeze with the structure of a hexagonally packed stack of two layers of particles (see Figure 5.6).

2. **The bulk microphases are kinetically accessible from the fluid phase.** For the chosen model parameters, the coherent ($F(q,t)$) and incoherent ($F_s(q,t)$) intermediate scattering functions do not show any signal of dynamic arrest at temperatures above the formation of

the ordered microphases (see Figure 5.10). However, the internal ordering of the microphases is clearly signalled by these scattering functions since the correlation does not decay to zero when the microphases are frozen.

3. **The confinement into slit pores can favour, both thermodynamically and kinetically, the formation of the ordered microphases.** The lamellar phase, whose structure is compatible with the slit pores, is more stable under confinement than in bulk. This can be clearly observed from Figure 5.11 since the lamellar phase can survive up to higher temperatures in the confined systems compared to the bulk system. Additionally, the confinement into slit pores modifies the structure of the colloidal fluid at the cluster-cluster and particle-particle scale (see Section 5.3). It can promote particularly interesting phenomena such as the freezing of the lamellae close to the pore walls while the central lamella behaves as a liquid (see Figure 5.15).

   The diffusion of the colloidal fluid can be enhanced by confinement into very narrow slit pores (see Figures 5.16 and 5.17). For instance, the diffusion coefficient of the colloidal fluid at $T = 0.4$ achieves its maximum value when the system is confined into the narrowest pore ($W = 5\sigma$). Our hypothesis is that the repulsive slit walls push away the colloidal particles and increase their movement inside the pore. This behaviour has been already observed in systems with interactions at two different ranges. [145, 146].

Bibliography

[1] G. M. Whitesides and B. Grzybowski, “Self-assembly at all scales,” *Science*, vol. 295, no. 5564, pp. 2418–2421, 2002.

[2] S. Glotzer, M. Solomon, and N. A. Kotov, “Self-assembly: From nanoscale to microscale colloids,” *AIChE Journal*, vol. 50, no. 12, pp. 2978–2985, 2004.

[3] S. Mann, “Self-assembly and transformation of hybrid nano-objects and nanostructures under equilibrium and non-equilibrium conditions,” *Nature Materials*, vol. 8, no. 10, pp. 781–792, 2009.

[4] F. Cardinaux, E. Zaccarelli, A. Stradner, S. Bucciarelli, B. Farago, S. U. Egelhaaf, F. Sciortino, and P. Schurtenberger, “Cluster-driven dynamical arrest in concentrated lysozyme solutions,” *The Journal of Physical Chemistry B*, vol. 115, no. 22, pp. 7227–7237, 2011.

[5] P. D. Godfrin, S. D. Hudson, K. Hong, L. Porcar, P. Falus, N. J. Wagner, and Y. Liu, “Short-time glassy dynamics in viscous protein solutions with competing interactions,” *Physical Review Letters*, vol. 115, no. 22, p. 228302, 2015.

[6] M. W. Matsen and F. S. Bates, “Unifying weak-and strong-segregation block copolymer theories,” *Macromolecules*, vol. 29, no. 4, pp. 1091–1098, 1996.

[7] H. Hu, M. Gopinadhan, and C. O. Osuji, “Directed self-assembly of block copolymers: a tutorial review of strategies for enabling nanotechnology with soft matter,” *Soft Matter*, vol. 10, no. 22, pp. 3867–3889, 2014.

[8] P. Atkins and J. d. Paula, *Physical Chemistry Thermodynamics, Structure, and Change*. WH Freeman and Company New York, 2014.

[9] C. P. Royall, “Hunting mermaids in real space: Known knowns, known unknowns and unknown unknowns,” *Soft Matter*, vol. 14, no. 20, pp. 4020–4028, 2018.

[10] J. Ruiz-Franco and E. Zaccarelli, “On the role of competing interactions in charged colloids with short-range attraction,” *Annual Review of Condensed Matter Physics*, vol. 12, 2021.

[11] S. Asakura and F. Oosawa, “On interaction between two bodies immersed in a solution of macromolecules,” *The Journal of chemical physics*, vol. 22, no. 7, pp. 1255–1256, 1954.

[12] M. Dijkstra, R. van Roij, and R. Evans, “Phase diagram of highly asymmetric binary hard-sphere mixtures,” *Physical Review E*, vol. 59, no. 5, p. 5744, 1999.

[13] Y. Mao, M. Cates, and H. Lekkerkerker, “Depletion force in colloidal systems,” *Physica A: Statistical Mechanics and its Applications*, vol. 222, no. 1-4, pp. 10–24, 1995.

[14] S. Asakura and F. Oosawa, “Interaction between particles suspended in solutions of macromolecules,” *Journal of polymer science*, vol. 33, no. 126, pp. 183–192, 1958.

[15] A. Ciach, “Universal sequence of ordered structures obtained from mesoscopic description of self-assembly,” *Physical Review E*, vol. 78, no. 6, p. 061505, 2008.

[16] A. Ciach and W. Góźdź, “Mesoscopic description of network-forming clusters of weakly charged colloids,” *Condensed Matter Physics*, vol. 13, no. 2, pp. 23603: 1–12, 2010.

[17] A. Ciach, J. Pękalski, and W. Góźdź, “Origin of similarity of phase diagrams in amphiphilic and colloidal systems with competing interactions,” *Soft Matter*, vol. 9, no. 27, pp. 6301–6308, 2013.

[18] Y. Zhuang and P. Charbonneau, “Recent advances in the theory and simulation of model colloidal microphase formers,” *The Journal of Physical Chemistry B*, vol. 120, no. 32, pp. 7775–7782, 2016.

[19] D. Pini and A. Parola, “Pattern formation and self-assembly driven by competing interactions,” *Soft Matter*, vol. 13, no. 48, pp. 9259–9272, 2017.

[20] R. P. Sear and W. M. Gelbart, “Microphase separation versus the vapor-liquid transition in systems of spherical particles,” *The Journal of Chemical Physics*, vol. 110, no. 9, pp. 4582–4588, 1999.

[21] M. B. Sweatman, R. Fartaria, and L. Lue, “Cluster formation in fluids with competing short-range and long-range interactions,” *The Journal of Chemical Physics*, vol. 140, no. 12, p. 124508, 2014.

[22] F. Sciortino, S. Mossa, E. Zaccarelli, and P. Tartaglia, “Equilibrium cluster phases and low-density arrested disordered states: the role of short-range attraction and long-range repulsion,” *Physical Review Letters*, vol. 93, no. 5, p. 055701, 2004.

[23] F. Sciortino, P. Tartaglia, and E. Zaccarelli, “One-dimensional cluster growth and branching gels in colloidal systems with short-range depletion attraction and screened electrostatic repulsion,” *The Journal of Physical Chemistry B*, vol. 109, no. 46, pp. 21942–21953, 2005.

[24] Y. Zhuang, K. Zhang, and P. Charbonneau, “Equilibrium phase behavior of a continuous-space microphase former,” *Physical Review Letters*, vol. 116, no. 9, p. 098301, 2016.

[25] Y. Zhuang and P. Charbonneau, “Equilibrium phase behavior of the square-well linear microphase-forming model,” *The Journal of Physical Chemistry B*, vol. 120, no. 26, pp. 6178–6188, 2016.

[26] Y. Zhuang and P. Charbonneau, “Communication: Microphase equilibrium and assembly dynamics,” *The Journal of Chemical Physics*, vol. 147, no. 9, p. 091102, 2017.

[27] M. Tarzia and A. Coniglio, “Pattern formation and glassy phase in the ϕ 4 theory with a screened electrostatic repulsion,” *Physical Review Letters*, vol. 96, no. 7, p. 075702, 2006.

[28] C. Ortix, J. Lorenzana, and C. Di Castro, “Coulomb-frustrated phase separation phase diagram in systems with short-range negative compressibility,” *Physical Review Letters*, vol. 100, no. 24, p. 246402, 2008.

[29] R. Roth, “Fluid of discs with competing interactions,” *Molecular Physics*, vol. 109, no. 23-24, pp. 2897–2905, 2011.

[30] A. Imperio and L. Reatto, “A bidimensional fluid system with competing interactions: spontaneous and induced pattern formation,” *Journal of Physics: Condensed Matter*, vol. 16, no. 38, p. S3769, 2004.

[31] A. Ciach, “Combined density functional and brazovskii theories for systems with spontaneous inhomogeneities,” *Soft Matter*, vol. 14, no. 26, pp. 5497–5508, 2018.

[32] R. P. Sear, S.-W. Chung, G. Markovich, W. M. Gelbart, and J. R. Heath, "Spontaneous patterning of quantum dots at the air-water interface," *Physical Review E*, vol. 59, no. 6, p. R6255, 1999.

[33] A. Imperio and L. Reatto, "Microphase separation in two-dimensional systems with competing interactions," *The Journal of Chemical Physics*, vol. 124, no. 16, p. 164712, 2006.

[34] T. Nicolai, C. Urban, and P. Schurtenberger, "Light scattering study of turbid heat-set globular protein gels using cross-correlation dynamic light scattering," *Journal of Colloid and Interface Science*, vol. 240, no. 2, pp. 419–424, 2001.

[35] M. Pouzot, T. Nicolai, D. Durand, and L. Benyahia, "Structure factor and elasticity of a heat-set globular protein gel," *Macromolecules*, vol. 37, no. 2, pp. 614–620, 2004.

[36] A. De Candia, E. Del Gado, A. Fierro, N. Sator, M. Tarzia, and A. Coniglio, "Columnar and lamellar phases in attractive colloidal systems," *Physical Review E*, vol. 74, no. 1, p. 010403, 2006.

[37] J. D. Bernal, "The bakerian lecture, 1962. the structure of liquids," *Proceedings of the Royal Society of London. Series A, Mathematical and Physical Sciences*, vol. 280, no. 1382, pp. 299–322, 1964.

[38] A. J. Archer and N. B. Wilding, "Phase behavior of a fluid with competing attractive and repulsive interactions," *Physical Review E*, vol. 76, no. 3, p. 031501, 2007.

[39] E. Zaccarelli, "Colloidal gels: equilibrium and non-equilibrium routes," *Journal of Physics: Condensed Matter*, vol. 19, no. 32, p. 323101, 2007.

[40] H. Sedgwick, S. Egelhaaf, and W. Poon, "Clusters and gels in systems of sticky particles," *Journal of Physics: Condensed Matter*, vol. 16, no. 42, p. S4913, 2004.

[41] A. Stradner, H. Sedgwick, F. Cardinaux, W. C. K. Poon, S. U. Egelhaaf, and P. Schurtenberger, "Equilibrium cluster formation in concentrated protein solutions and colloids," *Nature*, vol. 11, no. 25, pp. 432 – 492, 2004.

[42] A. I. Campbell, V. J. Anderson, J. S. van Duijneveldt, and P. Bartlett, "Dynamical arrest in attractive colloids: The effect of long-range repulsion," *Physical Review Letters*, vol. 94, no. 20, p. 208301, 2005.

[43] R. Sanchez and P. Bartlett, "Equilibrium cluster formation and gelation," *Journal of Physics: Condensed Matter*, vol. 17, no. 45, p. S3551, 2005.

[44] C. L. Klix, C. P. Royall, and H. Tanaka, "Structural and dynamical features of multiple metastable glassy states in a colloidal system with competing interactions," *Physical Review Letters*, vol. 104, no. 16, p. 165702, 2010.

[45] J. Groenewold and W. K. Kegel, "Anomalously large equilibrium clusters of colloids," *The Journal of Physical Chemistry B*, vol. 105, no. 47, pp. 11702–11709, 2001.

[46] T. H. Zhang, J. Klok, R. H. Tromp, J. Groenewold, and W. K. Kegel, "Non-equilibrium cluster states in colloids with competing interactions," *Soft Matter*, vol. 8, no. 3, pp. 667–672, 2012.

[47] T. H. Zhang, B. W. Kuipers, J. Groenewold, W. K. Kegel, *et al.*, "Polydispersity and gelation in concentrated colloids with competing interactions," *Soft Matter*, vol. 11, no. 2, pp. 297–302, 2015.

[48] M. Kohl, R. Capellmann, M. Laurati, S. Egelhaaf, and M. Schmiedeberg, "Directed percolation identified as equilibrium pre-transition towards non-equilibrium arrested gel states," *Nature Communications*, vol. 7, no. 1, pp. 1–8, 2016.

[49] Y. Guo, B. G. van Ravensteijn, and W. K. Kegel, "Self-assembly of isotropic colloids into colloidal strings, bernal spiral-like, and tubular clusters.," *Chemical Communications (Cambridge, England)*, 2020.

[50] R. Evans, "Fluids adsorbed in narrow pores: phase equilibria and structure," *Journal of Physics: Condensed Matter*, vol. 2, no. 46, p. 8989, 1990.

[51] P. Huber, "Soft matter in hard confinement: phase transition thermodynamics, structure, texture, diffusion and flow in nanoporous media," *Journal of Physics: Condensed Matter*, vol. 27, no. 10, p. 103102, 2015.

[52] C. Qiao, S. Zhao, H. Liu, and W. Dong, "Connect the thermodynamics of bulk and confined fluids: Confinement-adsorption scaling," *Langmuir*, vol. 35, no. 10, pp. 3840–3847, 2019.

[53] A. Imperio and L. Reatto, "Microphase morphology in two-dimensional fluids under lateral confinement," *Physical Review E*, vol. 76, no. 4, p. 040402, 2007.

[54] A. J. Archer, "Two-dimensional fluid with competing interactions exhibiting microphase separation: Theory for bulk and interfacial properties," *Physical Review E*, vol. 78, no. 3, p. 031402, 2008.

[55] A. J. Archer, C. Ionescu, D. Pini, and L. Reatto, "Theory for the phase behaviour of a colloidal fluid with competing interactions," *Journal of Physics: Condensed Matter*, vol. 20, no. 41, p. 415106, 2008.

[56] Y. Liu, L. Chew, and M. Yu, "Self-assembly of complex structures in a two-dimensional system with competing interaction forces," *Physical Review E*, vol. 78, no. 6, p. 066405, 2008.

[57] G. J. Zarragoicoechea, A. G. Meyra, and V. A. Kuz, "Pattern formation by interacting particles on the surface of a sphere," *Molecular Physics*, vol. 107, no. 4-6, pp. 549–554, 2009.

[58] A. G. Meyra, G. J. Zarragoicoechea, and V. A. Kuz, "Monte carlo simulation of a binary mixture on the surface of a sphere: lateral phase transition and pattern formation," *Molecular Physics*, vol. 108, no. 10, pp. 1329–1335, 2010.

[59] C. Bores, N. G. Almarza, E. Lomba, and G. Kahl, "Inclusions of a two dimensional fluid with competing interactions in a disordered, porous matrix," *Journal of Physics: Condensed Matter*, vol. 27, no. 19, p. 194127, 2015.

[60] J. Pękalski, N. G. Almarza, and A. Ciach, "Effects of rigid or adaptive confinement on colloidal self-assembly. fixed vs. fluctuating number of confined particles," *The Journal of Chemical Physics*, vol. 142, no. 20, p. 204904, 2015.

[61] J. Pękalski, A. Ciach, and N. G. Almarza, "Bistability in a self-assembling system confined by elastic walls: Exact results in a one-dimensional lattice model," *The Journal of Chemical Physics*, vol. 142, no. 1, p. 014903, 2015.

[62] N. G. Almarza, J. Pękalski, and A. Ciach, "Effects of confinement on pattern formation in two dimensional systems with competing interactions," *Soft Matter*, vol. 12, no. 36, pp. 7551–7563, 2016.

[63] J. Pękalski and A. Ciach, "Orientational ordering of lamellar structures on closed surfaces," *The Journal of Chemical Physics*, vol. 148, no. 17, p. 174902, 2018.

[64] E. Lima, P. Pereira, H. Löwen, and S. Apolinario, "Complex structures generated by competing interactions in harmonically confined colloidal suspensions," *Journal of Physics. Condensed Matter : an Institute of Physics Journal*, vol. 30, p. 325101, August 2018.

[65] L. C. Campos, S. Apolinario, and H. Löwen, "Structural ordering of trapped colloids with competing interactions," *Physical Review E*, vol. 88, no. 4, p. 042313, 2013.

[66] A. Ciach, "Mesoscopic theory for systems with competing interactions near a confining wall," *Physical Review E*, vol. 100, no. 6, p. 062607, 2019.

[67] M. Litniewski and A. Ciach, "Effect of aggregation on adsorption phenomena," *The Journal of Chemical Physics*, vol. 150, no. 23, p. 234702, 2019.

[68] A.-C. Shi and B. Li, "Self-assembly of diblock copolymers under confinement," *Soft Matter*, vol. 9, no. 5, pp. 1398–1413, 2013.

[69] G. S. Doerk and K. G. Yager, "Beyond native block copolymer morphologies," *Molecular Systems Design & Engineering*, vol. 2, no. 5, pp. 518–538, 2017.

[70] A. K. Khandpur, S. Foerster, F. S. Bates, I. W. Hamley, A. J. Ryan, W. Bras, K. Almdal, and K. Mortensen, "Polyisoprene-polystyrene diblock copolymer phase diagram near the order-disorder transition," *Macromolecules*, vol. 28, no. 26, pp. 8796–8806, 1995.

[71] T. L. Chantawansri, A. W. Bosse, A. Hexemer, H. D. Ceniceros, C. J. Garcia-Cervera, E. J. Kramer, and G. H. Fredrickson, "Self-consistent field theory simulations of block copolymer assembly on a sphere," *Physical Review E*, vol. 75, no. 3, p. 031802, 2007.

[72] Y. Xia and W. Li, "Defect-free hexagonal patterns formed by ab diblock copolymers under triangular confinement," *Polymer*, vol. 166, pp. 21–26, 2019.

[73] B. Yu, P. Sun, T. Chen, Q. Jin, D. Ding, B. Li, and A.-C. Shi, "Confinement-induced novel morphologies of block copolymers," *Physical Review Letters*, vol. 96, no. 13, p. 138306, 2006.

[74] B. Yu, P. Sun, T. Chen, Q. Jin, D. Ding, B. Li, and A.-C. Shi, "Self-assembled morphologies of diblock copolymers confined in nanochannels: Effects of confinement geometry," *The Journal of Chemical Physics*, vol. 126, no. 20, p. 204903, 2007.

[75] Y. Wu, G. Cheng, K. Katsov, S. W. Sides, J. Wang, J. Tang, G. H. Fredrickson, M. Moskovits, and G. D. Stucky, "Composite mesostructures by nano-confinement," *Nature Materials*, vol. 3, no. 11, pp. 816–822, 2004.

[76] P. Dobriyal, H. Xiang, M. Kazuyuki, J.-T. Chen, H. Jinnai, and T. P. Russell, "Cylindrically confined diblock copolymers," *Macromolecules*, vol. 42, no. 22, pp. 9082–9088, 2009.

[77] M.-H. Cheng, Y.-C. Hsu, C.-W. Chang, H.-W. Ko, P.-Y. Chung, and J.-T. Chen, "Blending homopolymers for controlling the morphology transitions of block copolymer nanorods confined in cylindrical nanopores," *ACS Applied Materials & Interfaces*, vol. 9, no. 24, pp. 21010–21016, 2017. PMID: 28558189.

[78] D. Frenkel and B. Smit, *Understanding molecular simulation: from algorithms to applications*, vol. 1. Elsevier, 2001.

[79] N. Metropolis, A. W. Rosenbluth, M. N. Rosenbluth, A. H. Teller, and E. Teller, "Equation of state calculations by fast computing machines," *The Journal of Chemical Physics*, vol. 21, no. 6, pp. 1087–1092, 1953.

[80] M. P. Allen and D. J. Tildesley, *Computer simulation of liquids*. Oxford university press, 2017.

[81] D. C. Rapaport, *The art of molecular dynamics simulation*. Cambridge university press, 2004.

[82] S. Nosé, "A unified formulation of the constant temperature molecular dynamics methods," *The Journal of Chemical Physics*, vol. 81, no. 1, pp. 511–519, 1984.

[83] W. G. Hoover, "Canonical dynamics: Equilibrium phase-space distributions," *Physical Review A*, vol. 31, no. 3, p. 1695, 1985.

[84] S. Plimpton, "Fast parallel algorithms for short-range molecular dynamics," *Journal of Computational Physics*, vol. 117, no. 1, pp. 1–19, 1995.

[85] H. Serna, E. G. Noya, and W. Góźdź, "Assembly of helical structures in systems with competing interactions under cylindrical confinement," *Langmuir*, vol. 35, no. 3, pp. 702–708, 2019.

[86] H. Serna, E. G. Noya, and W. T. Góźdź, "The influence of confinement on the structure of colloidal systems with competing interactions," *Soft Matter*, vol. 16, no. 3, pp. 718–727, 2020.

[87] H. Míguez, S. M. Yang, and G. A. Ozin, "Optical properties of colloidal photonic crystals confined in rectangular microchannels," *Langmuir*, vol. 19, no. 8, pp. 3479–3485, 2003.

[88] O. Lecarme, T. Pinedo Rivera, L. Arbez, T. Honegger, K. Berton, and D. Peyrade, "Colloidal optical waveguides with integrated local light sources built by capillary force assembly," *Journal of Vacuum Science & Technology B*, vol. 28, no. 6, pp. C6O11–C6O15, 2010.

[89] L. Fu, C. Bian, C. W. Shields, D. F. Cruz, G. P. López, and P. Charbonneau, "Assembly of hard spheres in a cylinder: a computational and experimental study," *Soft Matter*, vol. 13, no. 18, pp. 3296–3306, 2017.

[90] E. C. Oğuz, R. Messina, and H. Löwen, "Helicity in cylindrically confined yukawa systems," *EPL (Europhysics Letters)*, vol. 94, p. 28005, apr 2011.

[91] S.-C. Kim, S.-H. Suh, and B.-S. Seong, "Microphase separations of the fluids with spherically symmetric competing interactions," *The Journal of Chemical Physics*, vol. 137, no. 11, p. 114703, 2012.

[92] E.-Y. Kim, S.-C. Kim, and S.-H. Suh, "Structure and phase behavior of two-yukawa fluids with competing interactions in planar slit pores," *Physical Review E*, vol. 85, no. 5, p. 051203, 2012.

[93] J. Pękalski, E. Bildanau, and A. Ciach, "Self-assembly of spiral patterns in confined systems with competing interactions," *Soft Matter*, vol. 15, no. 38, pp. 7715–7721, 2019.

[94] H. K. Choi, J.-B. Chang, A. F. Hannon, J. K. Yang, K. K. Berggren, A. Alexander-Katz, and C. A. Ross, "Nanoscale spirals by directed self-assembly," *Nano Futures*, vol. 1, no. 1, p. 015001, 2017.

[95] H. Gerlach and H. von der Mosel, "On sphere-filling ropes," *The American Mathematical Monthly*, vol. 118, no. 10, pp. 863–876, 2011.

[96] C. Varea, J. Aragon, and R. Barrio, "Turing patterns on a sphere," *Physical Review E*, vol. 60, no. 4, p. 4588, 1999.

[97] A. Stukowski, "Visualization and analysis of atomistic simulation data with ovito–the open visualization tool," *Modelling and Simulation in Materials Science and Engineering*, vol. 18, no. 1, p. 015012, 2009.

[98] Y. Yin, Y. Lu, B. Gates, and Y. Xia, "Template-assisted self-assembly: a practical route to complex aggregates of monodispersed colloids with well-defined sizes, shapes, and structures," *Journal of the American Chemical Society*, vol. 123, no. 36, pp. 8718–8729, 2001.

[99] S. Pinge, G. Lin, D. Baskaran, M. Padmanaban, and Y. L. Joo, "Designing an ordered template of cylindrical arrays based on a simple flat plate confinement of block copolymers: A coarse-grained molecular dynamics study," *Soft Matter*, vol. 14, no. 4, pp. 597–613, 2018.

[100] C. Wang, Y. Zhao, L. Zhou, Y. Liu, W. Zhang, Z. Zhao, W. N. Hozzein, H. M. Alharbi, W. Li, and D. Zhao, "Mesoporous carbon matrix confinement synthesis of ultrasmall wo 3 nanocrystals for lithium ion batteries," *Journal of Materials Chemistry A*, vol. 6, no. 43, pp. 21550–21557, 2018.

[101] J. Zhao, Y. Yin, Y. Li, W. Chen, and B. Liu, "Synthesis and characterization of mesoporous zeolite y by using block copolymers as templates," *Chemical Engineering Journal*, vol. 284, pp. 405–411, 2016.

[102] H. Serna, E. G. Noya, and W. T. Góźdź, "Confinement of colloids with competing interactions in ordered porous materials," *The Journal of Physical Chemistry B*, vol. 124, no. 45, pp. 10567–10577, 2020. PMID: 33140966.

[103] Z. Lin, S. Liu, W. Mao, H. Tian, N. Wang, N. Zhang, F. Tian, L. Han, X. Feng, and Y. Mai, "Tunable self-assembly of diblock copolymers into colloidal particles with triply periodic minimal surfaces," *Angewandte Chemie*, vol. 129, no. 25, pp. 7241–7246, 2017.

[104] E. L. Thomas, D. M. Anderson, C. S. Henkee, and D. Hoffman, "Periodic area-minimizing surfaces in block copolymers," *Nature*, vol. 334, no. 6183, pp. 598–601, 1988.

[105] W. T. Góźdź and R. Hołyst, "Triply periodic surfaces and multiply continuous structures from the landau model of microemulsions," *Physical Review E*, vol. 54, no. 5, p. 5012, 1996.

[106] A. Schoen, "Infinite periodic minimal surfaces without self-intersections (nasa electronics research center, cambridge, ma)," tech. rep., Technical Report NASA TN D-5541, C-98, 1970.

[107] M. Deserno, "How to calculate a three-dimensional g(r) under periodic boundary conditions." Available from: https://www.cmu.edu/biolphys/deserno/pdf/gr_periodic.pdf, 2004.

[108] N. Dawass, P. Krüger, S. K. Schnell, D. Bedeaux, S. Kjelstrup, J. M. Simon, and T. Vlugt, “Finite-size effects of kirkwood–buff integrals from molecular simulations,” *Molecular Simulation*, vol. 44, no. 7, pp. 599–612, 2018.

[109] M. Spellings and S. C. Glotzer, “Machine learning for crystal identification and discovery,” *AIChE Journal*, vol. 64, no. 6, pp. 2198–2206, 2018.

[110] D. Z. Rocklin and X. Mao, “Self-assembly of three-dimensional open structures using patchy colloidal particles,” *Soft Matter*, vol. 10, no. 38, pp. 7569–7576, 2014.

[111] W. F. Reinhart and A. Z. Panagiotopoulos, “Equilibrium crystal phases of triblock janus colloids,” *The Journal of Chemical Physics*, vol. 145, no. 9, p. 094505, 2016.

[112] E. Marcotte, F. H. Stillinger, and S. Torquato, “Communication: Designed diamond ground state via optimized isotropic monotonic pair potentials,” *The Journal of Chemical Physics*, vol. 138, no. 6, p. 061101, 2013.

[113] A. Jain, J. R. Errington, and T. M. Truskett, “Dimensionality and design of isotropic interactions that stabilize honeycomb, square, simple cubic, and diamond lattices,” *Physical Review X*, vol. 4, no. 3, p. 031049, 2014.

[114] Y. Wang, I. C. Jenkins, J. T. McGinley, T. Sinno, and J. C. Crocker, “Colloidal crystals with diamond symmetry at optical lengthscales,” *Nature Communications*, vol. 8, no. 1, pp. 1–8, 2017.

[115] A. T. KG, K. Gotrik, A. Hannon, A. Alexander-Katz, C. Ross, and K. Berggren, “Templating three-dimensional self-assembled structures in bilayer block copolymer films,” *Science*, vol. 336, no. 6086, pp. 1294–1298, 2012.

[116] H. T. Stokes and D. M. Hatch, “Program for identifying the space group symmetry of a crystal,” *J. Appl. Cryst.*, vol. 38, p. 237, 2005.

[117] H. T. Stokes, D. M. Hatch, and B. J. Campbell, “Findsym, isotropy software suite.” iso.byu.edu.

[118] A. Coniglio, A. de Candia, and A. Fierro, “Modulated phases and structural arrest in colloidal systems with competing interactions,” *Molecular Physics*, vol. 109, no. 23-24, pp. 2981–2987, 2011.

[119] J. Pękalski, W. Rządkowski, and A. Z. Panagiotopoulos, “Shear-induced ordering in systems with competing interactions: A machine learning study,” *The Journal of Chemical Physics*, vol. 152, no. 20, p. 204905, 2020.

[120] D. Stopper and R. Roth, “Nonequilibrium phase transitions of sheared colloidal microphases: Results from dynamical density functional theory,” *Physical Review E*, vol. 97, no. 6, p. 062602, 2018.

[121] J. Ruiz-Franco, D. Jaramillo-Cano, M. Camargo, C. N. Likos, and E. Zaccarelli, “Multi-particle collision dynamics for a coarse-grained model of soft colloids,” *The Journal of Chemical Physics*, vol. 151, no. 7, p. 074902, 2019.

[122] J. C. F. Toledano, F. Sciortino, and E. Zaccarelli, “Colloidal systems with competing interactions: from an arrested repulsive cluster phase to a gel,” *Soft Matter*, vol. 5, no. 12, pp. 2390–2398, 2009.

[123] E. Mani, W. Lechner, W. K. Kegel, and P. G. Bolhuis, “Equilibrium and non-equilibrium cluster phases in colloids with competing interactions,” *Soft Matter*, vol. 10, no. 25, pp. 4479–4486, 2014.

[124] A. P. Santos, J. Pękalski, and A. Z. Panagiotopoulos, “Thermodynamic signatures and cluster properties of self-assembly in systems with competing interactions,” *Soft Matter*, vol. 13, no. 44, pp. 8055–8063, 2017.

[125] M. G. Noro and D. Frenkel, “Extended corresponding-states behavior for particles with variable range attractions,” *The Journal of Chemical Physics*, vol. 113, no. 8, pp. 2941–2944, 2000.

[126] P. D. Godfrin, N. E. Valadez-Pérez, R. Castaneda-Priego, N. J. Wagner, and Y. Liu, “Generalized phase behavior of cluster formation in colloidal dispersions with competing interactions,” *Soft Matter*, vol. 10, no. 28, pp. 5061–5071, 2014.

[127] H. Serna, A. D. Pozuelo, E. G. Noya, and W. T. Góźdź, “Formation and internal ordering of periodic microphases in colloidal models with competing interactions,” *Soft Matter*, vol. 17, no. 19, pp. 4957–4968, 2021.

[128] J. Škvor and I. Nezbeda, “Percolation threshold parameters of fluids,” *Physical Review E*, vol. 79, no. 4, p. 041141, 2009.

[129] W. Lechner and C. Dellago, “Accurate determination of crystal structures based on averaged local bond order parameters,” *The Journal of Chemical Physics*, vol. 129, no. 11, p. 114707, 2008.

[130] D. Faken and H. Jónsson, “Systematic analysis of local atomic structure combined with 3d computer graphics,” *Computational Materials Science*, vol. 2, no. 2, pp. 279–286, 1994.

[131] J. P. Doye and D. J. Wales, “Structural consequences of the range of the interatomic potential a menagerie of clusters,” *Journal of the Chemical Society, Faraday Transactions*, vol. 93, no. 24, pp. 4233–4243, 1997.

[132] D. J. Wales and J. P. Doye, “Global optimization by basin-hopping and the lowest energy structures of lennard-jones clusters containing up to 110 atoms,” *The Journal of Physical Chemistry A*, vol. 101, no. 28, pp. 5111–5116, 1997.

[133] D. F. Schwanzer, D. Coslovich, and G. Kahl, “Two-dimensional systems with competing interactions: dynamic properties of single particles and of clusters,” *Journal of Physics: Condensed Matter*, vol. 28, no. 41, p. 414015, 2016.

[134] P. Pieranski, “Two-dimensional interfacial colloidal crystals,” *Physical Review Letters*, vol. 45, no. 7, p. 569, 1980.

[135] P. Pieranski, L. Strzelecki, and B. Pansu, “Thin colloidal crystals,” *Physical Review Letters*, vol. 50, no. 12, p. 900, 1983.

[136] J. Zhang, Y. Li, X. Zhang, and B. Yang, “Colloidal self-assembly meets nanofabrication: From two-dimensional colloidal crystals to nanostructure arrays,” *Advanced Materials*, vol. 22, no. 38, pp. 4249–4269, 2010.

[137] O. D. Velev and A. M. Lenhoff, “Colloidal crystals as templates for porous materials,” *Current Opinion in Colloid & Interface Science*, vol. 5, no. 1-2, pp. 56–63, 2000.

[138] U. B. Sleytr, C. Huber, N. Ilk, D. Pum, B. Schuster, and E. M. Egelseer, “S-layers as a tool kit for nanobiotechnological applications,” *FEMS microbiology letters*, vol. 267, no. 2, pp. 131–144, 2007.

[139] Z. Tang, Z. Zhang, Y. Wang, S. C. Glotzer, and N. A. Kotov, “Self-assembly of cdte nanocrystals into free-floating sheets,” *Science*, vol. 314, no. 5797, pp. 274–278, 2006.

[140] Z. Shi, Y. Wei, C. Zhu, J. Sun, and Z. Li, "Crystallization-driven two-dimensional nanosheet from hierarchical self-assembly of polypeptoid-based diblock copolymers," *Macromolecules*, vol. 51, no. 16, pp. 6344–6351, 2018.

[141] C. O'Hern and T. Lubensky, "Sliding columnar phase of dna-lipid complexes," *Physical Review Letters*, vol. 80, no. 19, p. 4345, 1998.

[142] E. G. Noya, I. Kolovos, G. Doppelbauer, G. Kahl, and E. Bianchi, "Phase diagram of inverse patchy colloids assembling into an equilibrium laminar phase," *Soft Matter*, vol. 10, no. 42, pp. 8464–8474, 2014.

[143] S. Ferrari, E. Bianchi, and G. Kahl, "Spontaneous assembly of a hybrid crystal-liquid phase in inverse patchy colloid systems," *Nanoscale*, vol. 9, no. 5, pp. 1956–1963, 2017.

[144] Z. Varga and J. Swan, "Hydrodynamic interactions enhance gelation in dispersions of colloids with short-ranged attraction and long-ranged repulsion," *Soft Matter*, vol. 12, no. 36, pp. 7670–7681, 2016.

[145] J. R. Bordin, A. B. de Oliveira, A. Diehl, and M. C. Barbosa, "Diffusion enhancement in core-softened fluid confined in nanotubes," *The Journal of Chemical Physics*, vol. 137, no. 8, p. 084504, 2012.

[146] L. B. Krott and M. C. Barbosa, "Model of waterlike fluid under confinement for hydrophobic and hydrophilic particle-plate interaction potentials," *Physical Review E*, vol. 89, no. 1, p. 012110, 2014.

[147] H. Mosaddeghi, S. Alavi, M. H. Kowsari, B. Najafi, S. Az'hari, and Y. Afshar, "Molecular dynamics simulations of nano-confined methanol and methanol-water mixtures between infinite graphite plates: Structure and dynamics," *The Journal of Chemical Physics*, vol. 150, no. 14, p. 144510, 2019.

[148] P. Pršlja, E. Lomba, P. Gómez-Álvarez, T. Urbič, and E. G. Noya, "Adsorption of water, methanol, and their mixtures in slit graphite pores," *The Journal of Chemical Physics*, vol. 150, no. 2, p. 024705, 2019.

[149] S. Ruiz-Barragan, D. Munoz-Santiburcio, and D. Marx, "Nanoconfined water within graphene slit pores adopts distinct confinement-dependent regimes," *The Journal of Physical Chemistry Letters*, vol. 10, no. 3, pp. 329–334, 2019.

Institute of Physical Chemistry
Polish Academy of Sciences

Kasprzaka 44/52
01-224 Warsaw, Poland

www.ichf.edu.pl